UNIVERSIDADE DA BEIRA INTERIOR
Engenharia

Airfoil Improvement on Horizontal Axis Wind Turbine Suitable for Local Construction in Underdeveloped Countries

(Versão corrigida após defesa)

João Carlos Tavares Miguel

Dissertação para obtenção do Grau de Mestre em
Engenharia Aeronáutica
(Ciclo de Estudos Integrado)

Orientador: Prof. Doutor Miguel Ângelo Rodrigues Silvestre
Co-orientador: Prof. Doutor João Manuel Milheiro Caldas Paiva Monteiro

Covilhã, Julho de 2019

“First of all, the Big Bang wasn’t very big. Second of all, there was no bang. Third, Big Bang Theory doesn’t tell you what banged, when it banged, how it banged. It just said it did bang. So, the Big Bang Theory in some sense is a total misnomer.”

Michio Kaku

Acknowledgments

To my parents as they were the ones that allowed for the accomplishment of this dissertation, for my presence in this university and for my personal growth. To my sister that has always supported me, asking me about my academic performance, ready to help me anytime needed.

To my supervisor, Professor Miguel Silvestre for allowing my role in this study, for the readiness and patient given, and mostly for the shared knowledge and hints. To my supervisor, Professor João Monteiro, for the explanations about the Qblade simulations when the results weren't matching.

To the long date friends, to the academic friends met in this journey, to the Erasmus friends and to the bohemian friends for all the wonderful debates about any random topic.

Abstract

This dissertation purpose is to study the impact that a geometry modification of a wind turbine rotor imposes on its performance. The studied wooden rotor, with a diameter of 1.2 m, belongs to a family of small wind turbines that are built by unskilled persons using hand tools with the guidelines of Hugh Piggott. Due to its inaccuracy, the production process delivers a geometry with sharp leading edges. For the performance of an airfoil, the leading edge is one of the most important characteristics to take in mind, and so, the goal of this dissertation was to smooth the airfoils leading edge towards the lower surface in order to widen the $C_p - \lambda$ curve of the rotor. To do so, numerical methods were employed to assess such modification on the performance, in a way that the technique could be later applied on the rotor using nothing but hand tools. In a previous investigation, the same rotor here approached in this dissertation, was numerically and experimentally studied for the following windspeeds: 3.0; 3.7; 4.4; 5.5; 7.2 e 7.7 m/s. In the same study, a digital scan was performed on the rotor, one for each blade, resulting in 6 different cross sections each with its chord and incidence angle. The three blades present geometric differences. Having these airfoils characteristics, the QBlade software was used for the design and analysis of the new modified airfoils based on the original Piggott airfoils. The software also allows for rotor design and uses the Blade Element Momentum Theory for the analysis of horizontal axis wind turbines. The performance of both rotors was approximated by averaging the performance of three ideal rotors, each consisting of three identical blades 1,2 and 3. The new airfoils regarding blade 1 and 3, presented better aerodynamic efficiency performance compared to the Piggott airfoils, whereas blade 2 new airfoils did not exhibited any significant improved performance compared to the Piggott airfoils.The dimensionless simulations results from QBlade, portrayed that the averaged rotor with the modified airfoils present better power coefficient (C_p) for high values of λ (ratio between the tangential velocity of the blade tip and the free stream windspeed) when compared to the averaged rotor with the Piggott airfoils. For a constant rotational speed of 500 RPM, the new rotor remarkably withdraws more energy from the flow for low windspeeds. In a hypothetical approach of a optimized turbine production made up by the best modified airfoils, the optimized rotor simulations showed a significant better performance for high values of λ,as well as higher maximum C_p than the ones from the averaged rotor with the modified airfoils.

Keywords

Leading ege; Airfoil; Hugh Piggott; BEM; C_p; λ; C_l/C_d; *QBlade*

Resumo

O objectivo da presente investigação é estudar a influência que uma modificação na geometria do rotor de uma turbina eólica inflige na sua eficiência. O rotor estudado, de madeira e com um diâmetro de 1,20 m, pertence a um grupo de pequenas turbinas eólicas que são construídas apenas com recurso a ferramentas manuais seguindo as indicações do Hugh Piggott. Este processo de construcção, devido à sua imprecisão, resulta numa geometria que dá origem a um bordo de ataque aguçado. Sendo que o bordo de ataque é um aspecto importante para o desempenho do mesmo, o objectivo desta dissertação passou por suavizar o bordo de ataque do perfil alar a "fugir" para o intradorso, de maneira a ampliar a curva $C_p - \lambda$ do rotor. Para tal, recorreu-se a métodos numéricos para avaliar o desempenho de tal modificação, numa perspectiva que esta técnica possa ser aplicada no rotor usando ferramentas manuais, como por exemplo uma lixa. Num estudo prévio, o mesmo rotor que é estudado nesta dissertação foi alvo de um estudo numérico e experimental para as seguintes velocidades de vento: 3.0; 3.7; 4.4; 5.5; 7.2 e 7.7 m/s. No mesmo estudo o rotor foi alvo de uma digitalização na qual, cada pá do rotor foi examinada em 6 secções diferentes e que resultou em 6 perfis alares diferentes com a respectiva corda e o ângulo de incidência, sendo de realçar que as três pás apresentam diferenças geométricas entre si. Tendo estas características, usou-se o software QBlade para o desenho e análise dos novos perfis alares modificados a partir dos originais perfis alares do Piggott. O software permite o desenho de rotores e para a simulação do desempenho de turbinas eólicas de eixo horizontal, o software emprega a Blade Element Momentum Theory. O desempenho real do rotor original e do novo rotor foi estimado a partir da média de três rotores ideais, cada um constituído por três pás idênticas 1, 2 e 3. Os novos perfis alares das pás 1 e 3 revelaram melhor desempenho da sua eficiência aerodinâmica (C_l/C_d) quando comparados aos perfis oriundos da construção manual do Hugh Piggott, enquanto que os novos perfis da pá 2 não ilustraram qualquer melhoria significativa quando comparados aos perfis originais. Os resultados das simulações adimensionais do QBlade, mostraram que o rotor médio com os novos perfis apresenta melhor coeficiente de potência (C_p) para altos valores de λ (razão entre a velocidade tangencial da ponta da pá e a velocidade do vento) quando comparado ao rotor médio com os perfis do Piggott. Quando submetidos a uma velocidade rotacional constante de 500 RPM, o novo rotor retira notavelmente mais energia do escoamento a baixas velocidades de vento. Numa abordagem hipotética da construcção de uma turbina optimizada composta pelos melhores perfis modificados, as simulações do rotor optimizado ilustraram um significativo melhor desempenho a altos valores de λ como C_p máximos mais elevados do que os do rotor médio com os perfis modificados.

Palavras-chave

Bordo de ataque; Perfil alar; Hugh Piggot; BEM; C_p; λ; C_l/C_d; *QBlade*

Content

List of Figures

List of Figures

List of Figures

List of Tables

Nomenclature

A	Scale factor	$[m/s]$
A_d	Rotor area at the disk cross-section	$[m^2]$
a	Axial induction factor	$[-]$
a'	Rotational induction factor	$[-]$
B	Number of blades	$[-]$
$C_{D,max}$	Maximum drag coefficient	$[-]$
$C_{p,max}$	Maximum power coefficient	$[-]$
C_p	Power coefficient	$[-]$
C_N	Normal force coefficient	$[-]$
C_T	Tangential force coefficient	$[-]$
c	Blade chord length	$[m]$
D	Drag force	$[N/m]$
da	Incremental axial induction factor	$[-]$
dC_T	Incremental thrust coefficient	$[-]$
dP	Incremental extracted power	$[W]$
dC_p	Incremental power coefficient	$[-]$
dQ	Incremental torque	$[Nm]$
dT	Incremental thrust	$[N]$
dr	Radial thickness at the rotor cross-section	$[m]$
E_k	Kinetic energy	$[J]$
$\dot{E}_k$	Kinetic energy flow rate	$[m^3/s]$
F	Prandlt correction factor	$[-]$
F_{hub}	Blade root Prandtl correction factor	$[-]$
F_n	Normal force	$[N]$
F_t	Tangential force	$[N]$
F_{tip}	Prandtl correction factor for the blade tip	$[-]$
L	Lift force	$[N/m]$

m_{air}	Air mass	$[kg]$
$\dot{m}_{air}$	Air mass flow rate through the disk	$[kg/s]$
P_{avai}	Available power in the wind	$[W]$
p_1	Pressure at cross-section 1	$[Pa]$
p_2	Pressure at cross-section 2	$[Pa]$
p_3	Pressure at cross-section 3	$[Pa]$
p_4	Pressure at cross-section 4	$[Pa]$
p_∞	Pressure	$[Pa]$
$p(U)$	Weibull probability density function	$[-]$
Q	Rotor torque	$[Nm]$
R	Maximum rotor radius	$[m]$
Re	Reynolds Number	$[-]$
r	Radial coordinate at the rotor cross-section	$[m]$
r_{hub}	Hub radius	$[m]$
T	Thrust	$[N]$
TSR	Tip speed ratio	$[-]$
U	Windspeed	$[m/s]$
U_1	Windspeed velocity at cross-section 1	$[m/s]$
U_2	Wind velocity at cross-section 2	$[m/s]$
U_3	Wind velocity at cross-section 3	$[m/s]$
U_4	Wind velocity at cross-section 4	$[m/s]$
U_d	Wind velocity at disk cross-section	$[m/s]$
U_{rel}	Relative wind velocity	$[m/s]$

Nomenclature

Greek Alphabet Letters

Δp	Pressure difference between the rotor	$[Pa]$
$\Delta pa'$	Pressure difference between the rotor with only the effect of the wake rotation	$[Pa]$
Ω	Rotor velocity	$[rad/s]$
α	Angle of attack	[°]
θ	Pitch angle	[°]
k	Shape Factor	$[-]$
λ	Tip speed ratio	$[-]$
λ_r	Local tip speed ratio	$[-]$
μ	Dynamic viscosity	$[Ns/m^2]$
v	Kinematic viscosity	$[m^2/s]$
ρ	Volumetric mass density	$[kg/m^3]$
σ	Solidity Ratio	$[-]$
ϕ	Relative wind angle	[°]
ω	Angular velocity	$[rad/s]$

List of Acronyms

APREN	Asssociação Portuguesa de Energias Renováveis
BEM	Blade Element Momentum
BET	Blade Element Theory
GHG	Greenhouse Gas
HAWT	Horizontal Axis Wind Turbine
ICI	International cooperative initiatives
NSA	Non-state or subnational actor
RCP	Representative Concentration Pathways
RE	Renewable Energy
VAWT	Vertical Axis Wind Turbine
WECS	Wind Energy Conversion System
WTG	Wind Turbine Generator

Chapter 1

Introduction

Motivation

The natural greenhouse effect is a balanced transfer and transformation energy system on Earth's atmosphere, terrestrial surface and oceans. This balance means the received energy is equal to the lost energy, making Earth's climate stay largely stable. Nevertheless, there are factors that cause changes in the climate system. During the last millennium, changes in the Sun energy production, volcanic eruptions and the concentration increase of the greenhouse gases were the main reasons to cause such changes. Water vapor, carbon dioxide, methane and nitrous oxide are greenhouse gases and they are fundamental for our and other living things existence, by trapping some of the sun radiation on the atmosphere, thus making Earth liveable. The most important greenhouse gas (GHG) is water vapor followed by carbon dioxide. Scientists have been observing this disruption in the heat balance since the beginning of the twentieth century, known as global warming. The principal cause of global warming is the increase of greenhouse gases in the atmosphere [1]. They occur naturally but their increase since the beginning of the Industrial Revolution due to anthropogenic emissions (burning of fossil fuel as a source of energy, intensive agriculture and deforestation) have reached levels not seen in three million years ago. Atmospheric carbon dioxide has slowly changed from 260 ppm to 280 ppm during the last 7000 years prior to 1750, while it has increased 40% to 390.5 ppm in 2011. During the same period (1750-2011) atmospheric methane and nitrous oxide have increased 150 % and 20 % correspondingly [2]. As they absorb and emit the sun radiation, their concentration increase means more heat is trapped in the atmosphere, leading to an increase of Earth's average temperature and, to other effects on Earth's climate system. These effects are known to be anthropogenic climate changes.

Climate change has a direct impact on human, geophysical, biological and socioeconomic systems. The vulnerability to climate change is how it will damage or harm those systems, and it depends across regions and populations. The resilience to climate change impacts, is the ability of a system to absorb such changes. A developing country is less resilient to the impacts of climate change than a developed one. With these impacts it is fundamental to adapt our behaviour to these changes and mitigate the resulting effects from climate change in the different systems. Climate change affects various human sectors such as agriculture, food, health, water, energy, fisheries, education, nature and ecosystem conservation, among others, in the form of higher temperatures, change in precipitation patterns, snow and ice melting, sea level rise, increase of the frequency and intensity of extreme weather events. The

frequency increase of extreme weather events has a direct impact on agriculture production, especially severe droughts and extreme high or low temperatures. There is a tendency with temperature increase of the cereal productivity to increase at mid to high latitudes but to decrease at low latitudes. The changes in precipitation will affect the levels of rivers and lakes, limiting access to drinking water, for household use and agriculture use. Forecasts show that there will be a decrease in water availability at mid and low latitudes leading to a water stress for millions of people. The conservation of an ecosystem will be affected with the increase of species risk of extinction and coral bleaching. Also important is how climate change affects human health, and it will have three types of effects: direct effects of extreme climate events; effects caused by environmental damage and tertiary effects caused by the displacement of populations. Some of the potential climate changes scenarios for human health are: increased morbidity and mortality due to heat waves, floods or storms; greater incidence of infectious disease such as cholera, malaria and dengue fever; increased malnutrition, diarrhoea and cardiorespiratory diseases [3].

All these climate changes consequences and impacts are of complex understanding within Earth's interconnected systems and cycles and therefore, to address such problems is urgent, as the tipping point for humans to hold Earth's atmospheric temperature change under 1.5 ºC is almost "tipping", if not already crossed. The Representative Concentration Pathways (RCP) are projection model scenarios used to gather information about future emission and concentration of GHG, aerosols and climate drivers. They are based on a combination of climate models, atmospheric chemistry and global carbon cycle models [1]. In Figure 1.1, the predicted variation of the global temperature from multi-model simulated time series from 1950 to 2100 is different according to each RCP scenario. They concern the approximate total radiative force in year 2100 relative to 1750, as an example, 2.6 $W\ m^2$ for RCP 2.6. The RCP 2.6 represents a mitigation scenario of very low forcing level, the RCP 4.5 and RCP 6.0 correspond to two stabilization scenarios, and RCP 8.5 is a very high GHG emission scenario. By observing Figure

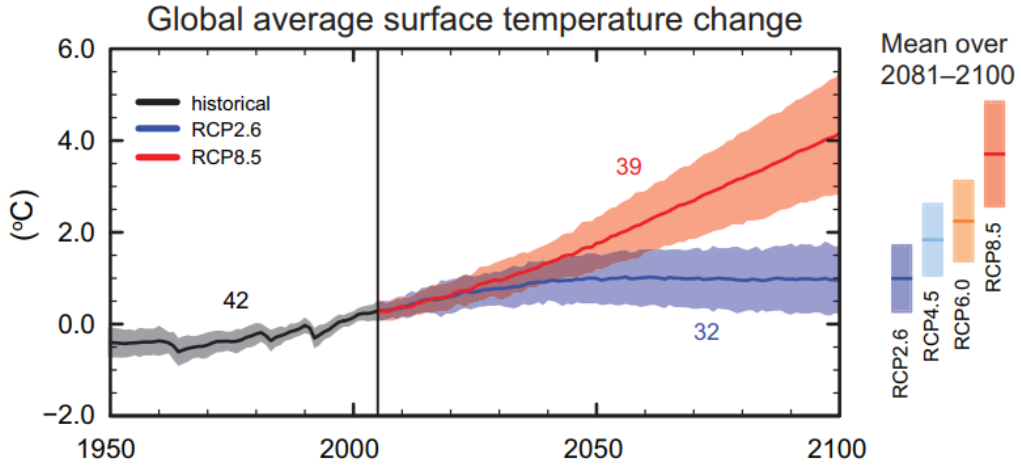

Figure 1.1: Change in global mean surface temperature [1].

1.1, the global temperature is likely to exceed 1.5 °C by the end of the current century relative to 1850 and 1900 for all RCP scenarios except RCP 2.6.

If such point is desired to avoid, the global greenhouse gas emissions must decline drastically. Figure 1.2 portraits the direct GHG emission shares, in % of all total anthropogenic GHG emissions, of five major economic sectors in 2010. The pull-out graphic shows the distribution of indirect carbon dioxide emissions shares from electricity and heat production. "AFOLU" stands for Agriculture, Forestry, and Other Land Use. The industry, AFOLU and energy supply sectors were the major contributors of the GHG emission levels. The total anthropogenic GHG emissions have risen more rapidly from 2000 to 2010 than in the previous three decades, as they have grown 1.0 $GtCO_2$ in 2010 compared to 0.4 $GtCO_2$ in 2000. Also, in these two referred periods, carbon dioxide emissions from fossil combustion and industrial processes were the cause of 78 % of the total GHG emissions [4].

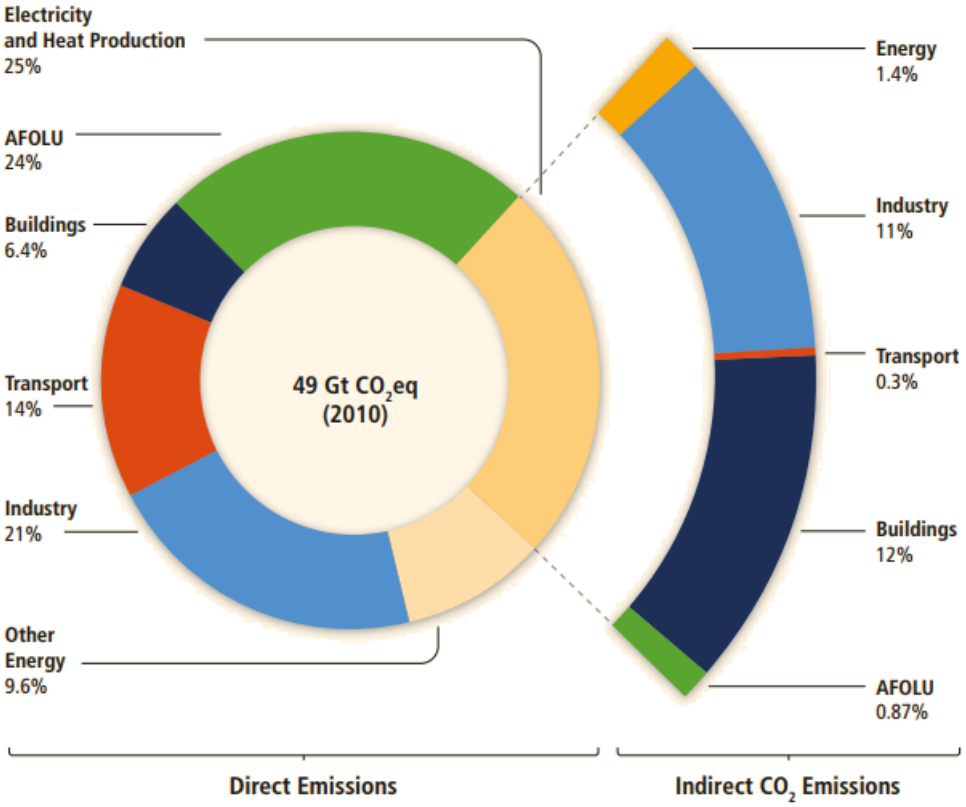

Figure 1.2: Greenhouse gas emissions by economic sector [4].

One way to mitigate greenhouse gas emissions, is the use of alternative methods in the energy supply sector. The use of renewable energy in form of wind, solar, biomass, hydric, geothermal and ocean power rather than the conventional use of coal, oil and gas, is a clean and reliable way of GHG emission reduction, a way of reaching a low carbon economy and a path for sustainable development. Within the last decade, a big push was done to promote initiatives for climate change mitigation. The engagement of non-state and subnational actors (NSAs) is a key role in mitigation and adaptation efforts. Their action may come in two categories:

individual NSA actions and cooperative actions by international cooperative initiatives (ICIs). An ICI is a transnational climate effort of non-state or subnational actors from at least two different countries. ICIs are important in a way that they reduce greenhouse gas emissions, pave the way for the establishment of low-emissions development strategies, ignite technology development and attract more initiatives with their momentum. In the Emissions Gap Report of 2018 from the United Nations Environment Programme, 244 ICIs were registered in the Climate Initiatives Platform, of which 220 are mitigation focused. In 2015, when COP 21 took place in Paris, 44 international cooperatives initiatives were launched, ten more than in 2014. Figure 1.3 shows an overview of the 220 mitigation-focused ICIs for several sectors, where the energy supply sector holds the most ICIs, around 70 % [5].

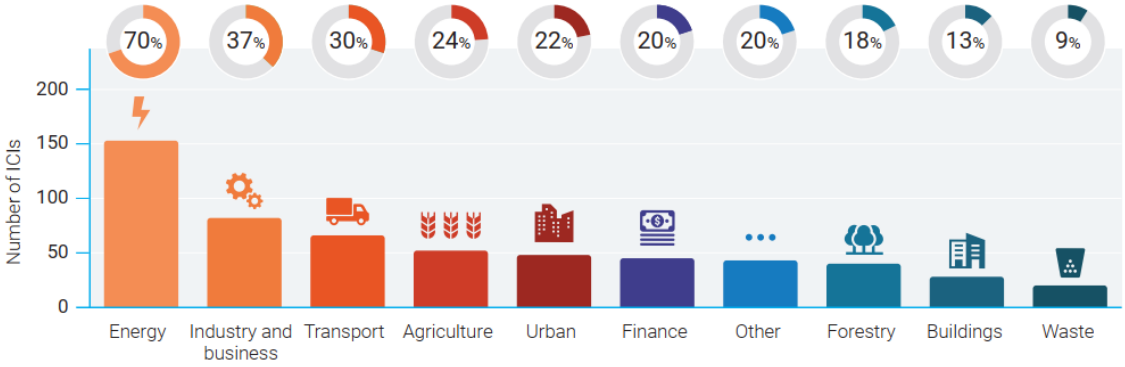

Figure 1.3: Sectoral coverage of international cooperative initiatives [5].

Recent statistics show that a huge push towards the increase of renewable energy installed capacity over the last decade has being made. Renewable energy can also provide extra benefits such as reducing negative impacts on the environment and health, energy access, be a secure energy supply and contribute to social and economic development in remote and poor rural areas. Renewable energy may be used to generate electricity, for heating and cooling and

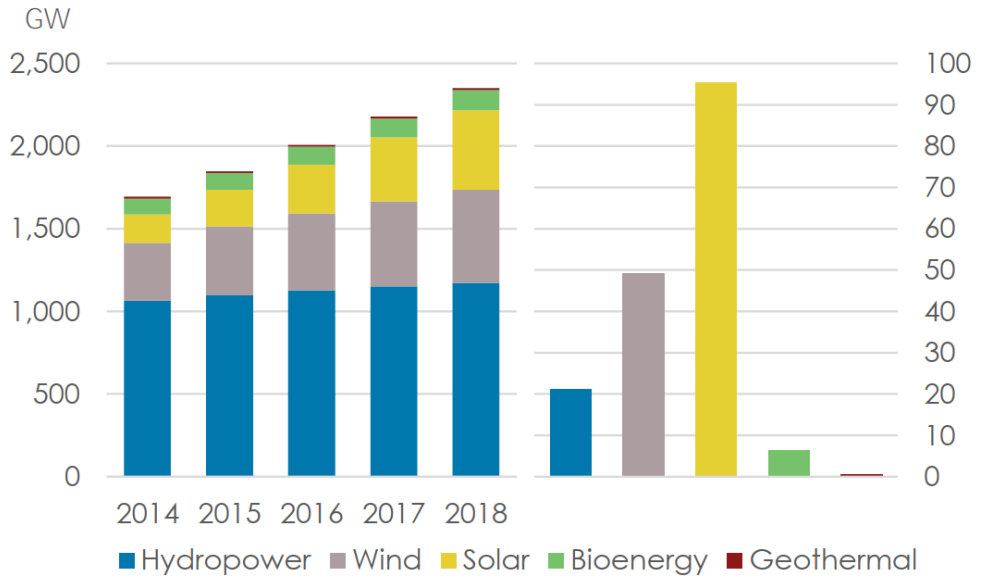

Figure 1.4: Renewable energy capacity growth (left) and capacity installed in 2018 (right) [6].

for the transport sector. In 2008, approximately 19 % of global electricity supply originated in renewable energy sources. Between 2008 and 2009, from the 300 GW of new electricity installed capacity, 140 GW concerned renewable sources. Figure 1.4 shows the global evolution of the cumulative capacity of renewable energy for electricity generation over the period of five years, reaching a total renewable energy capacity of 2,351 GW in 2018. The high amount of solar photovoltaics capacity installed goes in accordance to the trend seen in the right graphic of Figure 1.4 by the yellow columns. In 2018 there was an increase of 171 GW in global renewable energy capacity for electricity generation, of which 61 % was installed in Asia. Of the added 171 GW, wind and solar represent 84 %, with 49 GW and 94 GW respectively. Globally, there has been an increase of about 115 GW per year, on average, in non-renewable generation capacity, while renewable generation capacity increased from less than 20 GW in 2001 to around 160 GW or more in 2016, 2017 and 2018. The role of renewables sources in the share of total generation capacity in the world, improved from 22 % in 2001 to 33 % in 2018. In the same period, the global share of renewables in electricity generation capacity have increased from 25 % to 63 % [6].

In the European Union, 227 GW of renewable energy capacity for electricity generation was added between 2009 and 2018, reaching a cumulate capacity of 466 GW. In 2009, the installed capacity of renewable energy for electricity generation in Portugal accounted for 8.9 GW, and in 2018 the cumulative capacity performed up to 13.7 GW [7]. Renewables started to dispute the role of final gross electricity generation major provider in the European Union market, taking the first position in 2014, 2015 and 2016 as observed in Figure 1.5. With the increase of

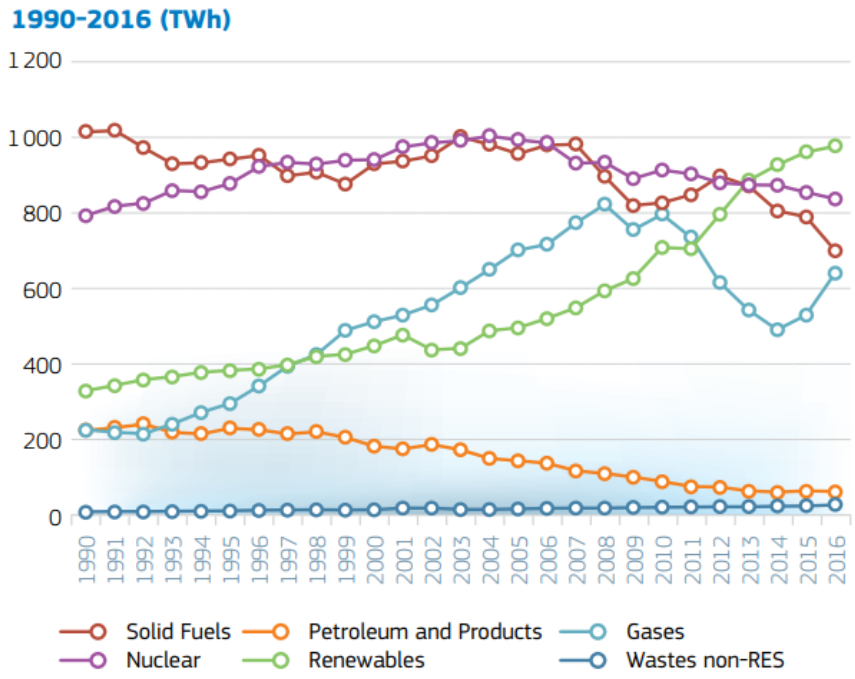

Figure 1.5: European Union gross electricity generation by fuel (adapted from [8]).

renewables electricity generation capacity and consequent production, non-renewables have decreased their production, thus leading to less greenhouse gases emissions. Figure 1.6 shows the gross electricity production for every renewable source in the European Union from 1990 to 2016, where it is observed the long reign of hydropower as the major provider of electricity production as well as wind power standing out as the second provider of electricity production since 2006. Although not displayed in Figure 1.6, in 2017, wind power accounted for 362 TWh of the electricity produced, while hydropower only produced 331 TWh, making wind power for the first time the major electricity provider within the European Union renewable mix. With the same trend observed in the European Union, renewables also play a key role in Portugal's electricity production mix. Portugal's gross electricity generation chart by fuel is displayed in the attachments, where is observed a clear decrease of electricity generated by Petroleum and Products [8].

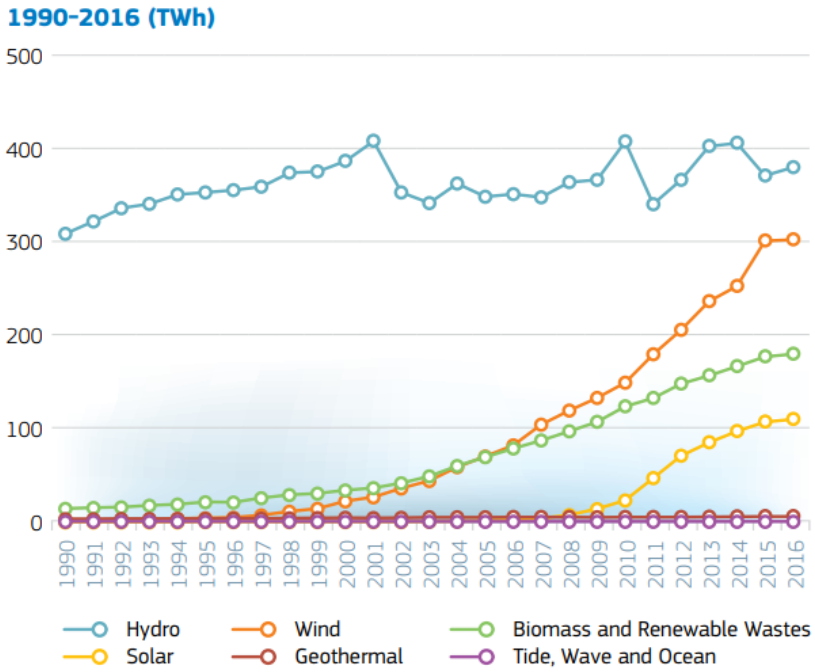

Figure 1.6: European Union renewable gross electricity production (adapted from [8]).

According to the Associação Portuguesa de Energias Renováveis - APREN statistics from 2017, Portugal's electricity production from renewable sources represented 42 % of the total electricity generated. Wind power and hydropower generated 21.6 % and 13.3 % of the total electricity generated respectively, meaning in a total electricity generated of 12.1 TWh and 7.4 TWh.

Globally, the installed capacity of wind power rose from 150 GW in 2009 to 563 GW in 2018. China, with 20 GW, holds the most wind power capacity added in 2018, followed by the United States of America with 7 GW. In Europe and Portugal, there was an increase of 106 GW and 1.8 GW, respectively, in wind power capacity between 2009 and 2018. Currently, Portugal holds 5.4 GW of onshore capacity [7].

Of the current 189 GW of wind power capacity in Europe, 65 % is installed in five countries (Germany, Spain, the UK, France and Italy). Up until recent years most of the wind power installations were onshore. Offshore installations have ascended in recent years as seen in Figure 1.7 by the light blue columns, prompting a considerable growth due to technological advancements such as foundations systems and loosen acoustic regulations. Onshore wind turbine installations in 2018 averaged a power rating of 2.7 MW, while the average capacity of offshore installations was 6.8 MW. The most added capacity was recorded in 2017 with 17,1 GW, with Germany installing a total (onshore and offshore) of 6.5 GW capacity [9]. Of the 10.1 GW added in 2018, 65 % of the installations belong to Germany, the United Kingdom, France and Sweden. Although with less capacity added compared to 2017, Germany installed a total of 3.3 GW of wind power in 2018, currently holding 59.3 GW of cumulative onshore and offshore capacity, followed by Spain with 23.5 GW of only onshore capacity [10].

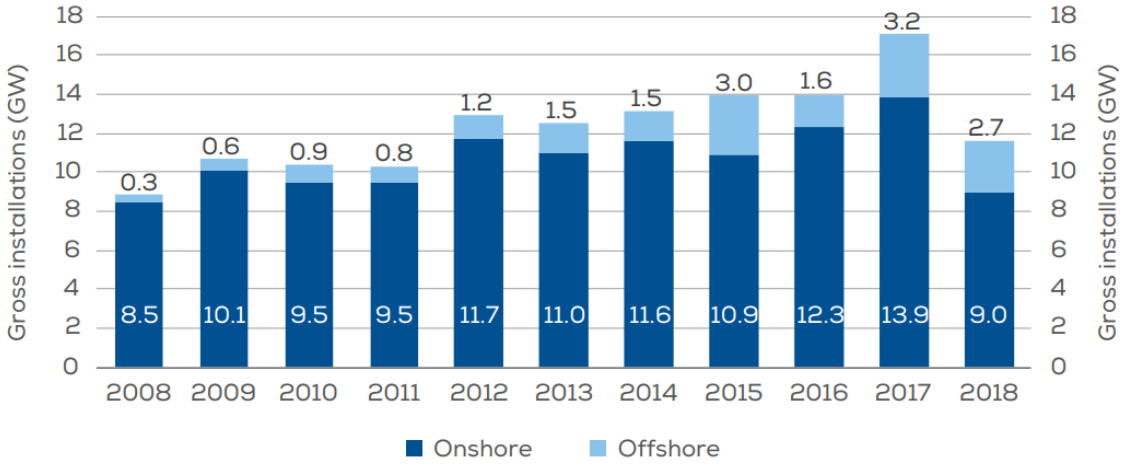

Figure 1.7: Added capacity of onshore and offshore installations in Europe [10].

With all this capacity installed, Europe can cover a reasonable electricity demand with wind as an energy source. For example, in 2018, 14 % of European Union's electricity demand was generated by wind power with a total wind energy production of 362 TWh, 2 % higher than in 2017. Denmark covered 41 % of its average annual electricity demand with wind in 2018, followed by Ireland and Portugal with a share of 28 % and 24 % respectively. In the previous year, the same countries reported a share of 44.4 %, 24 % and 24.2 % correspondingly. On December the 8th, wind energy registered a peak production of 98 GW, supplying one third of Europe's electricity demand [10].

One of the direct socio-economic benefits from the use of renewables, is the gradual drop of a country energy dependence from fossil fuels. As it is logical, renewables will decrease fossil fuels extraction, if such nation has them as natural resources. Otherwise, if a country relies primarily on imported energy fuels, the use of renewables will allow for economic savings in the balance of trade. Taking Portugal as example, the increased use of the renewable generated electricity allowed in 2017, a spare of 770 M € in gas and coal imports, as well as 40

M € less in carbon dioxide emissions permits. From 2010 to 2017, Portugal saved 6,030 M € in fossil fuel imports and 524 M € in carbon dioxide permits. The specific emissions of the electricity sector in Portugal was of 360 g/kWh in 2017, a reduction in 50 % compared to 1999 when they were at 631 g/kWh [11].

Another driven benefit from renewable energy is employment. In 2017, the global renewable energy industry employed 10.3 million people, representing a growth of 5.3 % compared to the previous year. China alone accounts for 40 % with over 4.1 million jobs. The solar photovoltaic industry has been through a notable growth over the last years with an increase of 8.7 % compared to 2016, leading the employment rate with 3.3 million jobs. A chart of the global RE employment by technology between 2012 and 2017 is displayed in Appendix A. The second industry with most people employed is liquid biofuels with 1.9 million jobs, followed by large hydropower (>10 MW) employing 1.5 million people. Wind power comes in the fourth position employing 1.15 million people across the globe, a decrease of 0.6 % from 2016. China, Germany, the United States of America, India and the United Kingdom represent 76 % of the total jobs in the wind segment. Again, China holds the first place with 44 % of the global wind employment. Europe accounts for 30 % of the wind employment and is a global technology leader especially in the offshore sector. The statistic from 2016 portraits a sector with 344,000 jobs in Europe, representing an increase of 15 % over the previous year [12]. In 2010, there were 41,542 people employed in the Portuguese RE sector, a value that increased to 55,275 jobs in 2017.

All the previous statistics concern large scale wind turbines, grouped into farms which provide power to the electrical grid. By definition, a large-scale wind turbine, although there is no clear and concise establishment, is a wind energy conversion system with a rated capacity of more than 1 MW, or with a rotor diameter superior than 50 m. The current biggest wind turbine belongs to the joint company between Mitsubishi Heavy Industries and Vestas, and it was installed in 2018 in the United Kingdom. The V164-8.8 MW offshore wind turbine that was upgraded from the 8.0 MW version, has a rotor diameter of 164 m and a power rating of 8.8 MW. Nevertheless, the joint company launched during 2018 the V164-10.0 MW offshore wind turbine, and in 2019, the V174-9.5 MW offshore wind turbine with a rotor diameter of 174 m was introduced to the market. One V164.10.0 MW wind turbine can power up to 9,000 UK households. Nevertheless, GE Renewable Energy is another competitor in the offshore industry with the Haliade 150-6MW, a wind turbine with a rotor diameter of 150 m, blades with 73.5 m length, capable of supplying enough electricity for 5,000 European households. The pursuit for better and more efficient wind turbines, has led to the launch of the Haliade-X 12 MW with a 220 m rotor diameter, featuring a 107 m blade and a capacity of 12 MW. Upon its installation, the Haliade-X will become the biggest and most efficient offshore wind turbine, capable of generating clean power to supply 16,000 European households [13] [14].

Objective

This dissertation purpose is to investigate the hypothetic effect that a shape modification on a wind turbine rotor would enforce on its performance. A graphic user friendly open source software, QBlade, is used to perform the rotor shape modification and to simulate the wind turbine performance. In order to accomplish this objective, intermediate tasks are required such as:

- Performance simulation of the "original" wind turbine;
- Shape modification by smoothing the rotor airfoils leading edge towards the lower surface;
- Performance simulation of the new wind turbine;
- Performance comparison and analysis.

Structure

Several chapters compose the lay out of this dissertation.

The first chapter introduces the importance wind power has and will have, to mitigate climate change effects and to ensure a sustainable development for our planet. The dissertation main objective is presented, and the document guidelines are introduced.

Chapter 2 exposes a literature review, starting by exposing a historical evolution of what is nowadays the concept of a wind turbine. The physics behind wind motion is then explained in the second section, followed by a description of modern wind turbines configuration. The aerodynamic theory that QBlade uses for wind turbines performance simulation is settled in the fourth section and the last section exposes what has been scientifically done on the investigation of small horizonal axis wind turbines performance.

The methodology applied in this study is described in the third chapter. In first place, the construction process of the Hugh Piggott wind turbine is shown in order to understand how the rotor is made of three different blades, and secondly, QBlade's structure and functionalities are presented. After, the process of modifying the airfoils shape and the efficiency simulation of the Piggott and the new rotor is depicted step by step. Another section addresses how both rotors power efficiency was compared, and the last section portrays a flowchart of the general methodology process.

In the fourth chapter, made of 6 sections, the results of the simulations are displayed and discussed. The first section compares the simulation results of the Piggott wind turbine from the work of (Monteiro et al) and from the ones obtained in this study, while the second section

reflects the effect of the airfoil refinement in the simulations accuracy. The results from the polar analysis of the Piggott and the modified airfoils are illustrated in the third section. As there are geometric differences between blades, the fourth section addresses the simulations performed for each blade assuming an ideal rotor that consists of three equal blades. By averaging the results from the three ideal rotors, an approximate performance for the real rotor is presented. Subchapter 4.6 presents the analysis of both rotors power output for a hypothetic scenario where the wind turbine would work at a constant rotational speed. Chapter's 4 last section concerns about the best blade airfoil comparison and selection regarding the same blade cross section, and the performance comparison between the averaged results of Subchapter 4.4, and an optimized turbine made with the best modified airfoil of each cross section.

Chapter 5 contains the conclusions withdrawn from the previous chapter and declares whether this dissertation objective was successful or not.

Chapter 2

Literature Review

2.1 Historical Perspective

The use of wind as a source of mechanical power for activities such as grinding grain, pumping water or cutting, lasts at least for the past 2000 years. Also, wind was largely used, and it is still used in the present time to power ships using sails. Only in the turning of the nineteenth century due to technological outbreaks, electricity started to be produced from what is nowadays called a wind turbine.

2.1.1 The Windmill

The windmill is a machine that converts the wind's power into mechanical power. Around the windmill literature, authors agree to accept the Persian windmill as the first historical documented reference of a windmill. The Persian windmill (Figure 2.1), a vertical axis windmill that dates to the tenth century [16], is also known as the Seistan windmill due to the windy conditions of that Persian region (now Eastern Iran [17]), said to reach 45 m/s windspeeds for four months between spring and summer.

Figure 2.1: Seistan Windmill [17].

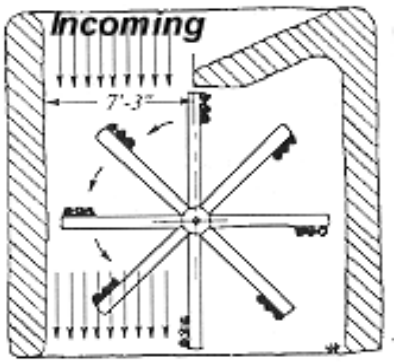

Figure 2.2: Seistan windmill shematic top view [18].

Driven by drag forces, the Seistan windmill was inefficient and vulnerable to damage in high winds. Figure 2.2 illustrates how the windmill was enclosed between walls that acted as a convergent to impose the wind towards the sails [19].

In Northwest Europe, the horizontal axis windmill, in which the shaft was placed horizontally, was born in the late twelfth century. Several hundred mills were registered in England by 1086 in the Doomsday Book, but no note was taken on what type they were [19]. Of 23 English

windmills dated before the year 1200, 15 are dated in the 1190's, five before 1200 and the remaining three in the 1180's. In the following century, windmills started to become common in Northwest Europe, being a major source of power in the fourteenth century [16].

The European windmill had horizontal axis and was driven by lift forces, being used for mechanical purposes like water pumping, grinding grain, sawing wood or even to power tools. These early mills had four sails, each set at a small angle with respect to the wheel plane of rotation, and were built on posts so that, when the wind changed its direction, they could be turned to face it. This post construction become later known as the Post-Mill design (Figure 2.3). These axes transition reported some engineering problems like the transmission of power from a horizontal rotor shaft to a vertical one; turning the mill into the wind; and stopping the rotor when necessary. Using a cog-and-ring gear mechanism designed by Vitruvius for the horizontal-axis water wheel solved the first problem while the second issue was overcome by rotating the whole system on a central spindle. Stopping the rotor could be solved by facing the rotor out of the wind and applying a frictional braking on the larger gear of the cog-and-ring gear mechanism [16].

Figure 2.3: Post-Mill design [17].

The Industrial Revolution marked the turning point for wind and water as a main source of energy, but more drastic for wind. Steam engines powered by coal provided a more compact and powerful source of energy. Coal had the advantage that it could be transported and used when it was needed, as well, in a certain way, did water. In its turning point, the European windmill reached a whole new level of design and technology due to the will of building larger mills. The challenge was to rotate only the upper part (sails, windshaft and brake wheel) of the mill to face the wind instead of rotating the whole body of the windmill. An example of a Tower-Mill design (or smock windmill) can be seen in Figure 2.4. It is necessary to say that there is no adequate record of the windmill technology development throughout its history until the Industrial Revolution, and most of the assumptions rely on drawings, illustrations, descriptions

or carvings that had little detail. Windmill sails started to get a certain degree and twist. The common sail, mostly developed in Northwest Europe, was given a twist from the root to the tip while the previous sails had a constant angle to the plane of rotation of about 20º [16].

Figure 2.4: European smock mill [17].

The Industrial Revolution was a time rich in mechanical development that lead to the improvement of the windmill control devices such as mechanically change the sail setting; improve braking and automatically wind the mill. One major development was the invention of the fantail that allow to ease the work of the miller to turn the windmill manually. During the eighteenth century, the windmill started to be scientifically studied and tested. Civil engineer John Smeaton born in England [16], carried out important work that would lead to the basic rules of windmill performance. Using a device that himself mounted and improved from other's work, Figure 2.5 illustrates his model on a whirling arm. Even in the absence of most of laws of energy, his model allowed him to run tests at constant speeds and taking measures, laying down design and performance principles. Three basic rules that are still important that come from his findings are [17]:

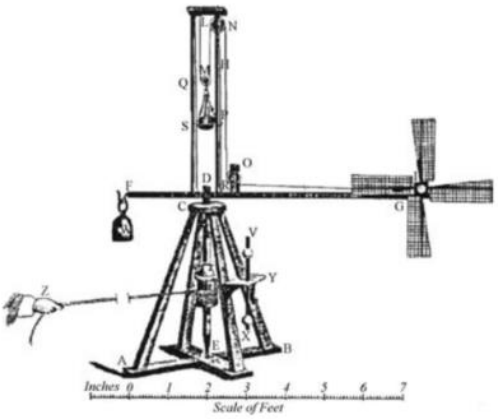

Figure 2.5: Smeaton's laboratory windmill rotor testing apparatus [17].

- The speed of the blade tip is ideally proportional to the speed of wind;
- The maximum torque is proportional to the speed of wind squared;
- The maximum power is proportional to the speed of wind cubed.

The windmill use reached its apogee in the seventeenth and eighteenth centuries as new energy sources, that provided power from the combustion of fuel, took place. Although its use may have declined, it continued into the twentieth century supplying isolated populated areas where small amounts of power were required but constant availability was not essential. The typical European windmill in the late nineteenth century, used a 25 m in diameter rotor. In the start of the century, in France there was about 20,000 of these European windmills and in the Netherlands, the industry used wind energy to power 90% of its activity. Still in the early twentieth century, Germany had more than 18,000 windmills and 11 % of the Dutch industry was based on wind energy [20].

With no association to the milling of grain, the term wind turbine is nowadays established as the machine capable of harnessing the wind energy for different applications together with several other devices that complete a power plant, such as mechanical transmission, nacelle, tower and control gear [16].

2.1.2 Wind-powered Generation of Electricity

The high cost of running transmission and distribution lines from central stations to dispersed habitations and the first appearances of small electrical generators at the end of the nineteenth century would encourage people to use wind for electricity generation. In the United States of America, Charles F. Brush, inventor, builder and industrialist in the electrical field, erected in 1888 a pioneer windmill-generator named the Brush windmill (Figure 2.6). Being the first windmill to generate electricity it had a post mill configuration, and the rotor with 144 blades was 17 m in diameter on a tower 18 m high. The rotor was a solid-wheel type, with a tail vane area of 112 square meters. It ran for 20 years until 1908 supplying 12 Kw of DC power for charging batteries mostly for 350 incandescent lights. Charles' windmill was a landmark in the multivane type. It was one among the largest built; it introduced the high step-up ratio (50:1) to windmill transmissions, assured by two belt-and-pulley sets in tandem to produce a full load dynamo of 500 rpm; and it was the first to mix structural and aerodynamic windmill features with the recent electrical technology [16].

In 1891, Danish professor and scientist Poul LaCour [19] was chosen to accomplish scientific research at the windmill experimental station established by the Danish State at Askov. LaCour was one of the most important pioneers in the transition from windmills to wind turbines. Introducing principles of the new science of aerodynamics, LaCour research purpose was to improve the rotor performance and the electricity output via wind-powered machines. LaCour

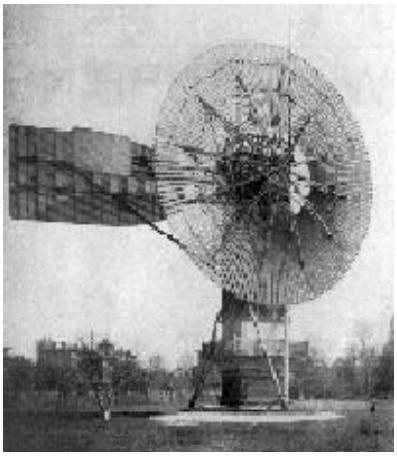

Figure 2.6: Brush Windmill in 1888 in Cleveland, Ohio [18].

was one the first persons in the world to use a wind tunnel. The LaCour turbine rotor was composed by plane and rectangular blades with a swept area of up to 23 m in diameter supported on steel framework towers with 23 m high [19]. One notable feature, was that LaCour used energy produced from the wind to electrolyse water, resulting in hydrogen that was burnt to illuminate his laboratory. Around 1910, villages around Denmark were electrically powered by these machines, equipped with 100 to 300 Ampere-hour capacity storage batteries. During windless periods these machines could meet demands up to 10 days.

2.1.3 Wind Turbine Generators

Until World War II, wind-generated electricity was mostly used to generate DC current to charge batteries. The development of the aeronautical science in the early twentieth century inspired the application of the propeller studies to the wind turbine. This led to the initial use of aerodynamic profiles and improvement in the power coefficient [19]. In the United States of America, small wind turbine generators become widespread after the Brush windmill. Being mostly pioneered by Marcellus and Joseph Jacobs, which they started to develop in 1925, their three-bladed rotors had high performance, minimal maintenance and good structural integrity (Figure 2.7). A 32-V DC model could produce 2,500 W and a 110-V DC generator delivered up to 3,000 W [16]. Jacobs rotor most notable feature was the passive pitch control system where the blades feathered with increasing rotor speed.

The early 1930's saw the introduction of an innovative vertical axis wind turbine patented by French engineer Darrieus, having two or three curved blades attached top and bottom to a central shaft. Darrieus also designed a two-bladed horizontal axis turbine with 20 m in diameter with a maximum power coefficient of 0.347 [19]. In the same decade the wind turbine configuration had settled down having a horizontal axis three bladed rotor upwind of the tower, working at variable speed with its blades at a fixed pitch angle. Even though these machines, generating low-voltage direct current, were reliable and with little maintenance, they did not

Figure 2.7: Jacob's turbine [17].

have the chance to stand against central stations power as a source of electrical energy. After World War II, along with the first concerns that fossil fuels reserves were finite, with fuel shortages and an increasing knowledge of aerodynamics, the development of larger wind power plants was getting more attention. However, some large-scale wind turbines had been already constructed prior to World War II. The Union of Soviet Socialists Republics took the first step by constructing a 100-kW 30 m diameter wind turbine in 1931 at Yalta on the Black Sea [19]. Being a three bladed rotor, it outputted a maximum coefficient power of 0.162 and it was the first wind powered system to be connected to an existing grid.

Other major achievement of the early large-scale wind turbine is credited to American engineer Palmer C. Putnam that stated that large wind turbines should supplement central power plants. In 1934 he got the S. Morgan Smith Company of York, Pennsylvania (known for manufacturing hydraulic turbines and electrical equipment) to fund its megawatt wind turbine generator prototype [19]. On October 10, 1941, the two bladed rotor, 53.3 m in diameter and with the synchronous generator, delivered electricity to the network for the first time [16].

To close this section about wind turbine generators, one final note is made to the implemention of an electric motor to turn the rotor into the wind by Danish F.L Smidth Company [19]. Developed by Johannes Juul after World War II, the Gedser turbine as it is known due to the location where it was installed, used an induction generator and aerodynamic stall for power control [17]. Between 1956 and 1967 it generated about 2.2 million kWh [21].

2.2 The Wind

Wind is air in motion relative to Earth's surface. Ultimately, the Sun is responsible for air motion by the pressure differences created by the uneven heating of the Earth surface, with more radiation absorbed at the equator than at the poles. This energy absorbed by the Earth's surface is then mostly transferred back into the atmosphere, creating variations in temperature,

pressure and density, setting up convective forces in the lower layer (troposphere). This result, globally, in hot air to rise at the tropics and flow to the poles. Locally, heated air rises creating depressions [22].

Another important factor in the air movement is the Earth's rotation, resulting in two aspects. One of them, the Coriolis force that act upon an air particle, accelerates it to the right of its direction of motion in the Northern hemisphere and to the left in the Southern hemisphere. The other effect accounts that an air particle has an angular momentum from the west to east, and as it moves closer to the poles (but remaining at the same altitude) it reaches the axis of rotation, where according to the conversation of angular momentum the velocity of the air particle increases [21]. This second effect is more apparent at middle latitudes and originates the Westerlies winds which are the ones better suited to extract energy This explanation is a general one for a spherical model surface and accounts as a large-scale atmospheric circulation. Local effects must be taken in account such as orography, roughness or the fact that landmasses heat and cool faster than water masses. Hurricanes, monsoons or cyclones constitute the secondary circulation scale, while an example of tertiary circulation is land and sea breezes, valley and mountain winds, or thunderstorms or tornadoes [23]. In Figure 2.8, an example of tertiary circulation is visible, where during the day, the air in the top gets warmer and rises creating a pressure difference due to the cold air in the valley. Hence the air moves towards the top and at night the opposite happens.

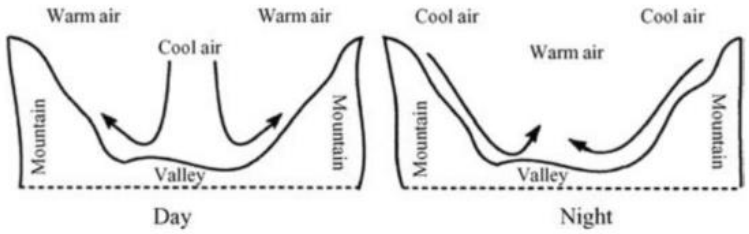

Figure 2.8: Diurnal and nocturnal tertiary circulation [23].

2.2.1. Weibull Distribution

Before even wind turbines can be designed, a complex siting process most occur to evaluate where to install the wind turbine or the wind farm in order to maximize the performance while reducing parameters such as noise, environmental and visual impacts, and overall cost of energy. Thus, estimating the wind resource of a certain location is one of the many fundamental aspects to take in account. In the final wind assessment evaluation, the desire is to have a detailed spatial variability of the wind resource across the studied location and the temporal variation over longer time scales. Some of the methods used to determine the wind resource at a certain location are ecological methods, the use of wind atlas data, computer modelling, mesoscale weather modelling, statistical methods and long-term site specific data collection [24].

Frequency distribution of wind speed and persistence are two parameters commonly used to characterize the wind resource of a certain site. Persistence gives the statistics on the continuous time the wind maintains a certain speed, while the frequency shows the cumulative time the wind blows at a given value. They are important factors for wind turbine design and siting as the frequency distribution allows to calculate the energy input of the wind turbine and persistence the assessment of the wind energy potential [20]. To assess this frequency distribution, several non-Gaussian distributions were suggested being the Weibull distribution the one that ended having the most use for wind load and energy assessment studies. The Weibull probability density function is given by:

$$p(U) = \left(\frac{k}{A}\right)\left(\frac{U}{A}\right)^{-1} exp\left[-\left(\frac{U}{A}\right)^{k}\right] \quad (2.1)$$

Where k is the shape factor, A the scale factor (m/s) and U the free stream wind speed (m/s).

In Figure 2.9, it is visible the sharpening of the curve with the increase of the shape factor meaning there will be less wind variation and higher wind speeds will be less probable. Also, the increase of the shape factor tends to turn the curve into a Gaussian distribution for shape factors over 3. On the other hand, Figure 2.10 illustrates that the increase of the scale factor will extend the curve over the X-axis meaning the higher probability of occurring higher wind speeds at a hypothetical location.

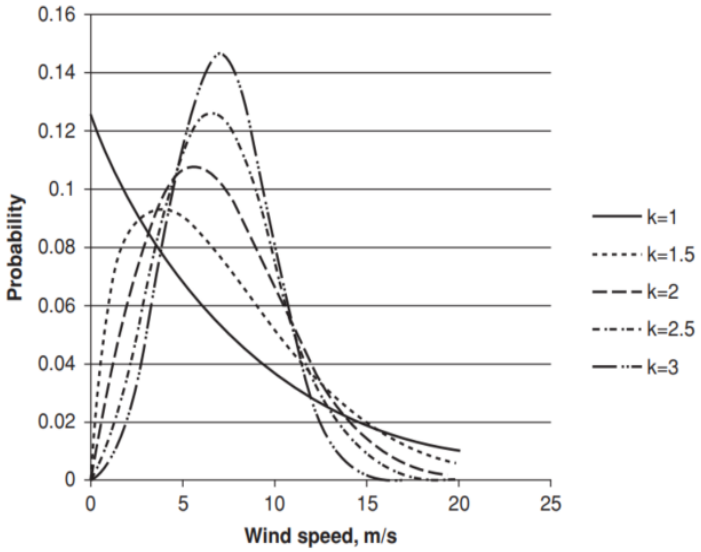

Figure 2.9: Weibull probability density function for A = 8 m/s [22].

To summarize, it is important to notice that with wind speeds measurements throughout a year, it is possible to view that strong winds are rare while moderate winds are more common. The mean wind speed or the scale factor say how windy in average the location is, while the shape factor tells if the wind speeds tend to be close to a certain value, the distribution will have a high shape factor and will be very peaked.

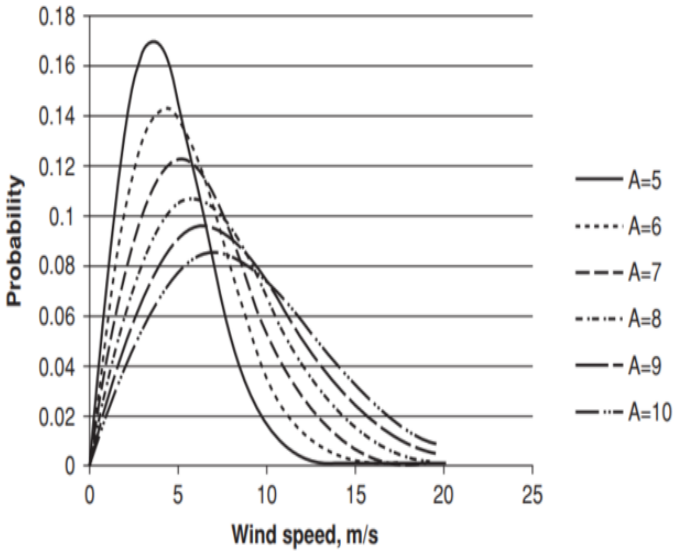

Figure 2.10: Weibull probability density function for k = 2 [22].

2.3 Modern Wind Turbines

The current term wind turbine is shortened from wind turbine generator, name given if the wind machine final purpose is the production of electricity through a generator rotated by the force wind imposes upon the rotor. To give a brief sight about the principle used by any wind turbine it is necessary to refer to the typical aircraft propeller as a rotary mechanism shaped by airfoils that imposes energy (from an external source) into the fluid producing a thrust force in the sense of the movement [25]. However, the wind turbine does the reverse, where it extracts the available power in the fluid stream producing a drag force in the sense of the flow. Withdrawing the scientific words, the goal of a propeller is to push the air through, while wind turbines seize the air displacement. Any wind conversion energy system can be divided according to if they are driven aerodynamically by lift or drag.

2.3.1 Types of Wind Turbines

As said above, wind turbines are defined as lift or drag driven. These two terms will be further explained in detail. Also, during the historical perspective, the horizontal and vertical axis terms were introduced. Although the reference to the wind turbine development in Subchapter 2.1 stagnated little after World War II, the concept of the wind turbine to supply electricity evolved to what it is known nowadays as several wind turbines making up a wind farm for electricity production and distribution to the network. Prior to World War II little development took place mostly in western Europe. It was only when the 1970' oil crisis struck that the interest in wind energy rose, with a lot of efforts taken by the United States of America, Germany, Denmark and Sweden [21]. By the end of the twentieth century, the largest US wind turbine manufacturer Kennetch Windpower, moved to Europe where, with the apprehension of

nuclear power and the ever-common effects of global warming being felt, an even stronger push for wind energy took place [17].

Nowadays, the most common type of wind turbine for commercial applications is the horizontal axis wind turbine, also known as HAWT and referred as “propeller-type” due to the basic principles of an aircraft propeller that are applied to HAWT rotors. Generally, a wind energy conversion system is composed of some subsystems such as the rotor, the power train, the nacelle, the tower structure, the foundation, power control and the ground equipment station. Horizontal and vertical-axis turbines share most of these subsystems and components, but some of the configurations are different. For example, a VAWT does not need a yaw mechanism as it accepts winds from any direction. To summarize, wind turbines can be classified according to its design (vertical or horizontal) and according to its size or power rating. Horizontal axis wind turbines with rotors less than 12 m in diameter are classified being small scale; from 12 m to 45 m they are medium scale and over 46 m they are large scale. For power rating, small-scale wind turbine are the ones with less than 40 kW; between 40 kW and 1 MW they are classified as medium-scale and large-scale for more than 1 MW [26]. Throughout the second half of the twentieth century different concepts of wind turbines beyond the traditional HAWT and VAWT were designed and built. None of them will be explained in detail but Figures 2.11 and 2.12 summarize most of the concepts invented.

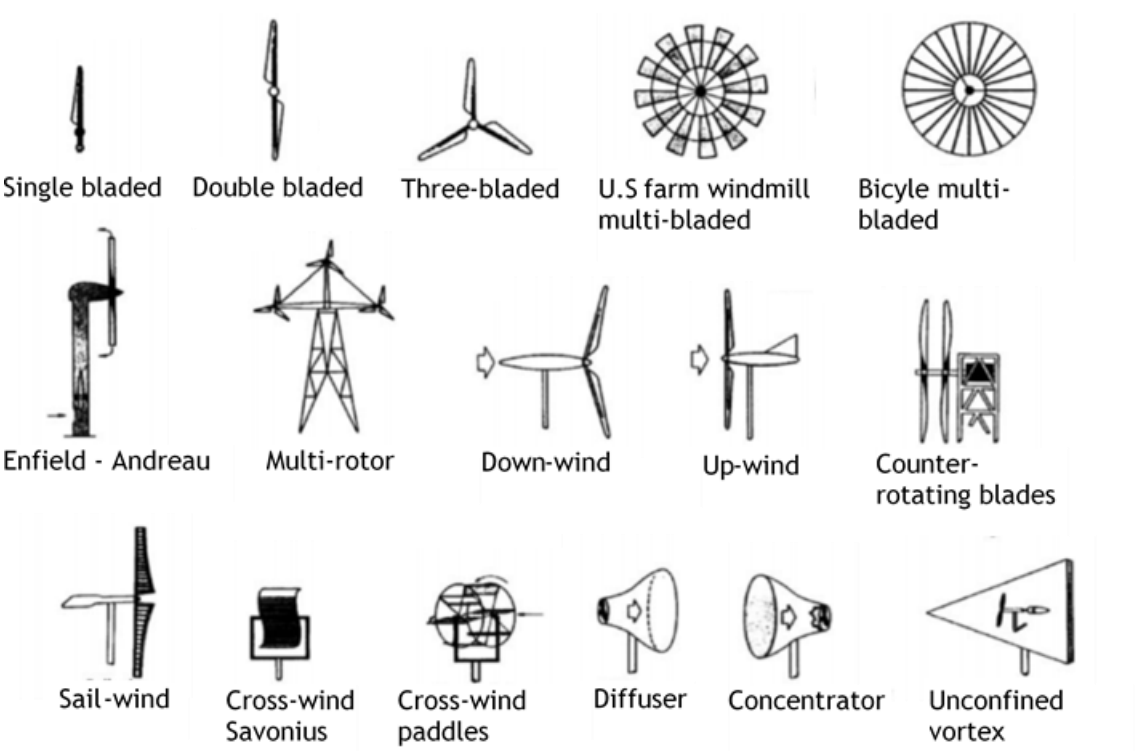

Figure 2.11: Different horizontal axis turbine concepts (adapted from [17]).

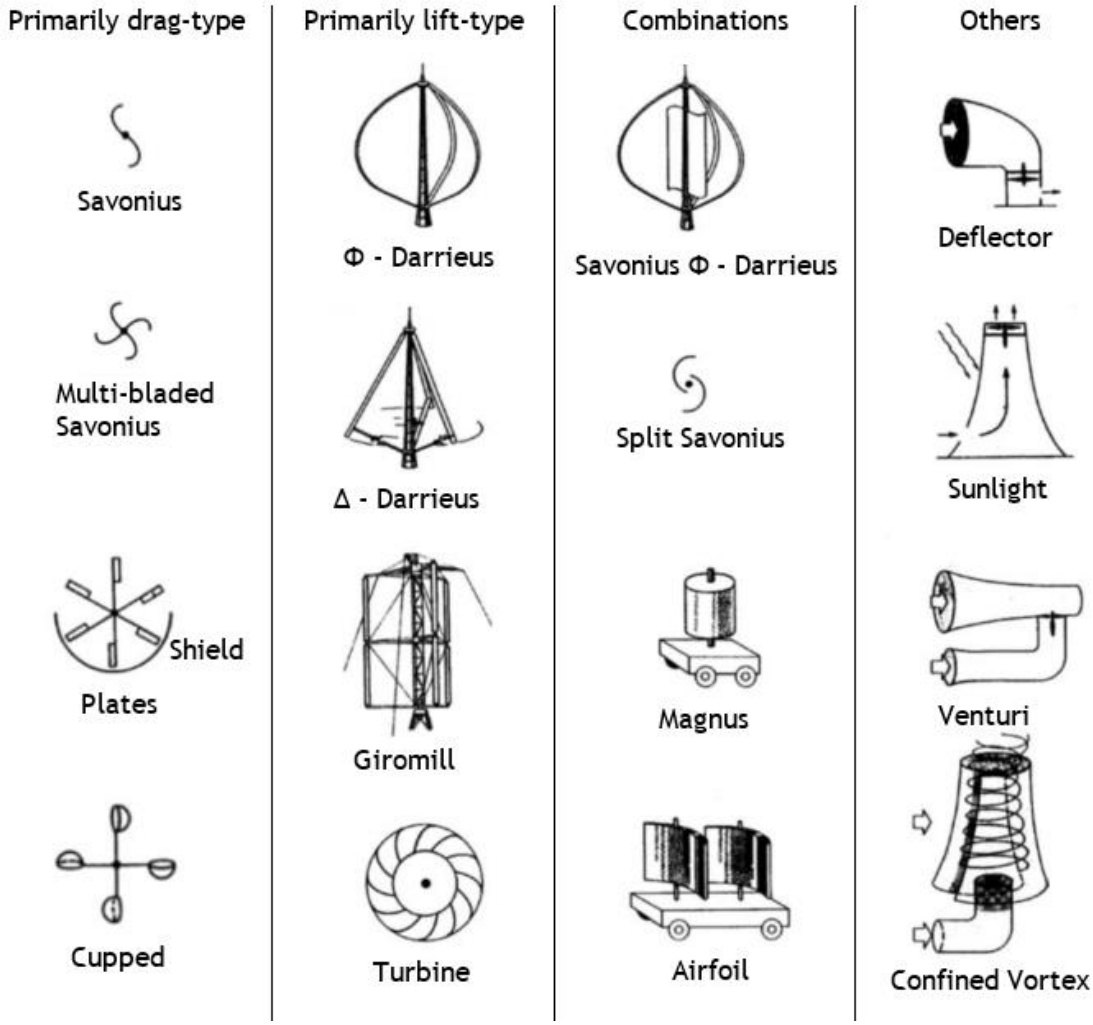

Figure 2.12: Different vertical axis turbine concepts (adapted from [17]).

2.3.2 Small Wind Turbines

As the wind turbine that is studied in this work is of a small-scale, it is logical to present a general overview on the small-scale wind turbine systems. During the 1970's, a big push by the United States of America government was made as little performance or engineering data was available for the small-scale application. Analytical and experimental projects were performed under the Federal Wind Energy Program that gave results for later development and assessment of small-scale turbines [27]. In a typical small-scale HAWT, the rotor, tower and power train are the fundamental subsystems. Most commercial small wind turbines are horizontal axis, have an upwind configuration and have passive controlled systems for speed and power regulation. Upwind or downwind refers to the location of the rotor with respect to the tower. Some small wind turbines have fixed pitch blades, as variable pitch mechanisms are costly and require periodic maintenance, relying then on aerodynamic stall to limit peak power. As mentioned before, Jacob's turbine used a fly-ball governor activated by centrifugal forces to mechanically change the pitch of its blades. A model employed and patented by Bergey Windpower Company

[26], used weights at the blade tips to twist them to their optimum position, though it did not limited power but helped to start the rotor rotate in low winds.

Whereas in larger-scale wind turbines, yaw control is done by rotating the nacelle to face the rotor to the wind with the use of an electric motor, in a small-scale this is done by weather-vaning. The turbine turns on a bearing by the action of wind forces upon the tail vane. Referring to this mechanism is implicit to note the furling mechanism, that protects the rotor from extreme high speeds and prevent the generator from overheating if not stopped. At high wind speeds vertical furling will tilt the rotor upwards and horizontal furling faces the rotor towards the tail vane. The axial force that acts on the rotor (thrust) causes a yawing moment which thanks to a leverage turns the rotor out of the wind.

Small turbines have generally three blades due to higher dynamic stability than one or two bladed rotors. Blades are often made of wood or wood-epoxy laminates that can be carved or molded but some concepts were made with cloth, fiberglass or laminates. As small turbines operate at different windspeeds it is important to control the rotor in high winds in order to waste the excess power. Mechanical brakes applied to the generator drive shaft are often the usual solution. Another form to control the rotor for small scale wind turbines are blade tip devices, where the outer section of the blade is turned, making the rotor to stop by aerodynamic drag or reducing its speed. There are three types of tip devices which are tip brakes, buckets and pitchable tips [26].

Tower configuration for small wind turbines tend to have a higher height to rotor diameter ratio in order to place the rotor to catch more energetic wind and to get above near obstacles. Some configurations are: shell, stepped shell, lattice or guyed shell. Tower materials for small scale wind turbine range from wood, fiberglass, concrete or tubular steel.

As small wind turbines operate with higher rotor speed than the counterpart large commercial wind turbines, the tradeoff of the transmission-generation system is different. The power train subsystem in general consists of a turbine shaft, a gearbox, a generator drive shaft, a rotor brake and an electrical generator. Most small turbine are direct-driven to the rotor with permanent magnet generators, with no gearbox, turbine shaft or generator drive shaft, but this design does require a converter to obtain a constant frequency [21].

2.4 HAWT Aerodynamics Basics

2.4.1 One-dimensional Momentum Theory

The power production of a wind turbine depends on the interaction between the rotor and the wind, thus the importance of further comprehension about the aerodynamic forces involved in

this energy exchange process. The aerodynamic analysis is important to predict the turbine performance, starting with the energy extraction process by explaining the axial momentum theory, also known as the Actuator Disk Theory. Being a simple model sustained with the fundamental principles of the mechanics of fluids (mass conservation, momentum theorem and energy conservation), it can be used to calculate the power output of an ideal turbine rotor. It was first originated by Rankine in 1865 and later developed by Froude for the analysis of the marine propeller [28]. The one-dimensional momentum theory assumes a control volume, where the control boundaries are the surface of a stream tube. The rotor with a finite number of blades is assumed as a rotor with an infinite number of blades, each of them giving an infinitesimally small contribution to the thrust force. To develop the one-dimensional momentum theory the following must be assumed [28]:

- A slipstream separating the flow passing through the rotor disc from that outside the disk;
- No frictional drag;
- Uniform thrust loading over the disk rotor;
- No rotation is communicated to the flow by the disc
- The static pressure far upstream and far downstream of the rotor is equal to the undisturbed ambient static pressure.

In Figure 2.13, the numbers below the stream tube are the considered sections for the development of the theory, being 1, 2 ,3 and 4, the far upstream the rotor, just before the rotor, just after the rotor and far downstream of the rotor respectively. The flow enters the stream tube, being deaccelerated by the rotor disk, leaving in the end of the stream tube.

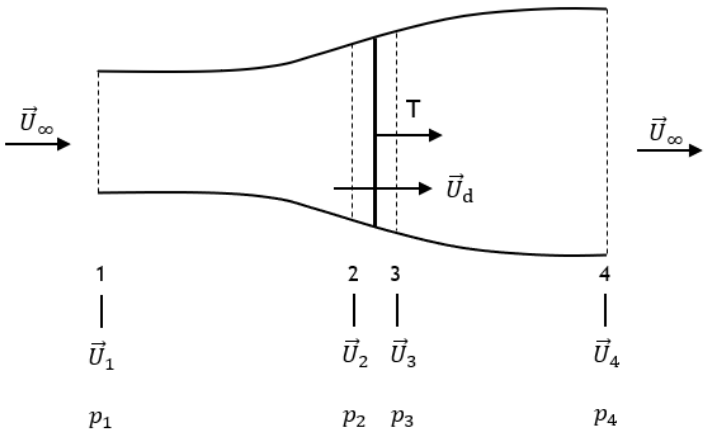

Figure 2.13: Flow through a wind turbine represented by a non-rotating disk.

By considering the balance of the axial momentum far upstream and far downstream, one obtains:

$$-\rho A_1 U_1^2 + T + \rho A_4 U_4^2 = 0 \quad (2.2)$$

where the letter A represents the area considered at the designated section. By using mass conservation through the disk:

$$(\rho A_1 U_1) = (\rho A_4 U_4) = (\rho A_d U_d) \quad (2.3)$$

and being A_d and U_d the area and wind velocity at the disk correspondingly, thrust from Equation 2.2 becomes:

$$T = \rho A_d U_d (U_1 - U_4) \quad (2.4)$$

The kinetic energy of air reaching the rotor decreases, as the rotor extracts part of it, leading to a decrease of the wind velocity. Just before the rotor the static pressure increases and decreases right after the air passes through the rotor. Work is only done at the actuator disk and from the drop pressure at the disk section ($p_2 > p_3$), thrust can be expressed as:

$$T = A_d \Delta p \quad (2.5)$$

Bernoulli equation is not applicable between section 2 and 3 but it is valid to the flow from far upstream until just right before the rotor, and from after the rotor until far downstream the rotor, being:

$$p_1 + \frac{1}{2}\rho U_1^2 = p + \frac{1}{2}U_2^2 \quad (2.6)$$

$$(p - \Delta p) + \frac{1}{2}\rho U_3^2 = p_4 + \frac{1}{2}U_4^2 \quad (2.7)$$

It is assumed $U_2 = U_3 = U_d$ and that $p_1 = p_4 = p_\infty$. If p is the pressure slightly upstream of the rotor disk, then the pressure after the rotor becomes $p - \Delta p$. Re-arranging Equations 2.6 and 2.7:

$$\Delta p = \frac{1}{2}\rho (U_1^2 - U_4^2) \quad (2.8)$$

Applying Equation 2.8 in Equation 2.5, the thrust force is:

$$T = \frac{1}{2}\rho A_d (U_1^2 - U_4^2) \quad (2.9)$$

Equating Equations 2.4 and 2.9, one obtains:

$$U_d = \frac{(U_1 + U_4)}{2} \quad (2.10)$$

Meaning that the velocity at the disk is the average of the far upstream and downstream velocities, or in other words, the average of the free stream and far-wake velocities. Therefore, the total velocity change from far upstream to far downstream is twice the change from far up stream to the disk [29]. If

$$U_1 - U_d = aU_1 \ (2.11)$$

then

$$U_1 - U_4 = 2aU_1 \ (2.12)$$

The term a is the axial induction factor and it represents the influence of the turbine in the wind. If Equations 2.10 and 2.11 are combined and re-arranged:

$$a = 1 - \frac{U_1 + U_4}{2U_1} \ (2.13)$$

Re-arranging Equation 2.11:

$$U_d = U_1(1 - a) \ (2.14)$$

Because the minimum velocity at the wake is zero, the maximum axial induction factor is 0.5. From the first law of thermodynamics, the power extracted by rotor is [30]:

$$P = \frac{1}{2}\rho A_d(U_1^2 - U_4^2)U_d = \frac{1}{2}\rho A_d U_d(U_1 + U_4)(U_1 - U_4) \ (2.15)$$

By combining Equations 2.10, 2.12 and 2.14 the power extracted from the rotor yields:

$$P = \frac{1}{2}\rho A_d U_1^3 4a(1 - a)^2 \ (2.16)$$

The kinetic energy of air is given by:

$$E_k = \frac{1}{2}m_{air}U_\infty^2 \ (2.17)$$

The flow that passes by the rotor holds a certain mass in a designated volume of air, from which energy is extracted from. The maximum rate at which the wind could supply energy to the wind turbine depends on the amount of mass that passes through the rotor per second, therefore:

$$\dot{E}_k = \frac{1}{2}\dot{m}_{air}U_\infty^2 \ (2.18)$$

where:

$$\dot{m}_{air} = \rho A_d U_\infty \quad (2.19)$$

The power available in the free stream wind of a stream tube is (the free stream wind velocity is equal to the wind velocity at section 1):

$$P_{avai} = \frac{1}{2}\rho A_d U_\infty^3 \quad (2.20)$$

Defining the power coefficient as a ratio of the power extracted by the rotor and the power available in the wind:

$$C_p = \frac{P}{P_{avai}} = 4a(1-a)^2 \quad (2.21)$$

By applying the first derivative to Equation 2.21, it is possible to find the axial induction factor value for the maximum power coefficient. In the same way the power coefficient was presented, the thrust coefficient is the ratio between the thrust force and the dynamic pressure actuating in the rotor disk area:

$$C_T = \frac{T}{\frac{1}{2}\rho A_d U_\infty^2} = 4a(1-a) \quad (2.22)$$

where the thrust force is given by combining Equations 2.10, 2.12 and 2.14 into Equation 2.9:

$$T = \frac{1}{2}\rho A_d U_\infty^2 4a(1-a) \quad (2.23)$$

Maximum power coefficient and maximum thrust coefficient occurs when:

$$\frac{dC_p}{da} = 0 \quad (2.24)$$

$$\frac{dC_T}{da} = 0 \quad (2.25)$$

Re-arranging Equations 2.12 allows to obtain the ratio between the far down stream wind velocity and the upstream wind velocity as a function of the axial induction factor:

$$\frac{U_4}{U_1} = 1 - 2a \quad (2.26)$$

The maximum power coefficient occurs when $a = 1/3$ performing a $C_p = 0.593$, and this value is known as the Betz limit, whose interpretation is that only up to 59% of the power available in the wind can be converted to mechanical power. For this maximum output, the wind velocity reaching the disk is $2/3$ of the free stream wind velocity, and the far downstream velocity is $1/3$ of the free stream velocity. The value for maximum $C_T = 1$ happens when $a = 1/2$. At the maximum power coefficient condition, the value of the thrust coefficient is 0.888. Figure 2.14 helps to visualize the conditions of maximum power and thrust coefficient. Equation 2.26 that represents the ratio between the wake velocity and the undisturbed free stream velocity is portrayed as the dash dot line where it is seen that when $a = 0.5$ the velocity ratio is zero, meaning that the wake velocity is zero.

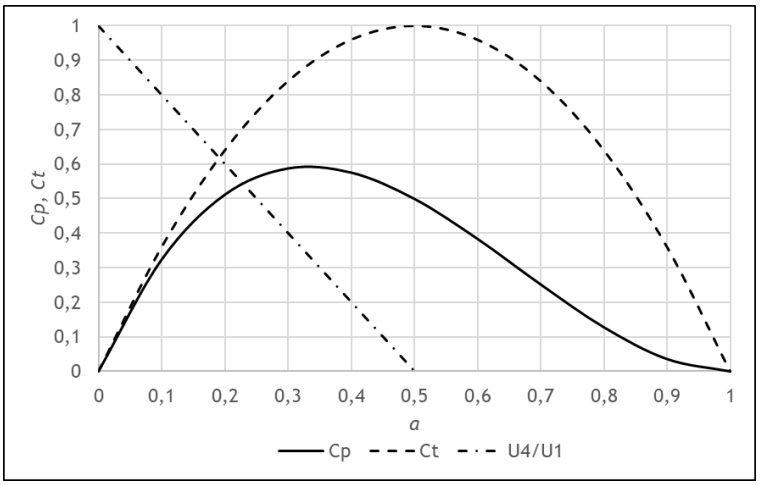

Figure 2.14: Power coefficient, thrust coefficient and the velocity ratio between the wake and the free stream as a function of the axial induction factor.

2.4.2 Momentum Theory with Wake Rotation

The previous analysis assumed no wake rotation, but in practical cases the rotating disk imposes a rotation motion to the flow passing through it. The angular momentum generated from the rotor, related to torque, makes that the flow behind the rotor rotates in the opposite direction of the rotor. The kinetic energy in the rotational motion means that less energy is extracted. The energy accounted for the wake rotation reduces the power coefficient as it is dependent from the rotational and translational kinetic energy instead of only translational kinetic energy presented in the previous theory. The kinetic energy present in the wake is proportionally related to the torque from the rotor. In 1935, Glauert [29] developed an approach to account for these losses, a model where the actuator disk is rotating, based on an annular stream tube with a certain radius, thickness and area (Figures 2.15 and 2.16). Across the rotating actuator disk, the angular velocity of the fluid flow relative to the disk, increases from Ω to $\Omega + \omega$,where Ω is the rotor angular velocity and ω the angular velocity imposed to the flow stream.

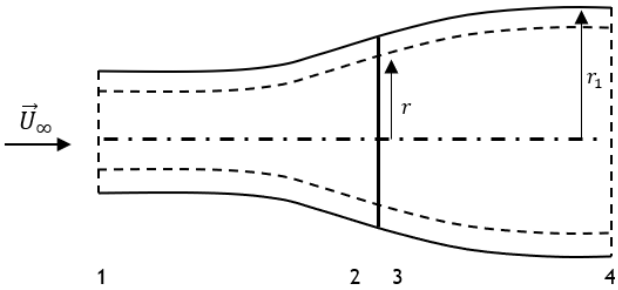

Figure 2.15: Annular stream tube model.

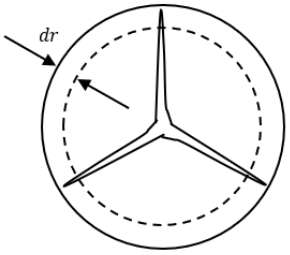

Figure 2.16: Annular stream tube geometry at the rotor plane.

First, a dimensionless parameter that define the one-dimensional momentum theory with wake rotation is presented as the angular induction factor:

$$a' = \frac{\omega}{2\Omega} \quad (2.27)$$

Following the previous analysis logic, the incremental thrust produced by the rotor is equal to pressure difference times the rotor area:

$$dT = \Delta p_{a'} dA = \Delta p_{a'} 2\pi r dr \quad (2.28)$$

The pressure difference between the rotor with only the effect of the wake rotation is given by:

$$\Delta p_{a'} = \rho\left(\Omega + \frac{1}{2}\omega\right)\omega r^2 \quad (2.29)$$

$$\Delta p_{a'} = 2\rho\Omega^2 r^2 a'(1 + a') \quad (2.30)$$

So, the incremental thrust is:

$$dT = 4\pi\rho\Omega^2(1 + a')a' r^3 dr \quad (2.31)$$

The thrust force from the non-wake rotation analysis applied for an annular cross section is:

$$dT = \frac{1}{2}\rho 2\pi r U_\infty^2 4a(1 - a)dr \quad (2.32)$$

Equating both the thrust forces equations, a relation between the two induction factors is obtained:

$$\frac{a(1 - a)}{a'(1 + a')} = \lambda_r^2 \quad (2.33)$$

where λ_r is the local tip speed ratio. The tip speed ratio compares the velocity of the tip of the blade to the free stream velocity by:

$$\lambda = \frac{\Omega R}{U_\infty} \quad (2.34)$$

The local tip speed ratio is a fraction of the tip speed ratio based on the local blade position:

$$\lambda_r = \lambda \frac{r}{R} = \frac{\Omega r}{U_\infty} \quad (2.35)$$

Applying the conservation of angular momentum that states that rotor torque equals the change in the wake angular momentum, the torque for a giving annular element is given by:

$$dQ = (d\dot{m} r^2)\omega \quad (2.36)$$

where

$$d\dot{m} = \rho U_d dA = \rho U_d 2\pi r dr \quad (2.37)$$

and the term in brackets represents the mass moment of inertia going through the giving annular element. Knowing the velocity at the disk by Equation 2.14 and the formula of the angular rotational factor, the torque for a giving annular element is:

$$dQ = 4\rho U_1 (1-a) a' \Omega \pi r^3 dr \quad (2.38)$$

The power extracted from the streamtube is:

$$dP = \Omega dQ = 4\rho U_1 (1-a) a' \Omega^2 \pi r^3 dr \quad (2.39)$$

With the definition of the local tip speed ratio, the incremental power coefficient is given by:

$$dC_p = \frac{dP}{\frac{1}{2}\rho A_d U_\infty^3} = \frac{dP}{\frac{1}{2}\rho \pi R^2 U_\infty^3} = \frac{8a'(1-a)\lambda_r^3 d\lambda_r}{\lambda^2} \quad (2.40)$$

Thus, integrating the power coefficient given by Equation 2.40 from 0 to the tip speed ratio, one gets:

$$C_p = \frac{8}{\lambda^2} \int_{\lambda_r=0}^{\lambda} a'(1-a)\lambda_r^3 d\lambda_r \quad (2.41)$$

In order to integrate Equation 2.41, a, a' and λ_r need to be related. Equation 2.33 performs a relation between these variables, but another equation is needed. By looking at Equation 2.41,

maximum power coefficient occurs when the factor $a'(1-a)$ gets a maximum for λ_r. Maximizing function $f(a,a') = a'(1-a)$ yields the second relation between a a':

$$a' = \frac{(3a-1)}{(1-4a)} \quad (2.42)$$

Replacing a' in Equation 2.33 by Equation 2.42, one gets the axial induction factor as function of the local tip speed ratio:

$$\lambda_r^2 = \frac{(1-a)(4a-1)^2}{(1-3a)} \quad (2.43)$$

For obtaining maximum power coefficient, Equation 2.43 must be derived in order to the axial induction factor. With this derivative, plus Equations 2.42 and 2.43, substituting in the power coefficient Equation (2.41) gives:

$$C_{p,max} = \frac{24}{\lambda_2}\int_{a_1}^{a_2}\left[\frac{(1-a)(1-2a)(1-4a)}{(1-3a)}\right]^2 da \quad (2.44)$$

The lower bound of the integral assumes the value of the axial induction factor from Equation 2.43 when the local tip speed ratio is zero (at the root), and when at the tip, the local tip speed ratio equals the tip speed ratio and the axial induction factor calculated is the one to be used for the upper bound of the integral.

For a fixed λ, the local tip speed ratio, λ_r, is maximum at the tip of the blade, decreasing as going inboard towards the root. According to the One-dimensional Momentum Theory, the angular velocity imposed to the fluid,ω must be added, where at the inner sections of the blade, ω is greater than Ω, thus leading to a greater effect of the rotation motion on the fluid stream. Figure 2.17 represents the behaviour of the axial and angular induction factor along

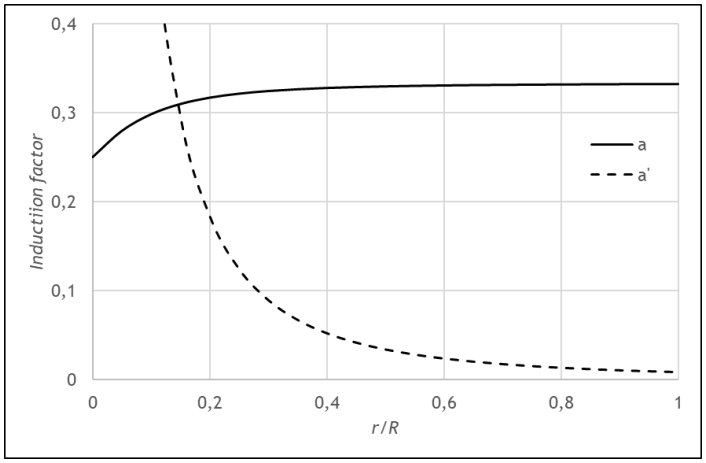

Figure 2.17: Axial and angular induction factors as a function of the non-dimensional blade (λ =5).

the non-dimensional blade, calculated for λ = 5. The axial induction factor, represented by the solid line, reaches its optimum value of 1/3 towards the tip of the blade while the rotational induction factor goes to zero, meaning that at the tip the effects due to the rotational motion are zero and the Betz limit is approached. In terms of the maximum power coefficient that is achieved at the tip of the blade, Figure 2.18 illustrates that for low tip speed ratios, the maximum power coefficient is low due to the effects of the rotational kinetic energy in the wake, and for an infinitely high tip speed ratio the maximum power coefficient reaches the value from the one dimensional theory due to the small effect of wake rotation.

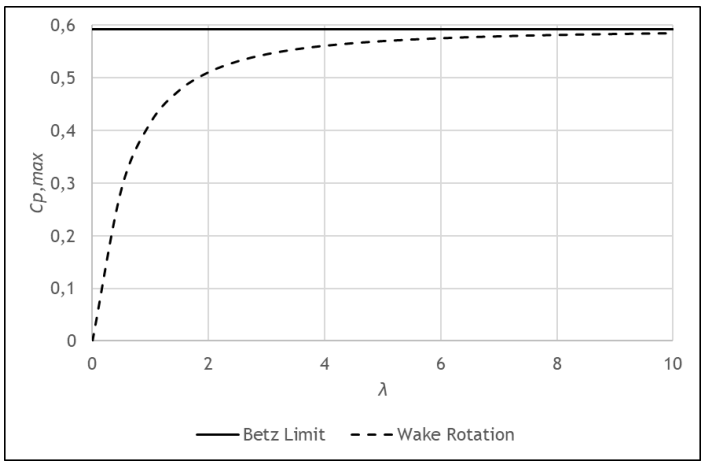

Figure 2.18: Maximum power coefficient obtained with wake rotation as a function of λ.

2.4.3 Airfoil Terminology

The action of the relative wind drives the blades of a wind turbine by creating aerodynamic forces, whether lift-like or drag-like forces. Wind turbines can be powered by lift or drag devices, but simple power coefficient analysis for both yields that lift driven machines are more efficient than drag driven ones. Lift devices produce 50 times the power per unit of projected area than drag devices [29]. The maximum power coefficient of a rotary machine using drag is less than $\frac{4}{27} C_{D,max}$ according to the projected area of the drag elements.

The generation of circulation creates lift that does not imply viscous losses in the flow, while drag forces operate through flow separation on the blade. An airfoil is a specific shape to form a structure that produces mechanical forces due to the motion of the airfoil subjected to a fluid, being important in the performance of any wind energy conversion system as its blades use airfoils to maximize the lift per unit drag. Visible in Figure 2.19 several parameters are used to describe an airfoil such as: chord, mean camber line, thickness, leading edge, trailing edge, upper and lower surface and angle of attack. The angle between the relative wind and the chord line is defined as the angle of attack, α. The chord line is the line connecting the leading and trailing edge and the chord is the length of the chord line. The camber line is the mean line between the upper and lower surface while the camber is the distance from the

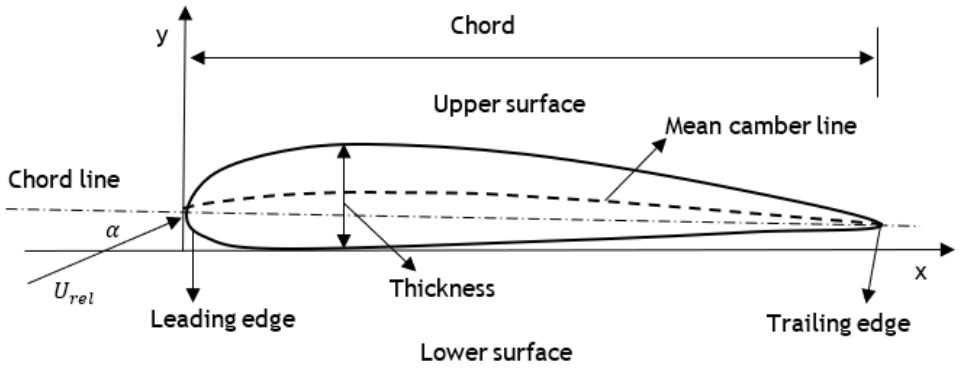

Figure 2.19: Airfoil geometry parameters.

camber line and the chord line measured perpendicularly to the later. Thickness is the distance from the upper and lower surface measured perpendicularly to the chordline. The aerodynamic performance of an airfoil is affected by geometric paraments such as: the leading edge radius, mean camber line, maximum thickness, thickness distribution of the profile, and the trailing edge angle [30].

The lift force, defined to be normal to the incident flow, is the result of the uneven pressure between the upper and lower airfoil surface and shear stress due to friction. The drag force, as stated previously, is the result of the viscous friction forces at the surface of the airfoil and from the unequal pressure on the upstream facing and downstream facing airfoil surfaces. One non-dimensional parameter to define the fluid flow conditions is the Reynolds number, that is the ratio between orders of magnitude of inertial forces and viscous forces. The Reynolds number is given by:

$$Re = \frac{Uc}{v} = \frac{\rho U c}{\mu} \quad (2.45)$$

where v is the kinematic viscosity, U the relative velocity, c the chord length, ρ the fluid density and μ the dynamic viscosity. Another non-dimensional parameter important to the airfoil behaviour is to normalize lift and drag forces by dividing the force per unit span by the dynamic pressure and the chord length, therefore obtaining lift and drag coefficients:

$$C_L = \frac{L}{\frac{1}{2}\rho_\infty U_{rel}^2 c} \quad (2.46)$$

$$C_D = \frac{D}{\frac{1}{2}\rho_\infty U_{rel}^2 c} \quad (2.47)$$

where ρ_∞ and U_{rel} are free stream density and relative velocity correspondingly.

Usually, HAWT airfoils are designed to be used at low angles of attack, where lift coefficients are high and drag coefficients are relatively low. The airfoil also behaves differently according to the Reynolds number, as it decreases, viscous forces increase in magnitude compared to inertial forces, leading to an increase in surface friction, that affect velocity, the pressure gradient and the lift generated per unit drag.

2.4.4 Blade Element Theory

Originated by Froude and later developed by Drzewiecki [30], this theory refers to an analysis of forces produced at a section of the blade as a result of the motion of the fluid. In Blade Element Theory, the blade is divided into N sections (Figure 2.20), and each blade section acts as a two-dimensional lifting surface as well as it is subjected to a relative wind due to the air flow and rotation of the disk. No interactions between the blade elements are assumed and the forces on the blade elements are only determined by the blade's airfoil lift and drag coefficients. The Momentum Theory described in Subchapter 2.4.1 provides the induced flow needed to calculate the air flow at the rotor disk.

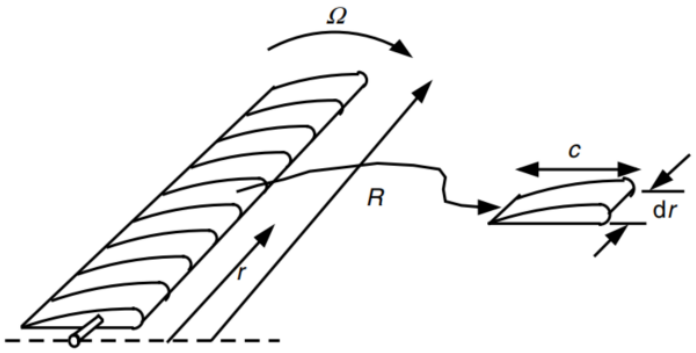

Figure 2.20: Blade Element schematic model [30].

Each element experiences a different flow as they have different rotational speed, different chord length and different twist angle. The blade section does not experience the free stream wind velocity in its total magnitude as it suffers the reduction from the axial induction factor,

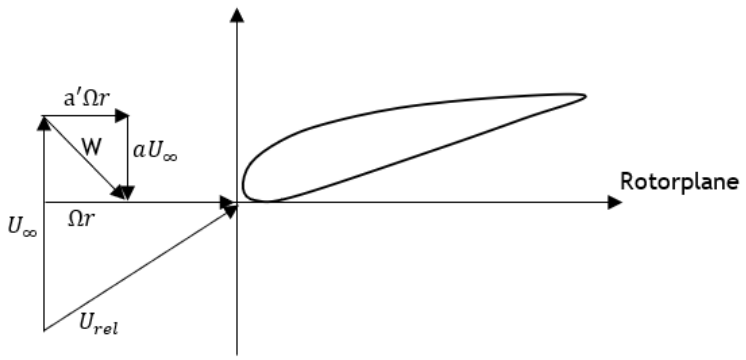

Figure 2.21: Velocity triangle model of the flow incident at a section of the blade.

giving the induced velocity vector, aU_∞. The rotational velocity is the sum of the blade section velocity with the induced angular velocity, $a'\Omega r$, that results from the angular induction factor. Figure 2.21 portraits the schematic velocity vectors at a section of the blade.

Analysing Figure 2.22, the relative wind velocity is given by:

$$U_{rel}^2 = [U_\infty(1-a)]^2 + [\Omega r(1+a')]^2 \quad (2.48)$$

and, it is deduced the angle between the relative wind and the plane of rotation ϕ, as well as the relative velocity in terms of the cosine and sine of ϕ:

$$tan\phi = \frac{U_\infty(1-a)}{\Omega r(1+a')} = \frac{(1-a)}{(1+a')\lambda_r} \quad (2.49)$$

$$U_{rel} = \frac{U_\infty(1-a)}{\sin\phi} \quad (2.50)$$

$$U_{rel} = \frac{\Omega r(1+a')}{\cos\phi} \quad (2.51)$$

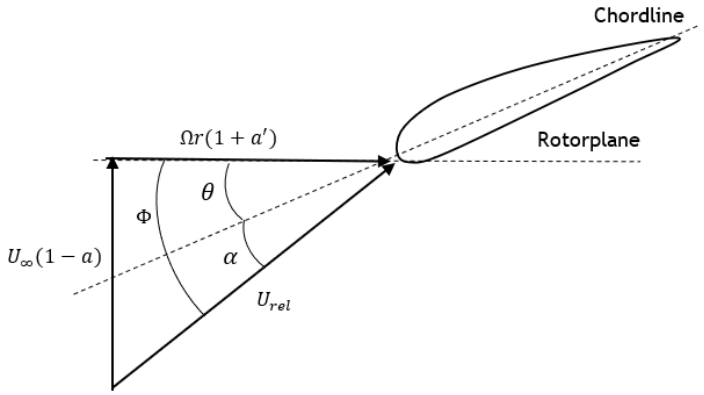

Figure 2.22: Blade forces analysis.

The sum of the angle of attack α, and the angle between the chordline and the rotational velocity, θ, known as the pitch angle, gives ϕ that is the angle of relative wind. Knowing the equation of the relative wind velocity, it is possible by analysing Figure 2.23 to calculate the forces that act on the plane of the rotation of the blade.

The lift and drag force per unit blade span for each element is given by:

$$L = \frac{1}{2}\rho c C_L U_{rel}^2 \quad (2.52)$$

$$D = \frac{1}{2}\rho c C_D U_{rel}^2 \quad (2.53)$$

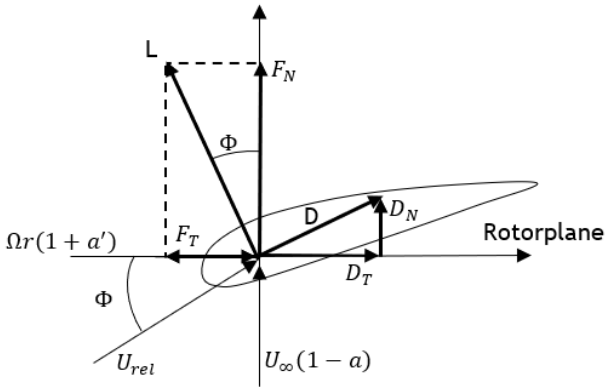

Figure 2.23: Local loads analysis.

The force normal to the plane of rotation is the one responsible for the thrust of the rotor and it is the sum of the vertical lift and drag component:

$$F_N = L\cos\phi + d\sin\phi \quad (2.54)$$

The tangential force is the sum of the lift and drag horizontal component and it is the responsible force for the motion of the rotor:

$$F_T = L\sin\phi - D\cos\phi \quad (2.55)$$

Being B the number of blades of the rotor, thrust is yielded as:

$$dF = BF_N dr = B\frac{1}{2}\rho c U_{rel}^2 (C_L\cos\phi + C_D\sin\phi)dr \quad (2.56)$$

The rotor torque produced is calculated by multiplying the tangential force times the radius of the section times the number of blades:

$$dQ = BF_T r dr = B\frac{1}{2}\rho c U_{rel}^2 r(C_L\sin\phi - C_D\cos\phi)dr \quad (2.57)$$

The rotor power is given by multiplying the rotor angular velocity by the torque produced:

$$dP = \Omega dQ = \Omega B F_T r dr \quad (2.58)$$

Hence, from the Blade Element Theory, equations are obtained for the normal force (thrust), tangential force (torque) and power from the flow angles at the blade and the airfoil lift and drag characteristics.

2.4.5 Blade Element Momentum Theory

The concept of free vortices being shed from the blades, defining a slipstream and generating induced velocities has led to the development of modern propeller theory, which work is attributed to Lanchester and Flamm for the original concept; to Joukowski for the induced velocity analysis; to Betz for optimization; to Prandtl and Goldstein for circulation distribution; and Glauert, Pistolesti and Kawada for general improvements [20].

Wind turbine blades operate within a complex environment, and the interaction between the production of power, the boundary layers around the airfoils and the flow field around the turbine rotor, forced the need to use computer codes for blade design and performance analysis. Some or all, of the following characteristics are calculated by these computer codes: overall steady state rotor performance; fluctuating aerodynamic loads along the blade; the flow field around the wind turbine; and noise emissions generated by aerodynamic effects. Aeroelastic codes (referred to the ones that perform fluctuating aerodynamic loads along the blade) calculate not only the rotor aerodynamics but also the interaction between the blade motions, due to its elastically deforming, and the flow. The aeroelastic codes used for rotor behaviour by the industry and the scientific community, are based on the Blade Element Momentum Theory that describes the rotor steady state behaviour. Using both the Momentum Theory with Wake Rotation and the Blade Element Theory, one can model the ability of a wind turbine to extract power with the blade shape. Also known as Strip Theory, it assumes a local 2-D local flow at each radial station, and it is used to determine the rotor performance (if the blade shape has been selected) or the rotor shape (if the blade shape is yet known) [30].

As said in Subchapter 2.4.4, the blade is divided in a finite number of elements, where two sections form an element that will sweep the rotor plane on a circular path. If using the BEM Theory for performance analysis, the radial position, profile, chord, twist and length of the blade sections are required. The Momentum Theory with Wake Rotation (Subchapter 2.4.2) provides the relative wind speed for every section that will allow to calculate the angle of attack and thus, the lift and drag coefficients from the Blade Element Theory. Having these coefficients, the normal and tangential force components, the thrust and torque of an element is computed and added to provide the final thrust and torque of the rotor [31].

In Subchapter 2.4.1, describing the performance of the ideal wind turbine, meaning with no wake rotation, it was seen that the maximum C_p would occur for $a = 1/3$. If applying the same assumptions to the equations of the One-dimensional Momentum Theory and the Blade Element Theory, one can reach simple equations to determine the shape of an ideal rotor. Known as the Betz optimum rotor, it provides the maximum power for a chosen design λ. For this blade shape analysis, the following is assumed:

- No wake rotation, $a' = 0$;
- No drag, $C_D = 0$;
- No losses because of a finite number of blades;
- In each annular stream tube, $a = 1/3$.

Equating the thrust equation from the One-dimensional Momentum Theory for no wake rotation for an annular stream tube, to the thrust equation from the Blade Element Theory, an equation is reached that allows to calculate the chord distribution of the blade for the Betz optimum rotor:

$$\frac{a}{1-a} = \frac{BcC_L \cos\phi}{8\pi r (\sin\phi)^2} \quad (2.59)$$

From the Blade Element Theory, the equation of the angle of the relative wind is already known, and with the value of the axial induction factor of $1/3$, Equation 2.59 turns in:

$$\frac{8\pi r \sin\phi}{3BC_L\lambda_r} = c \quad (2.60)$$

The angle of the relative wind within these assumptions is given by:

$$\phi = \tan^{-1}\left(\frac{2}{3\lambda_r}\right) \quad (2.61)$$

By analysing Equation 2.59, it is seen that a design λ, the number of blades, the radius of the rotor, and the lift and drag coefficients of an airfoil as function of the angle of the attack must be defined. The chosen angle of attack must be one where the lift to drag ratio is the minimum possible in order to comply with the assumption of no drag. Assuming a rotor radius of 1.5 m, 3

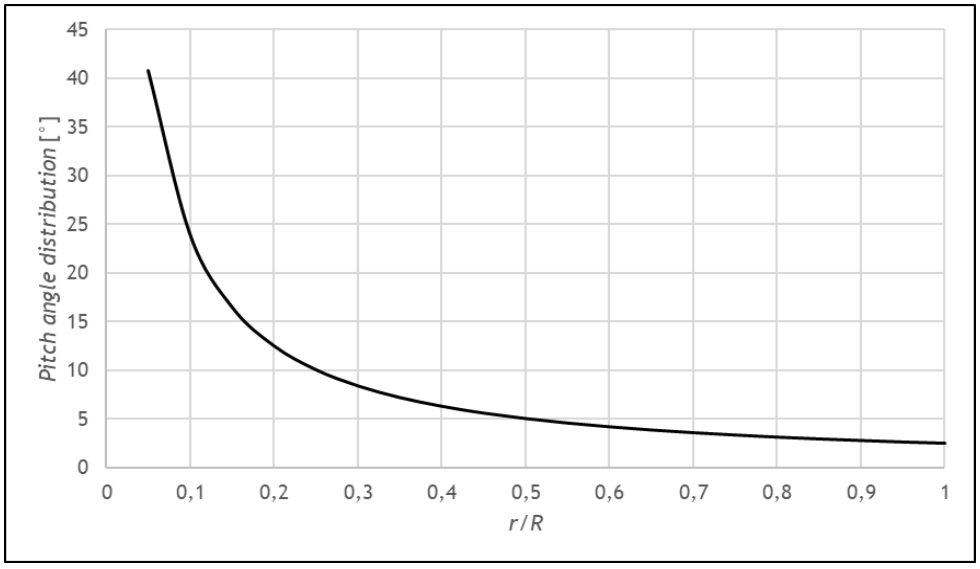

Figure 2.24: Blade pitch angle distribution.

blades, a design $\lambda = 5$, and a hypothetic airfoil with a lift coefficient of 1 and an angle of attack of $7°$ corresponding to the minimum L/D, the chord, relative wind and pitch angle are possible to compute. Figure 2.24 and 2.25 represent the calculated values of the pitch angle and chord distribution respectively, for the chosen parameters, where it is seen that the chord decreases from the root to the tip of the blade. The same behaviour is noted for the pitch angle distribution of the blade. The calculated ideal blade shape would function well for the tip speed ratio considered, but an ideal rotor is hard to design, as the rotor will operate in a wide range of tip speed ratios, meaning that no longer would be an optimum rotor. Although this presents difficulties for the design and fabrication of the blade, it provides valuable insight for the overall design and performance analysis.

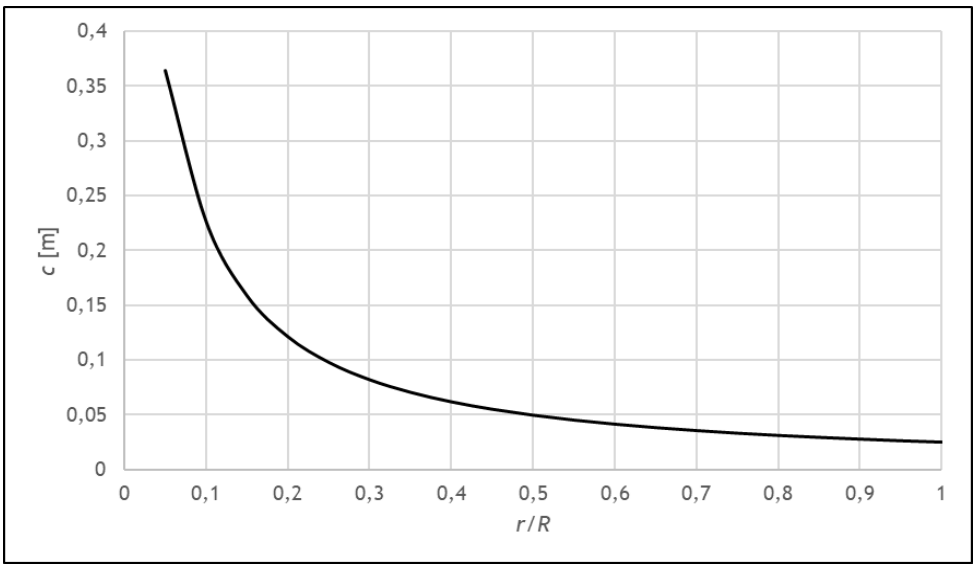

Figure 2.25: Blade chord distribution.

Using the BEM Theory for non-optimum blades, the approach must be an iterative one, meaning that one should try one blade shape and predict its performance until a suitable blade is chosen. For this performance analysis, including wake rotation, it is assumed that the blade shape is chosen and the airfoil characteristics are already known, such as the chord and pitch angle distribution. Normalizing the equations of the normal (2.54) and tangential (2.55) forces from the Blade Element Theory, with respect to $\frac{1}{2}\rho c U_{rel}^2$ gives:

$$C_N = C_L \cos\phi + C_D \sin\phi \quad (2.62)$$

$$C_T = C_L \sin\phi + C_D \cos\phi \quad (2.63)$$

where:

$$C_N = \frac{F_N}{\frac{1}{2}\rho c U_{rel}^2} \quad (2.64)$$

$$C_T = \frac{F_T}{\frac{1}{2}\rho c U_{rel}^2} \quad (2.65)$$

Using Equation 2.50 for the U_{rel} and Equation 2.64, the thrust provided by the Blade Element Theory becomes:

$$dT = B\frac{1}{2}\rho c C_N U_\infty^2 \frac{(1-a)^2}{(\sin\phi)^2} dr \quad (2.66)$$

In the same way, the torque calculated by the Blade Element Theory with the manipulation of Equation 2.50 and 2.51 for the U_{rel}, and Equation 2.65, yields:

$$dQ = B\frac{1}{2}\rho c F_T \frac{U_\infty(1-a)}{\sin\phi}\frac{\Omega r(1+a')}{\cos\phi} dr \quad (2.67)$$

Equating the two expressions regarding the rotor thrust, 2.32 and 2.66, it is obtained an expression for the the axial induction factor:

$$a = \left[\frac{4(\sin\phi)^2}{\sigma C_N} + 1\right]^{-1} \quad (2.68)$$

where σ, that is the solidity ratio represents the annular area that is covered in the blade, given by:

$$\sigma = \frac{Bc}{2\pi r} \quad (2.69)$$

If the torque equations from the One-dimensional Momentum Theory (2.48) and the Blade Element Theory (2.67) are equated, the angular induction factor is possible to express by:

$$a' = \left[\frac{4\sin\phi\cos\phi}{\sigma C_T} - 1\right]^{-1} \quad (2.70)$$

Having these equations deduced, the BEM Theory can be applied for each strip independently with the aid of the following steps [32]:

1. Assume a and a';
2. Calculate ϕ (equation 2.49);
3. Calculate α ($\alpha = \phi + \theta$);
4. Read values of the airfoil C_L and C_D according to α;
5. Compute C_N and C_T (equations 2.62 and 2.63);
6. Calculate a and a' with equations 2.68 and 2.70;
7. Compare to the previous assumed values. If within a certain tolerance, stop iteration.

With the known values of a for each annular cross section, it is possible to calculate the overall rotor performance by integrating the power coefficient. The power from each annular cross section is given by multiplying the differential torque with the angular velocity ($dP = \Omega dQ$). Thus, the overall rotor power is:

$$P = \int_{r_h}^{R} dP = \int_{r_h}^{R} \Omega dQ \quad (2.71)$$

where r_h is the blade radius at the hub of the blade. The power coefficient is then:

$$C_p = \frac{\int_{r_h}^{R} \Omega dQ}{\frac{1}{2}\rho\pi R^2 U_\infty^2} \quad (2.72)$$

Substituting the differential torque by the expression provided by the Blade Element Theory, applying the definition of the local λ, and other equations combining different parameters, the power coefficient yields [28]:

$$C_p = \frac{8}{\lambda^2}\int_{\lambda_h}^{\lambda} \lambda_r^3\, a'(1-a)\left[1 - \frac{C_L}{C_D}\cot\phi\right] d\lambda_r \quad (2.73)$$

where λ_h is the tip speed ratio at the hub section.

The previous analysis presents the basics of the BEM Theory but in order to be even more precise it is needed to apply corrections. One of those corrections addresses the losses due to the interaction of the shed vorticity with the blade flow near the tip. This circulation reduction at the tip of the blade is due to the pressure difference between one side of the blade and the

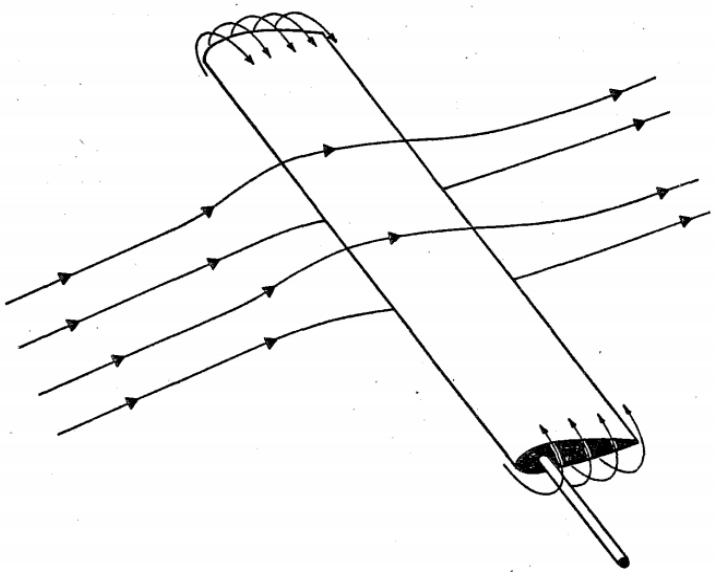

Figure 2.26: Tip and Hub Losses [28].

other. As the pressure is greater on one side of the blade, the flow at the tip of the blade will behave as shown in Figure 2.26. As the tip of the blade has a great contribution to the rotor torque and overall performance of the wind turbine, it is important to handle this torque reduction due to the circulation over the tip and root of the blade [28]. With fewer blades the tip losses become more significant.

One analysis to tackle this issue was done by Prandtl but it was performed for a slightly loaded propeller. Prandtl developed a method where the system vortex sheets created by the blades was substituted by parallel planes at a uniform spacing, in a way that the flow around the edges of the vortex sheets is approximated to the flow around the edges of the parallel planes system. Prandtl correction factor is given by:

$$F = \frac{2}{\pi}\cos^{-1}(e^{-f}) \quad (2.74)$$

where f is defined as:

$$f = \frac{B}{2}\frac{R-r}{r\sin\phi} \quad (2.75)$$

Thus, the equations of the thrust and torque must contain the tip loss correction factor. Equations 2.32 and 2.38 become:

$$dT = \frac{1}{2}\rho 2\pi r U_\infty^2 4a(1-a)Fdr \quad (2.76)$$

$$dQ = 4\rho U_1(1-a)a'\Omega\pi r^3 Fdr \quad (2.77)$$

With the Prandtl factor correction in the equations from the Momentum Theory with Wake Rotation, equating them to the equations from the Blade Element Theory, the axial and angular induction factors are:

$$a = \left[\frac{4F(\sin\phi)^2}{\sigma C_N} + 1\right]^{-1} \quad (2.78)$$

$$a' = \left[\frac{4\,\mathrm{F}\sin\phi\cos\phi}{\sigma C_T} - 1\right]^{-1} \quad (2.79)$$

Equations 2.78 and 2.79 are now the ones to be used in step 6, instead of Equations 2.68 and 2.70 in the algorithm described previously. There are also losses in the blade root section, and in the same way of the tip losses method, Prandtl's method is applied to account for the inner blade losses. The correction factor (F) follows the same as the one in Equation 2.74 but f is given by:

$$f = \frac{B}{2}\frac{R - r_{hub}}{r_{hub}\sin\phi} \quad (2.80)$$

where r_{hub} is the hub radius. Thus, the overall correction factor for the tip losses is:

$$F_{total} = F_{tip} * F_{hub} \quad (2.81)$$

A more rigorous analysis for the tip losses of a propeller was made by Goldstein [28], based as a function of the induced rotational velocity along the blade. With the right boundary layers, Laplace's equation was used to solve Goldstein tip loss correction factor. The correction factor is:

$$K = \frac{1 + {\lambda_r}^2}{{\lambda_r}^2}\frac{r\Omega}{\pi v_G \omega_G} \quad (2.82)$$

where v_G is the advance ratio and ω_G is the advance velocity of helical vortex surfaces. Figure 2.27 shows the circulation distribution for a two-bladed propeller using the Prandtl and Goldstein corrections factors. The Prandtl approximation is accurate for B greater than two for high values of λ. In the other hand, Goldstein method is useful for low tip speed ratios and for one or two bladed propellers.

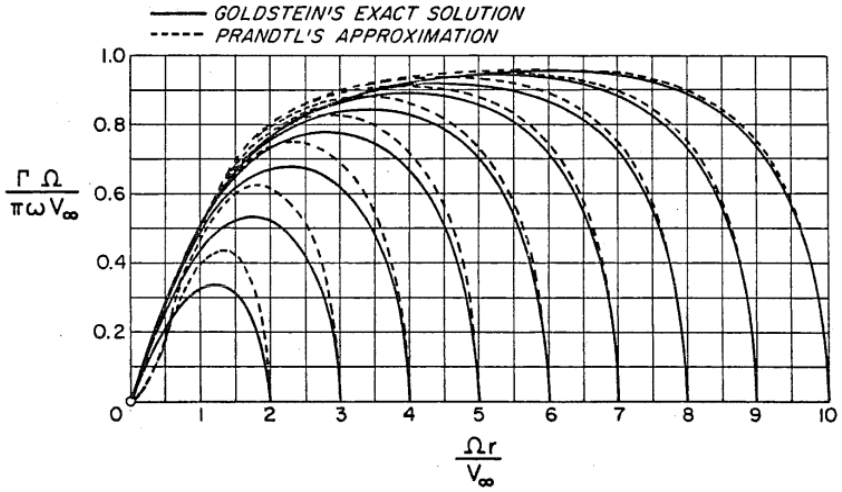

Figure 2.27: Circulation distribution along the blade [28].

2.5 State of the art

The small wind turbine that is studied in the present work belongs to the family of wind turbines designed by Hugh Piggott, an alternative energy enthusiast with background on electrical engineering. Hugh currently lives off-grid in the Scoraig peninsula in Scotland, where over the time he has been improving his designs and fabrication methods for a reliable and affordable wind turbine. Having worked in developing countries such as Zimbabwe, Sri Lanka and Peru sharing his knowledge, over the years he has written books explaining how he designs and builds

his wind energy conversion systems. With diameters from 1200 to 4200 mm, his turbines are designed to be economically viable, construction friendly (meaning that an unskilled person should be able to fabricate the wind turbine with hand tools), strong enough to survive extreme weather conditions and presenting good performance from 3 to 10 m/s winds [15].

Hugh's wind turbines consist of a three bladed fixed pitch rotor connected to an axial flux permanent magnet coreless generator, a tail vane to face the rotor to the wind and a furling mechanism to protect it against extreme wind speeds. Everything is assembled in a guyed tower that allows to be lowered for maintenance purposes. In his document entitled "How to build a WIND TURBINE", Hugh lays out the blueprints for the overall construction of the wind turbine. The support of the rotor/generator assembly uses an automobile wheel hub while the generator's magnets are attached to car brake disks. The blades and the tail vane are made from wood because of its low price, availability and it will last for several years.

TieOLLE is the organization that built the Piggott turbine studied in this work. Designed for a $\lambda = 5$ and submitted to experimental and computational tests, the rotor was analysed and compared by the work of João Monteiro, Miguel Silvestre, Hugh Piggott and Jorge André, whose results are shown in the article "Wind tunnel testing of a horizontal axis wind turbine rotor and comparison with simulations from two Blade Element Momentum codes". The goal was to simulate the rotor with QBlade and WT_Perf BEM codes and compare it to the results from the wind tunnel testing. The rotor, shown in Figure 2.28, was analysed in the wind tunnel of the Associação para o Desenvolvimento de Aerodinâmica Industrial at wind speeds of 3.0, 3.7, 4.4, 5.5, 7.2 and 7.7 m/s, with experimental errors of 1 %. In order to analyse it using the BEM codes, the rotor was digitalized at the Centro Tecnológico da Cerâmica e do Vidro in Coimbra,

Figure 2.28: Stand used to perform the rotor's calibration [15].

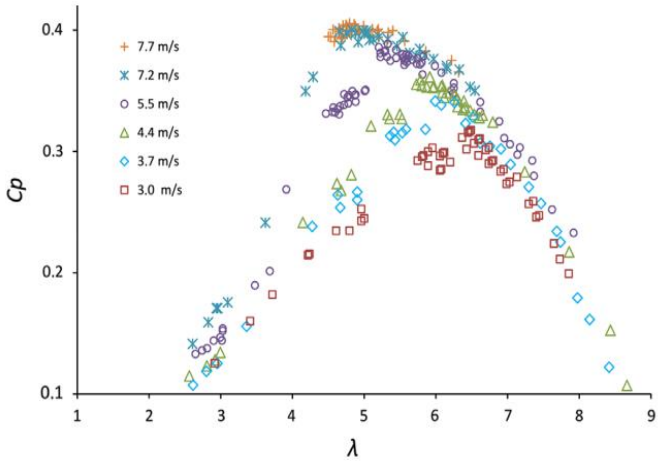

Figure 2.29: Experimental results [15].

with a 6 mm sphere diameter feeler for the individual shape of each blade, and a 2 mm feeler to obtain the setting angles and cords at each cross section required. The scans analysis found that blades 1 and 3 airfoils are similar in the outer regions, while only the two outer sections of blade 2 are similar with the other blades outer sections.

The experimental results are presented in Figure 2.29, where it is visible that the power coefficient increases with wind speed. The fall after the maximum power coefficient with the decrease of the λ is also visible due to the stall of the blades, but no data regarding the stall is presented for the 7.2 and 7.7 m/s as the rotor maximum rotational speed was set to 750 RPM. The results found a maximum C_p = 0.4 for a λ = 4.8 [15].

Being the blades geometrically different, the computational method performed a simulation of an ideal rotor for each individual blade and the rotor performance is the average of the three ideal rotors. The results seen in Figure 2.30 show similar outputs for the averaged rotor between both codes, where it is also seen the decrease of the power coefficient peak to higher values of λ with decreasing wind speed as in the experimental ones.

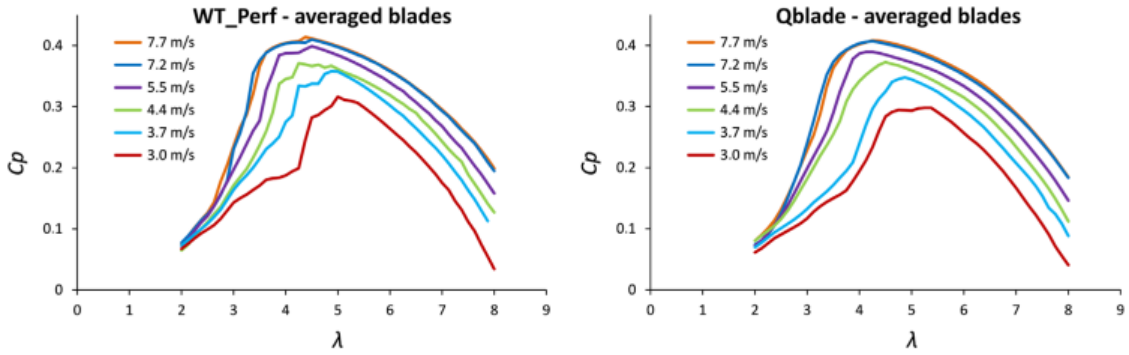

Figure 2.30: Average of blade 1, 2 and 3 BEM simulations of WT_Perf and QBlade codes [15].

A study that also conducted experimental and numerical investigation on a Hugh Piggott rotor was done by [33] at Delft University of Technology, that intended to design a rotor more practical to build (untwisted and untampered blades) and operate in Mali, where Hugh Piggott turbine designs already function. To do so, a 1.8 m diameter Hugh Piggott was tested at a closed wind tunnel circuit for wind speeds of: 4.17; 5.21; 6.27 and 8.23 m/s. The tests results show a maximum power coefficient ranging from 0.27 for 4.2 m/s windspeed to 0.33 for 8.3 m/s windspeed, around a λ = 5.3. The numerical simulation using an in-house BEM model, overpredicted the maximum power coefficient whose result was a C_p = 0.41. This difference was credited to the limited accuracy of the BEM model as well as of the inputs of the BEM model, as the BEM simulations used the NACA 4415 (at the blade root) and 4412 airfoils while the wind tunnel tests were carried with the actual geometry of the rotor. The experimental results also demonstrated the increase of the rotor performance with the increase of the wind speed as a result of higher Reynolds numbers.

Another study about small wind turbines that investigated numerically and experimentally a 900 mm diameter, 3 bladed, constant pitch rotor was done by [34]. The geometry of the model was made following an in-house BEM model for a design λ = 6 and with a National Renewable Energy Laboratory S826 airfoil that presents 14 % thickness and is designed for a $Re = 2\text{x}10^6$. The chord at the tip of the blade is 25.8 mm and the hub diameter is 0.09 m. The model was then machined in aluminium and tested in a 2.7 m wide, 2 m high and 12 m long wind tunnel for wind speeds of 7.2, 8.2, 9.3 and 10.3 m/s, that yielded a maximum C_p = 0.448 at λ = 6.The numerical method started with subjecting the 2D airfoil to the XFoil and Fluent software to see how well would they behave. The Fluent simulations used the turbulent $k-\omega$ shear stress transport and the $k-\epsilon$ re-normalization group turbulence model options. The critical amplification ratio (Ncrit) of the XFoil was of 0.01 so that it could imitate the conditions of the turbulence models. It was concluded that the $k-\omega$ shear stress transport model gave results close to the XFoil results and that the $k-\epsilon$ re-normalization group over-predicted the lift and drag coefficients. The 3D simulations were performed using the BEM method and the Fluent software with the shear stress transport model. The numerical results showed that the BEM method can predict the performance of a wind turbine as the general shape of the power and thrust coefficient curves overall matched the wind tunnel data. Nevertheless, the thrust coefficient presented lower than the data from the experimental results for most of the λ range. The BEM method over predicted the power coefficient for high values of λ but for the λ values below the design value the predictions agreed well.

Chapter 3

Methodology

In this chapter, the procedure for the improvement of the horizontal axis wind turbine presented in [15] is presented and discussed. The first section summarizes a part of the fabrication process of the wooden rotor focusing the blades carving. In the second subchapter, there is a brief description of QBlade software and its capabilities. The modification that focusses a small leading edge smoothing of the airfoil towards the lower surface is explained in Subchapter 3.3. Each blade of the wind turbine is characterized by 6 sections across its length, thus making a total of 36 different airfoils to be smoothed. With all airfoils modified, QBlade is then used to perform a BEM simulation for the Piggott and modified rotor and the way to set up these simulations is described in Subchapter 3.4. In order to handle the high amount of data resulting from Subchapter 3.3 and 3.4, Excel software is used to plot side by side the graphics regarding the Piggott and the modified rotor performance. This is an iterative process meaning, if after the simulations are done the modifications fail to be better than the originals, the entire process is repeated until a better (if possible) performance is achieved. The last subchapter explains how the Piggott and modified rotor power are calculated for different rotational speeds, as well how all the data was handled.

3.1 The 1200 mm Diameter Hugh Piggott Wind Turbine

The blade carving process, as said before, must be a task possible for an unskilled person to perform with hand or power tools. In the “How to build a WIND TURBINE”, the detailed process is described. Because of the availability, low price and workability, wood is the material chosen for the carving of the rotor blades. To ease the carving, the builders must follow an image of the Aquila airfoil (Figure 3.1) to guide them, as this airfoil has a relative flat bottom and it is suitable for small scale wind turbines [15].

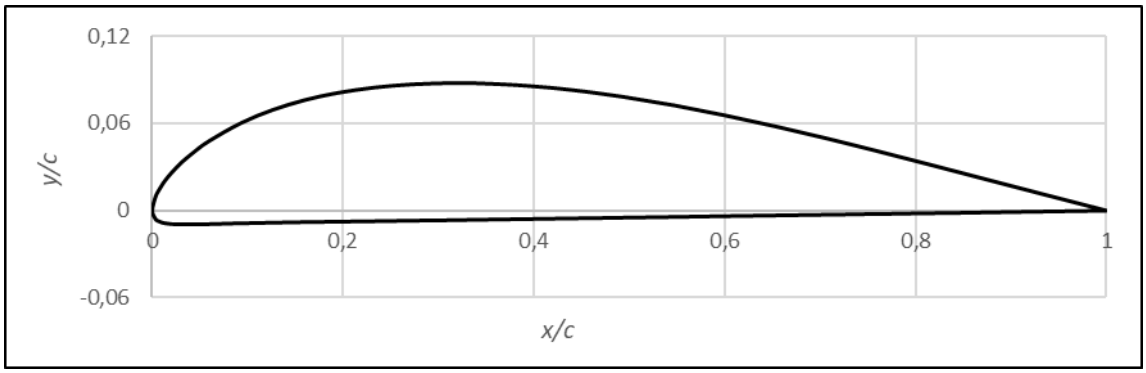

Figure 3.1: Aquila 9.3% smoothed airfoil from the UIUC Airfoil Coordinates Database.

The blade shape is determined by stations along the blade, each with a chord, blade angle and thickness. In this process, it is used width instead of chord and the “drop”, that is the distance from the face of the workpiece to the trailing edge (Figure 3.2).The blades are carved from workpieces (piece of wood) and the material must be light, straight grained and preferably well-seasoned and free of sap. A workpiece has the following dimensions: 1200 mm length, 150 mm width and 37 mm thick.

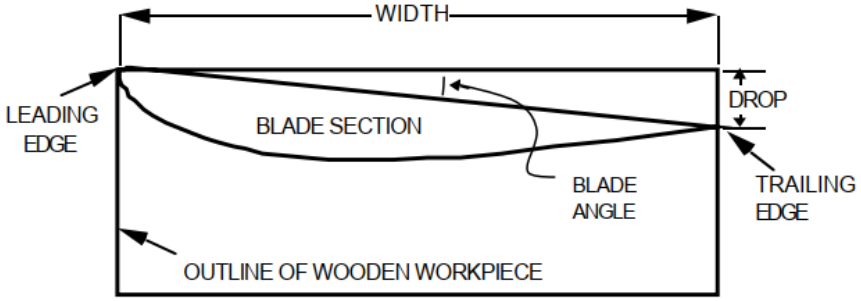

Figure 3.2: Airfoil scheme within the workpiece [35].

The first step is to create the tapered shape meaning, as said in the BEM Theory, the blade should be narrow at the tip whilst increasing its chord towards the root. From the root of the workpiece the stations are marked in all sides of the workpiece and then at each station, the desired width is marked from the leading and joined by a line crossing all marks (Figure 3.3). With the marks done, the extra material must be cut off with a bandsaw.

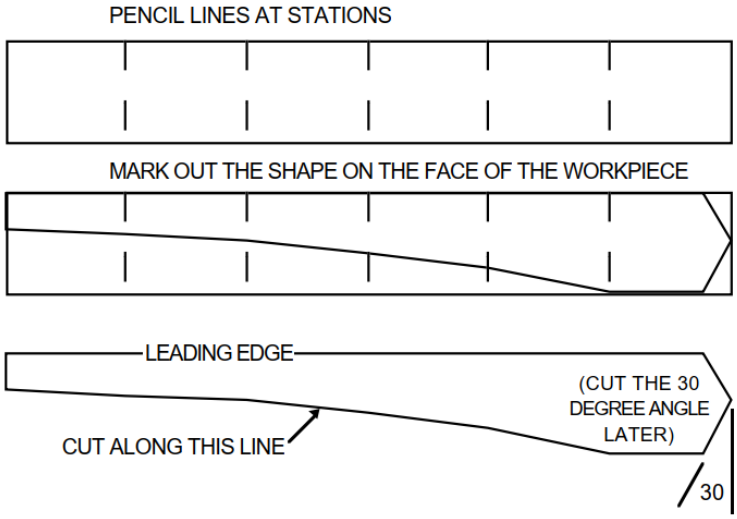

Figure 3.3: Tapered shape schematic view [35].

On the face that was cut, the stations must be draw again and in each station the drop is marked from the face of the wood and joined by a line, thus creating the line of the trailing edge. To finish step two the material above the line is removed (Figure 3.4) and when in doubt about the accuracy of the blade angle, a spirit level is used to check and fix any incorrections. In the third step the thickness of each station is marked from the windward face and joined by a line either in the trailing and leading edge (Figure 3.5). The lines help to carve the blade in

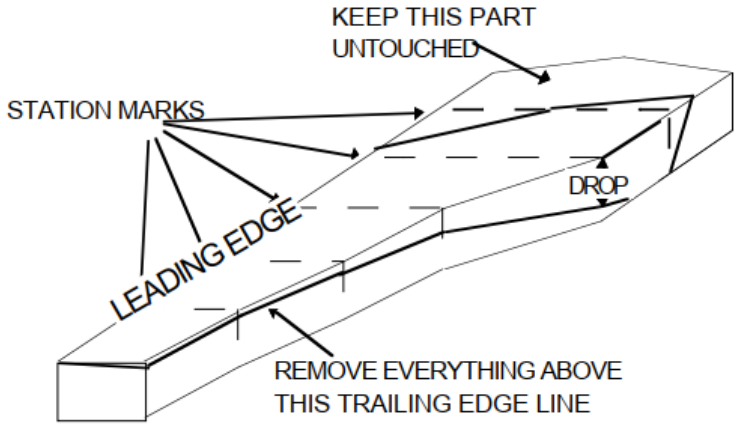

Figure 3.4: Schematic view of the twisted windward face [35].

order to obtain the correct thickness and when reaching the lines, the thickness must be checked with a calipper to make sure the right thickness is not crossed. In the end of this step both sides should be flat and parallel to each other and maximum thickness will be at 30 % of the distance between the leading and trailing edge.

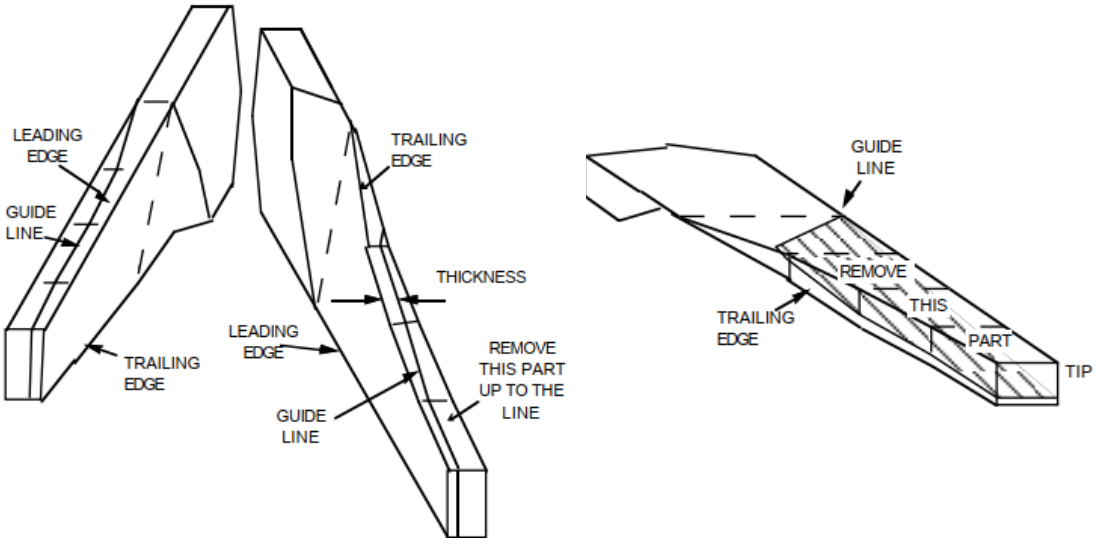

Figure 3.5: Workpiece marks to achieve the blade thickness [35].

The last step is to carve the blade sections with the shape of an airfoil. To do so another line is marked at 50 % of the distance between the leading and trailing edge that will guide in the carving of the trailing edge as seen in Figure 3.6. The trailing edge should be less than 1 mm thick. After the removal of the crossed area shown in Figure 3.6, the blade is finally carved to present a smooth curved shape like the Aquila airfoil. The geometric shape of an airfoil is of extreme importance due to the performance the rotor will present, thus this final step requires much care as there is no explanation on how to produce such curved shape. The trick is to remove any corners, but as one removes a corner, another one is produced. The builder should run his fingers through the wood to feel for any bump while bearing in mind: not to remove too

much wood; not to carve over the 30 % line and not to produce a corner at the maximum thickness point. Creating such curved shapes might seem easy while seeing the airfoil as a cross section but when carving over a blade with 1200 mm length the task gets more complicated, originating sometimes in less curved leading edges. These poor well-defined shapes will affect

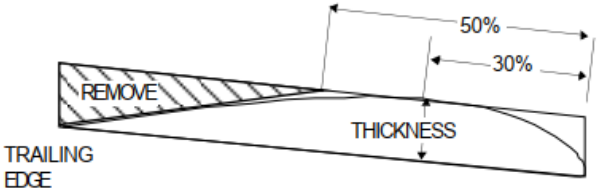

Figure 3.6: Cross section scheme on how to carve the curved shape [35].

the overall performance of the blade and consequently the rotor.

3.2 QBlade Software

3.2.1 Description

QBlade started as part of G. Pechlivanoglou PhD work, and it was initially developed by David Marten at the Department of Experimental Fluids Mechanics of Berlin Technical University. QBlade [36] is an open source calculation software, that uses Blade Element Momentum Method, Double Multiple Streamtube and nonlinear Lifting Line Theory Design and simulation software for vertical and horizontal wind turbines. It started from the need to create a single tool that would comprise all the functionalities needed for aerodynamic wind turbine design and simulation without the need to import, convert or process data from other sources (Figure 3.7). For horizontal axis wind turbines QBlade relies on the Blade Element Momentum Method while it uses the Double Multiple Streamtube method for vertical axis wind turbines computation. As almost all BEM codes available on the market are command line interfaced, it was desired to come up with a user-friendly graphic user interface capable of simulating airfoils as well as wind turbines. QBlade offers the following functionalities for BEM computations and blade design:

- Extrapolation of XFoil generated or imported polar data to 360º AoA;
- Blade design optimization, including 3D visualization;
- Turbine definition (rotor blade, turbine control, generator type, losses);
- BEM computation over range of tip speed ratios or windspeeds;
- Annual yield computation with Weibull distribution;
- Data browsing and visualization;
- Blade geometry export functionality;
- Storing of projects, rotors, turbines, airfoils and simulations in a runtime database;

- Computation of more than 30 relevant rotor variables, such as critical roughness.

The combination of a BEM code and XFoil allows for the user to rapidly design custom airfoils and compute their polars, extrapolate the polar data to a range of 360º AoA, and directly integrate them into a wind turbine rotor-simulation [36]. QBlade includes the following modules:

- Airfoil design and analysis;
- Lift and drag polar extrapolation;
- Blade design and optimization;
- Turbine definition and simulation.

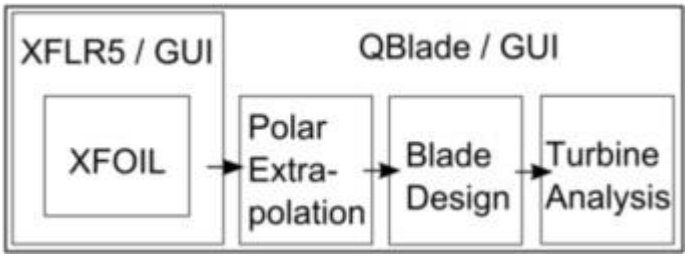

Figure 3.7: Software modules inside QBlade [36].

3.2.2 Airfoil Design and Analysis Module

XFLR5 is the software behind QBlade Airfoil design and analysis module. Created by Depperois in 2003, XFLR5 [36] is the result of translating XFoil software from FORTRAN to C++ with a friendly graphical user interface. According to the definition given by the official website of XFLR5 [37]: "XFLR5 is an analysis tool for airfoils, wings and planes operating at Low Reynolds Numbers. It includes: XFoil's Direct and Inverse analysis capabilities; Wing design and analysis capabilities based on the Lifting Line Theory, on the Vortex Lattice Method, and on a 3D Panel Method".

The airfoil design module of XFLR5 offers the option to design an airfoil either by a NACA airfoil generator or by some other options such as:

- B-splines;
- Splined Points;
- Modification of a foil's thickness and camber;
- Interpolation of airfoils;
- Inverse Methods.

The first option gives smoother surfaces; upper and lower surfaces are each determined by a separate and single B-Spline and the spline degree can go between 2 and 5. Second option has

greater control over the geometry, where the upper and lower surfaces are each determined by a set of control points. These are linked by 3rd degree B-Splines and the slope at each visible control points are determined by the line passing through the immediately previous and next control points. Any modification of a foil's thickess, camber, max thickness or max camber will generate a new airfoil. This option is used when comparing different profiles with similar shape because of the greater accuracy on the final design shape [37].

The airfoil analysis module allows to import airfoils and to compute the lift and drag coefficient data over different angles of attack. While it is necessary that airfoils file format be .dat, they must also follow the traditional format. The first line of the file must hold the foil's name, followed by the X and Y coordinates, starting in the trailing edge, move to the leading edge through the upper surface before going back to the trailing edge. An example of the data format for the airfoil coordinates is given in Appendix A. With the foils stored in the Direct Foil Design, a 'polar object' required to perform any analysis is possible to define. A polar object is defined by:

- Its Reynolds and Mach numbers;
- The laminar to turbulence transition criterion;
- The forced trip locations on top and bottom surfaces.

There are 3 different types of analysis to choose from QBlade XFoil Direct Analysis menu, being them: Define an Analysis; Batch Analysis and Multi-threaded Batch Analysis. The airfoils analysis are further explained but all were performed using the first type. The "Define an Analysis" allows to define Reynolds and Mach numbers, as well as the transition number and trip locations. By default, the transition number is set to 9, and the trip locations are set at the trailing edge. XFLR5 interface provides different graphics, at a maximum of 5 being displayed in the "XFoil's Direct Analysis" menu. Double clicking on a certain graphic will open the settings menu, where variables can be chosen for the X and Y axis, to adjust scales, grids, fonts or backgrounds, among others.

3.2.3 Lift and Drag polar extrapolation

In this module, polars previously created can be extrapolated to a 360º angle of attack (Figure 3.8). An airfoil polar is extrapolated due to the limited lift and drag coefficients of XFoil results at angles before and beyond stall. The algorithm does not converge for very high or low angles of attack, and for HAWT and VAWT operations, angles of attack high as 70º can occur [36]. To tackle this issue QBlade implements two different approaches of how to generate this extrapolation, such as the Viterna-Corrigan post stall model or the Montgomerie model.

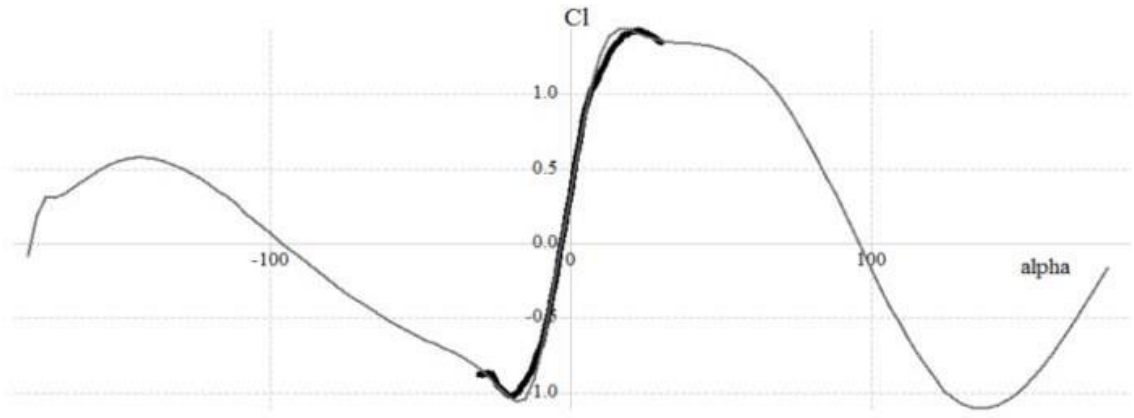

Figure 3.8: NACA-63 polar extrapolation to 360º [36].

3.2.4 Blade Design and Optimization

Inside this module, blades can be designed using existing airfoils and 360º polars. A rotor blade is defined by distributing airfoils over different sections of the blade, and: blade number, hub radius, single or multi polar, chord length, twist angle, edgewise or flapwise blade curvature, azimuthal angle and the twist axis of each individual foil. The last two parameters are inserted in the advanced blade design option.

3.2.5 Turbine Definition and Simulation

For these simulations, the wind turbine type must be defined, with parameters such as, for example: power regulation, rotational speed, cut in and cut out velocity or generator efficiency. After this setup is complete three different simulations types can be performed: a dimensionless simulation is useful to compare different rotor geometries and yields only dimensionless results over a number of λ; a turbine simulation yields the annual energy production for a given Weibull wind speed distribution over a range of wind speeds; over a set of rotational speeds, blade pitch angles and wind speeds, the multi-parameter simulation results in the turbine full operational characteristics.

3.3 Existing Wind Turbine Airfoil Modification

The modification operation in according to the last section, used the following QBlade features:

- Data import of the Piggott airfoil file;
- Use of B-Splines to replicate the Piggott airfoil;
- Spline modification to smooth the leading edge towards the airfoil lower surface;
- Direct analysis.

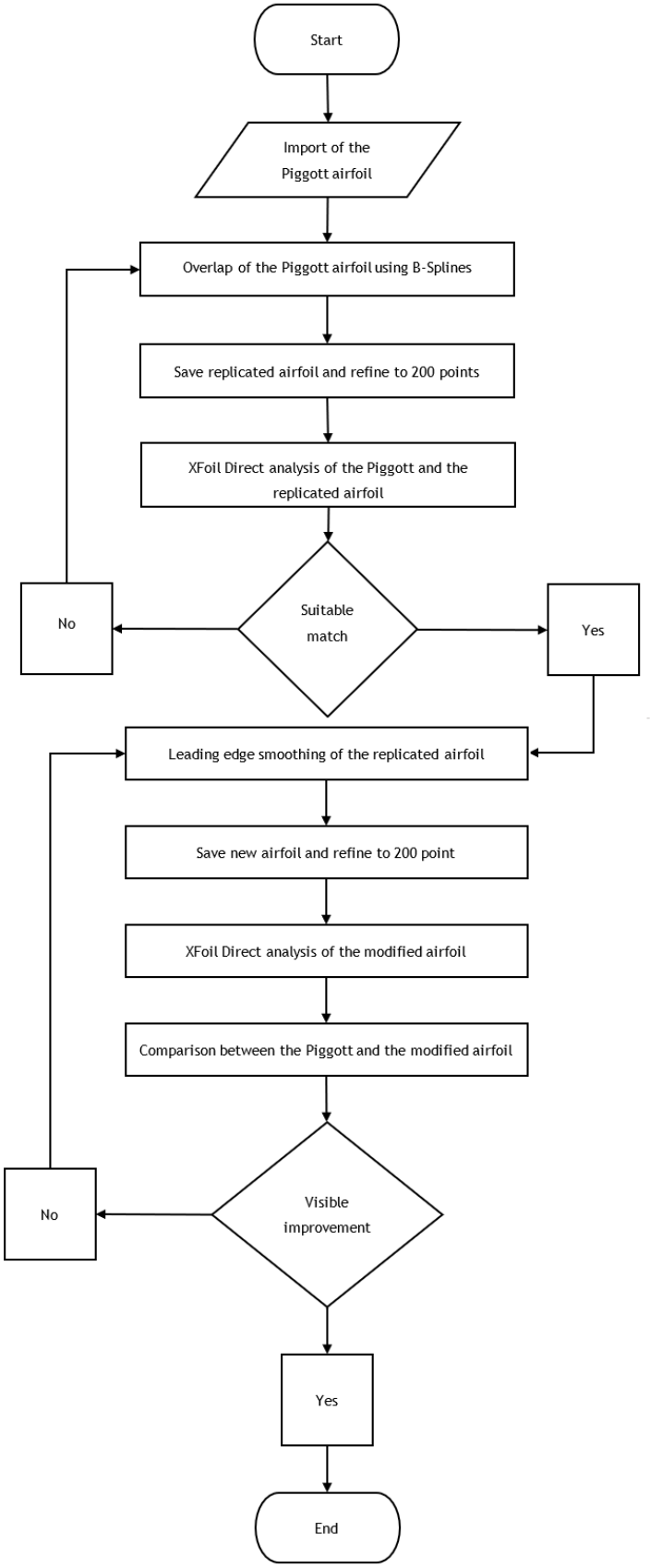

Figure 3.9: Flowchart of the method employed to obtain the smoother airfoil.

The flowchart of Figure 3.9 provides an initial insight of how the process occurred to develop the new airfoils, and a step by step description is followed that depict as an example, how the original section 4 airfoil (r = 300 mm) of blade 1 was used to create the corresponding new airfoil. The results from the digital scan performed to the rotor in [15] are illustrated by Figure 3.10, where 6 cross sections of the three blades are characterized by its chord, setting angle and the distance from the centre of the rotor. This data is used to perform the Blade Element Momentum simulations in Subchapter 3.4. For a better understanding, in this study the cross sections were numbered from 1 to 6, where section 1 (r = 600 mm) refers to the tip cross section, section 2 to r = 500 mm, section 3 to r = 400 mm, section 4 to r = 300 mm, section 5 to r = 200 mm, and the last section, 5, refers to the blade root cross section (r = 150 mm). Consequently, having 18 different airfoils, the presented method is repeated for all, resulting, as it is logical, in 18 new airfoils.

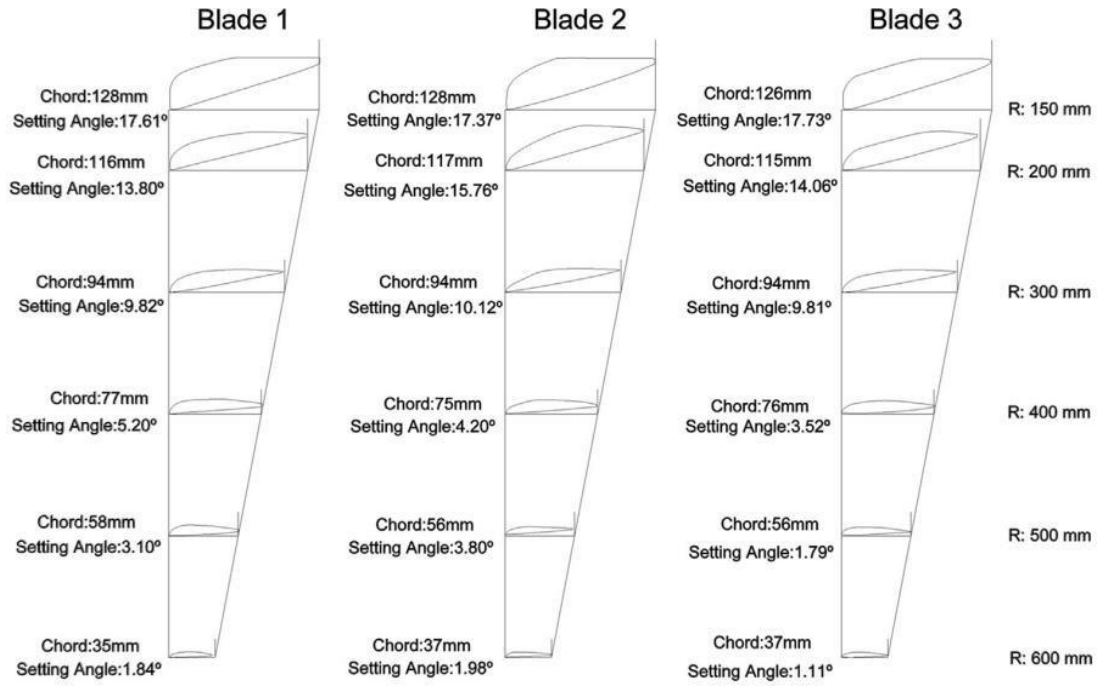

Figure 3.10: Digital scans of the blades of the rotor [15].

1. According to the flowchart (Figure 3.9), the first step is to upload the desired Piggott airfoil file into the newly created QBlade project. It is necessary that the file format is .dat and that the data points start in the trailing edge, move to the leading edge through the upper surface before going back to the trailing edge. The user may rename the airfoil by right clicking on the airfoil name as seen in Figure 3.11. Although the work presented in [15] was perfomed with the airfoils holding 100 points, every airfoil uploaded must be refined to 200 points to improve XFoil predictions [38]. The explanation of the refinement as well the comparison of the 200 points refinement with the 100 points results from [15] is presented is Chapter 4.

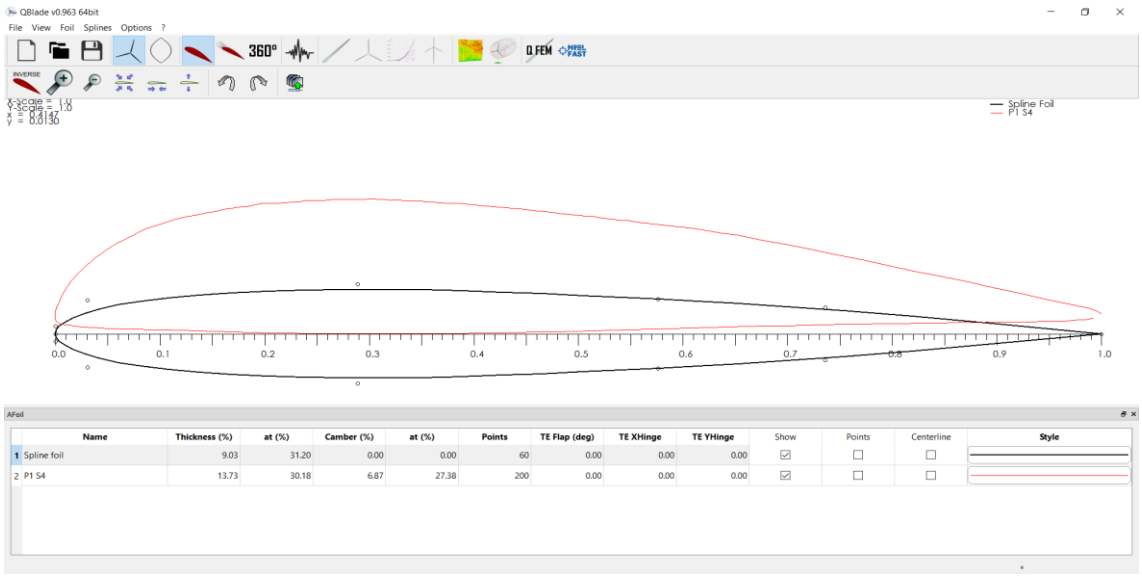

Figure 3.11: QBlade airfoil design module with section 4 (r = 300 mm) of blade 1 and standard spline foil.

2. Going through Figure 3.9, the second step is to overlap of the Piggott airfoil with the use of the spline foil available at the Airfoil Design feature. The user can change the spline shape by just clicking and dragging the control points to wherever is intended (Figure 3.11). Once the spline seems to proper replicate the Piggott airfoil, it must be stored with the desired name. Due to the spline foil standard number of points being 60, the airfoil stored must be refined to 200 points to be in accordance with the original one. Depending on the airfoil geometry, additional control points are required. To do so, first it must be selected the "Spline foil" at the panel in the bottom of the Arfoil Design module (Figure 3.11 has "Spline foil" selected). Secondly, right clicking in the place where the control point is desired will display a list of options, where "Splines" must be selected followed by "Insert Control Point". The standard spline is composed of two splines, upper and lower. To add a control point to the upper spline, the "right-clicking" must be done above the X-axis while to add a control point to the lower spline the right clicking must be done below the X-axis.
   Because the airfoil generated by this step is modified after, it is vital to ensure that both are aligned as possible to accurately replicate the original one (Figure 3.12). Subsequently, the replicated airfoil will be modified thus the importance of this step to sustain the comparison between the Piggott airfoil and the modified one.

3. With the airfoil replication step finished, the third step is to run the polar analysis for the Piggott and replicated airfoils in the XFoil Direct Analysis module. An analysis can be set up by either selecting in the upper toolbar "Analysis" followed by "Define an analysis" or clicking "New Polar" in the XDirect panel. For this comparison, a Reynolds numbers of 80,000 was set up; Mach and transition locations are left with standard values; as the critical amplification ratio in the simulations of [15] was of 8, Ncrit is set

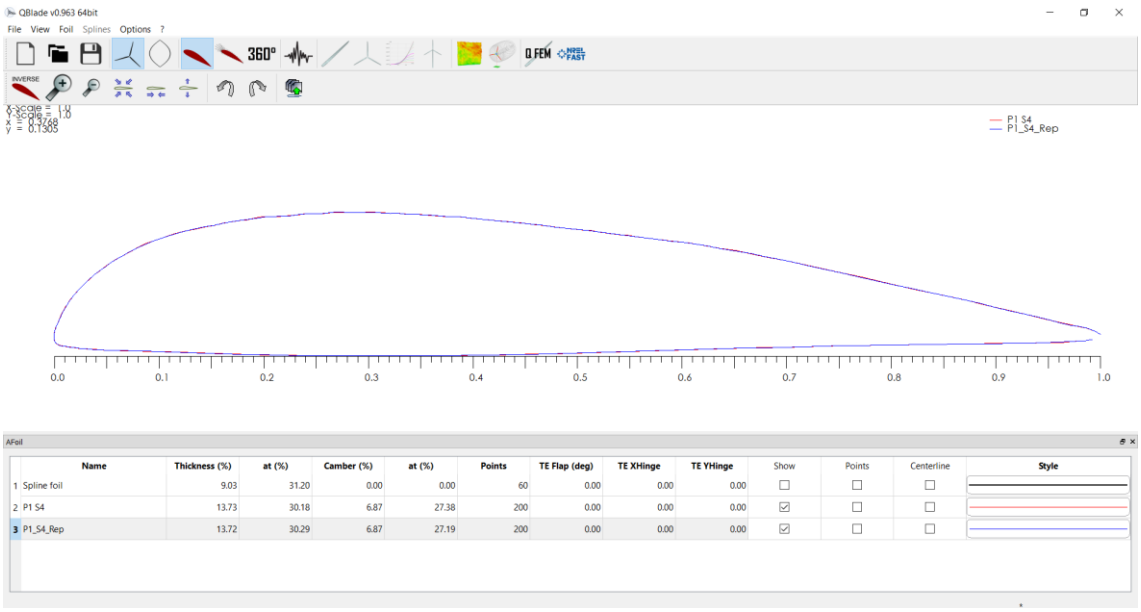

Figure 3.12: Piggott and replicated airfoil of section 4 (r = 300 mm) of blade 1.

to the same value (Figure 3.13); the angle of attack is set to be between [-5°,15°] and the incremental step to be 1 (Figure 3.14). The results of the two analysis are illustrated in Figure 3.15, where the Piggott and replicated airfoil are represented by a red solid and red dashed line respectively. If the analysis performed do not display consistent results, step 2 and 3 must be done again until reaching a good and close match to the Piggott airfoil.

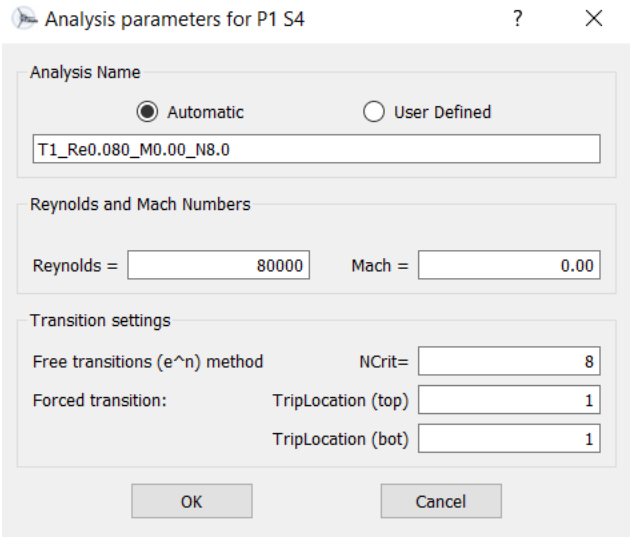

Figure 3.13: XFoil analysis parameters.

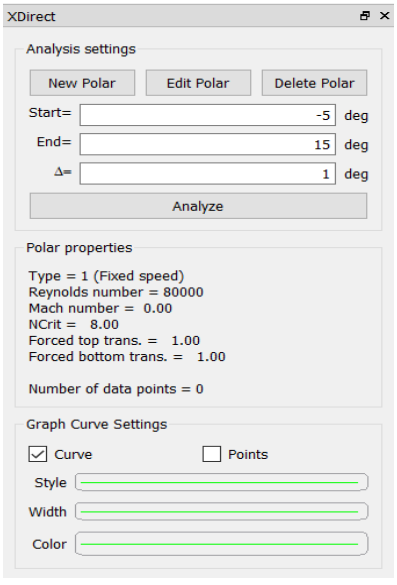

Figure 3.14: XDirect settings panel.

4. With a suitable match found, the modification of the reproduced airfoil takes place. With the standard foil having the shape of the reproduced foil, the next step is to modify the same spline by smoothing the leading edge towards the lower surface of the airfoil geometry. Additional control points will be needed to ease the task. Once again,

the spline must be stored with the proper name and refined to 200 points. In Figure 3.16, it is visible the modification made to section 4 of blade 1 by the green solid line.

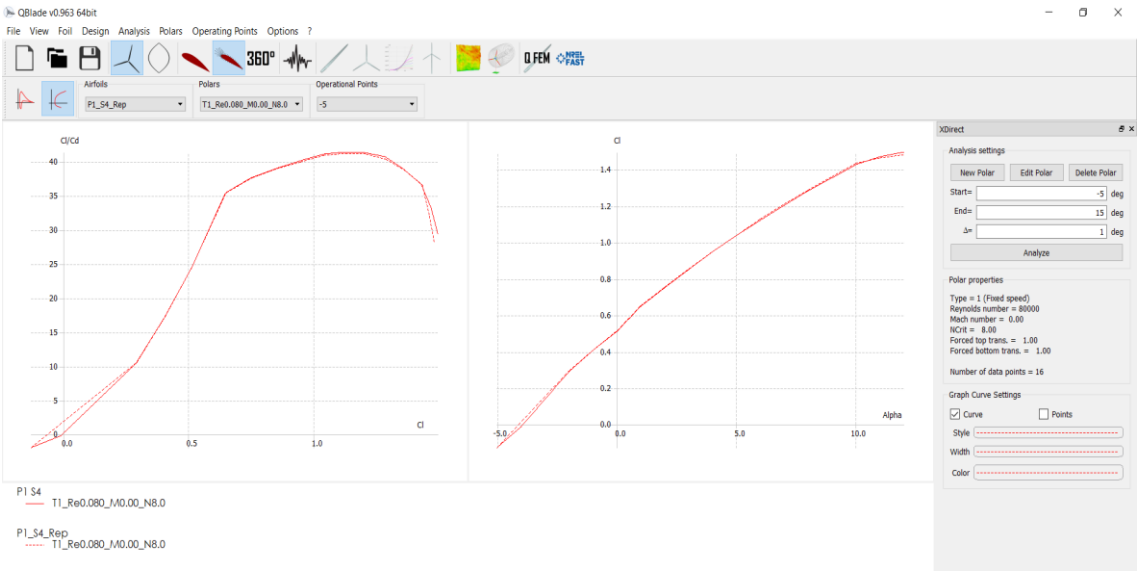

Figure 3.15: Blade 1 section 4 (r = 300 mm) polar analysis for the Piggott and replicated airfoil.

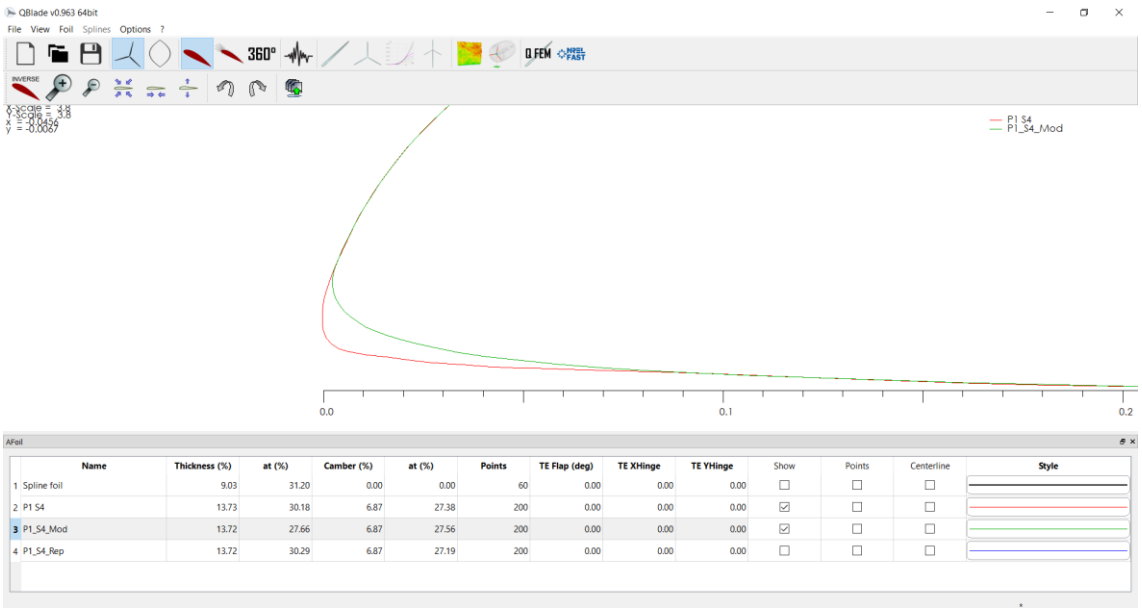

Figure 3.16: Blade 1 section 4 (r = 300 mm) Piggott and modified airfoil.

5. The following step is to run an analysis for the modified airfoil. With the same settings described in step 3, an analysis is performed to compare it with the Piggott airfoil. Figure 3.17 shows the analysis obtained for the original and modified airfoil in red and blue lines respectively. QBlade Airfoil design module supports up to 5 graphs at once but it would be difficult to visualize all 5 as they would appear small when copied and paste to this document. As the requirement of this study is the widening of the power coefficient curves, it was selected to show only the aerodynamic efficiency and the lift coefficient as the criteria parameters. This step is only complete when the modified

airfoil presents better performance than the original one and, if the modification does not result in a better performance, step 4 must be done again. The operation, as the flowchart shows, only ends when the new airfoil achieves better performance. The analysis results of the remaining airfoils are shown in Chapter 4.

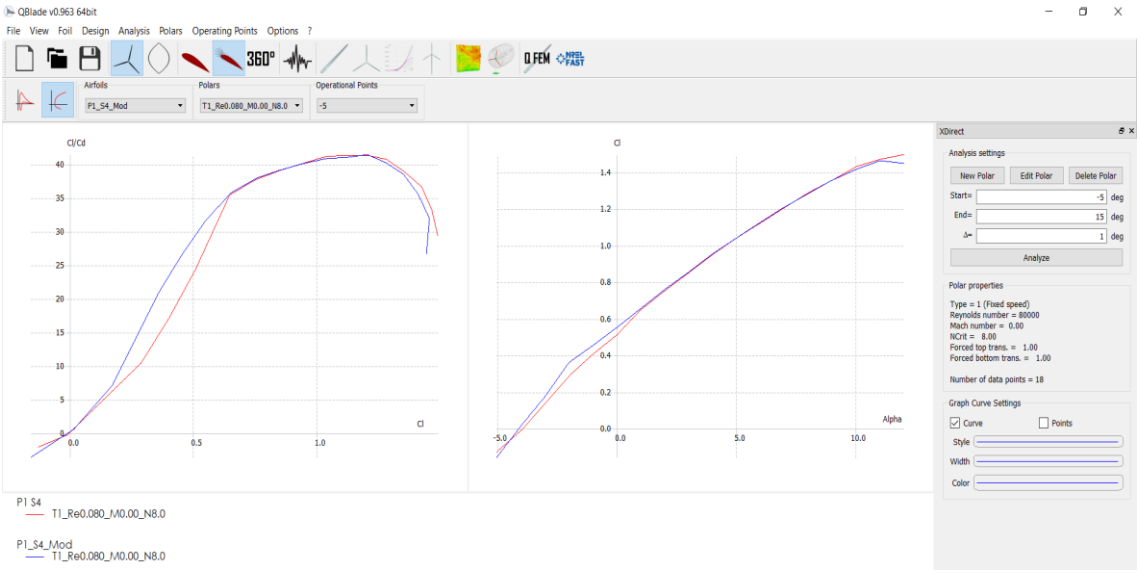

Figure 3.17: Aerodynamic efficiency and lift coefficient analysis for the Piggott and modified airfoil of blade 1 section 4 (r = 300 mm).

3.4 BEM Simulations

With the Piggott airfoils and the new ones created, QBlade is used to perform a dimensionless simulation to obtain data about the rotor power coefficient performance. This data is later used to compare the original and modified blades. A step by step description on how to set up the dimensionless simulations follows, taking as an example blade 3 with the Piggott airfoils. As the studied rotor consists of 3 geometrically different blades, and every blade is defined by 6 different airfoils, this procedure is repeated for each different blade (1,2 and 3) with the Piggott airfoils and with the modified airfoils. This mean a BEM simulation for an ideal rotor with three equal blades made up only of blade 1 airfoils, another ideal rotor with three equal blades regarding blade 2 airfoils and an ideal rotor with three equal blades characterized by blade 3 airfoils. First the procedure is done with the Piggott airfoils, and then is repeated but this time with the new airfoils. The HAWT tab must be selected at the upper toolbar. For further comprehension, Figure 3.18 resumes how to set up a rotor in QBlade to simulate its performance for the 6 windspeeds considered (3.0, 3.7, 4.4, 5.5, 7.2 and 7.7 m/s).

1. The first step as described in the flowchart of Figure 3.18, is to import all the 6 scanned Piggott airfoils of blade 3 to QBlade Airfoil design module (Figure 3.19). The user should check if all airfoils are refined to 200 points, to ensure enough numerical accuracy according to the work of [38].

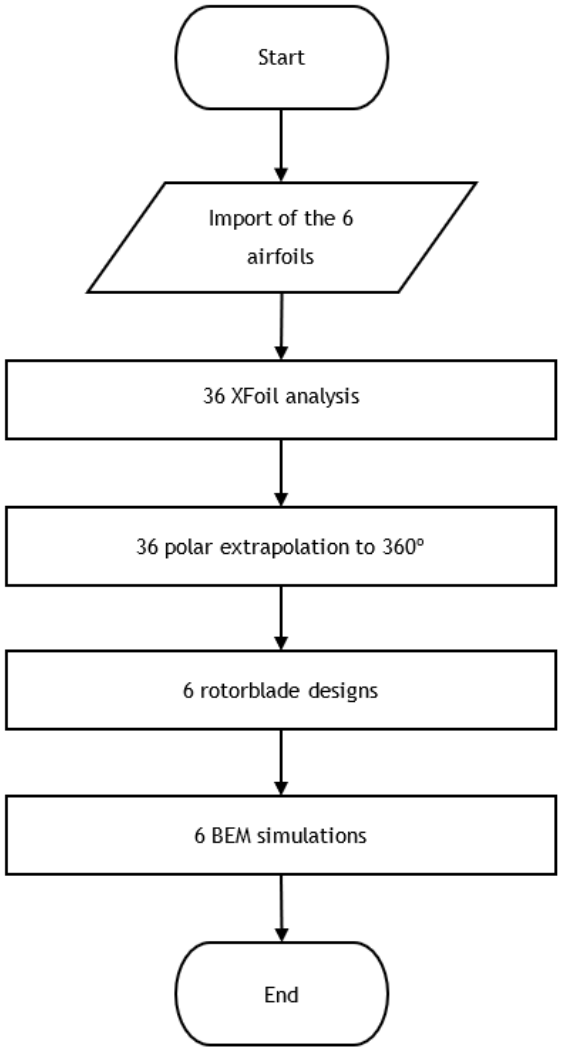

Figure 3.18: BEM simulation procedure flowchart.

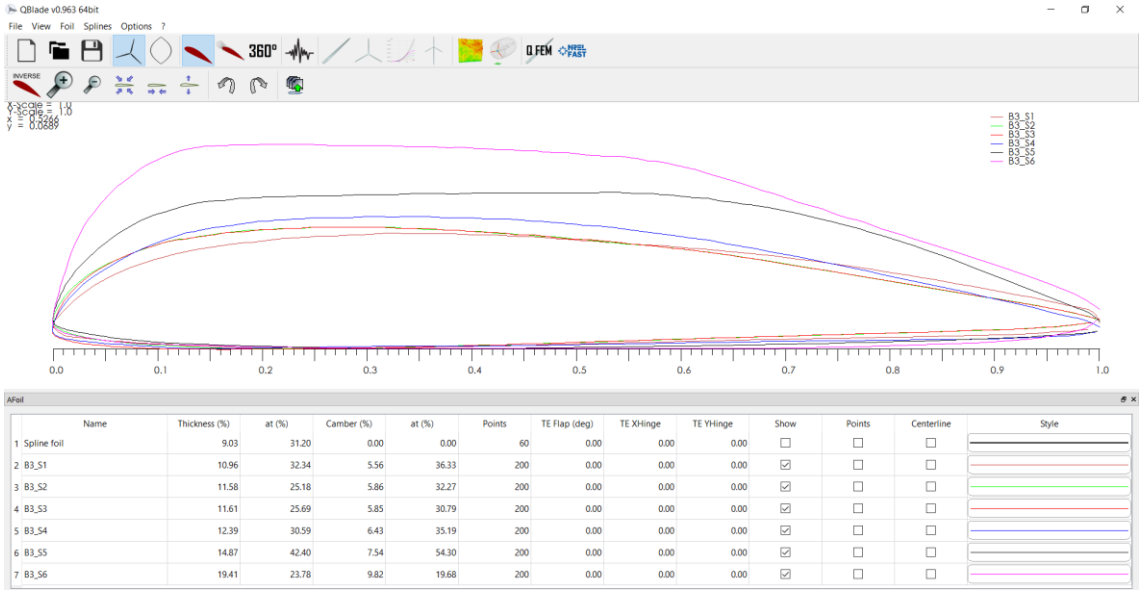

Figure 3.19: Blade 3 Piggott airfoils.

2. Following the procedure flowchart, the next step is to run the polar analysis in the XFoil Direct Analysis module. It is necessary to compute 36 analysis due to the 6 different wind speeds that the rotor was submitted to. Each airfoil has a different Reynolds number according to the designated wind speed and section position along the blade (Table 3.1). The air dynamic viscosity and density used to calculate each Reynolds number was of $1.82x10^{-5}\ Ns/m^2$ and $1.196\ kg/m^3$ respectively. It is simple to run an analysis as clicking in the "Analysis" menu at the upper toolbar (Figure 3.20), simply hitting F6 on the keyboard or clicking "New Polar" in the XDirect panel.

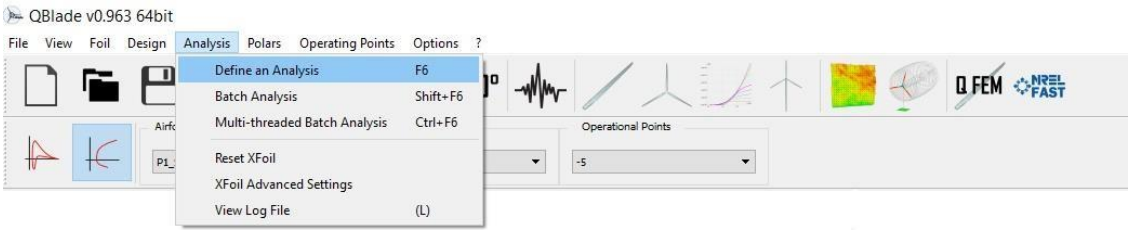

Figure 3.20: Analysis menu view.

Before running the analysis, the parameters must be set. The only parameter changing in all the 36 analysis is the Reynolds number. The transition number (Ncrit) is set to 8 to replicate the conditions specified in [15], and Mach, top and bot TripLocation are left with standard values (Figure 3.21). In this case, it was chosen to name every analysis according to the wind speed that the Reynolds number corresponded. When the analysis parameters are set, the final step before running the analysis is to set the XDirect analysis values located on the right side of the XFoil Direct Analysis sub-module (Figure 3.22). This feature allows to set the range and increment of the angle of attack for the analysis to be run, being [−5°, 25°] and 1 the corresponding values, and to choose the style, width and colour of the curve to be plotted as well as the option to visualize the points calculated. The 36 analysis performed for this example can be seen in Figure 3.23.

Table 3.1: Reynolds number according to the windspeed and radial position.

Windspeed [m/s]		3.0	3.7	4.4	5.5	7.2	7.7
Airfoil radial position [m]							
Section 6 Root	0.15	31687	38593	45485	56886	74834	80010
Section 5	0.2	37932	46199	54451	68098	89583	95781
Section 4	0.3	46189	56256	66305	82921	109083	116632
Section 3	0.4	48799	59436	70055	87609	115249	123226
Section 2	0.5	45764	55740	65699	82161	108083	115564
Section 1 Tip	0.6	37427	45586	53730	67193	88392	94152

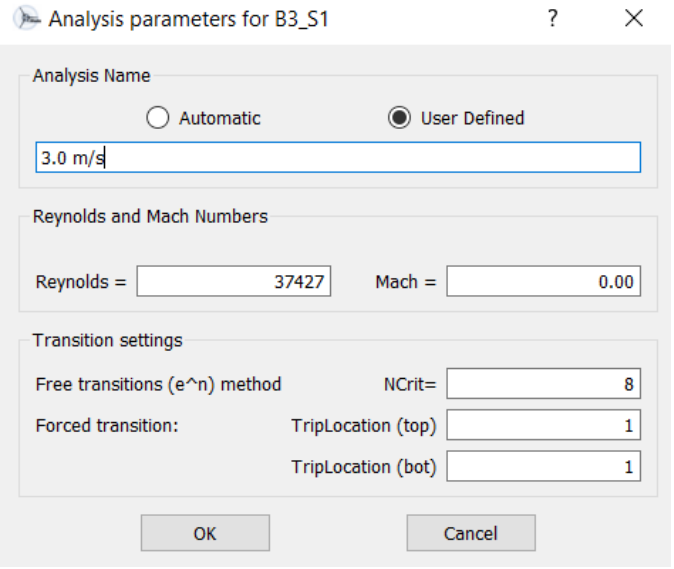

Figure 3.21: XFoil analysis parameters.

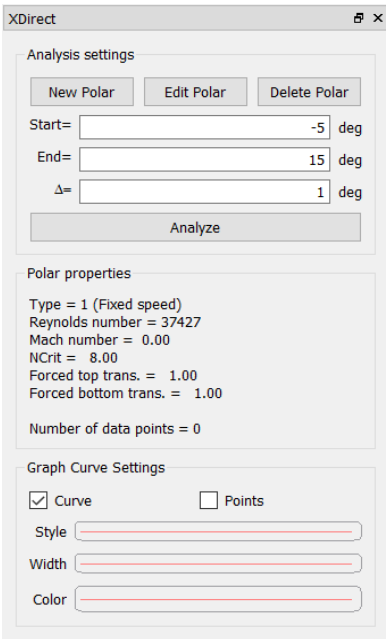

Figure 3.22: XDirect settings panel.

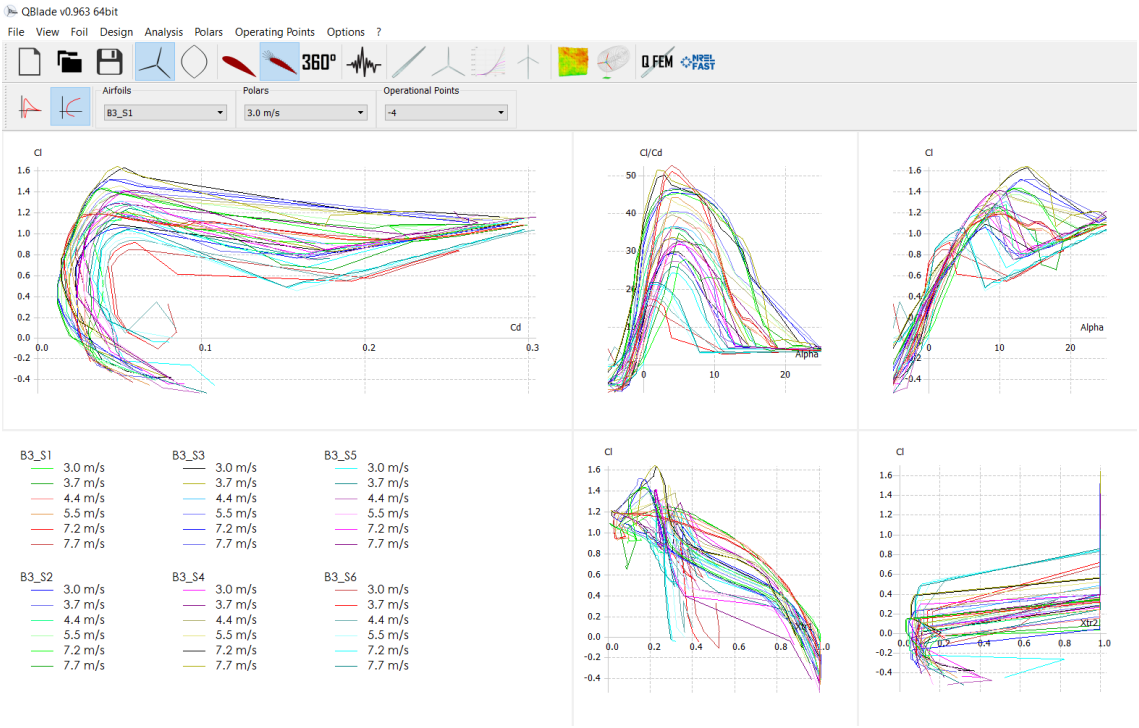

Figure 3.23: XFoil analysis for each windspeed of each section of blade 3.

3. With all 36 polars analysed, a polar extrapolation to 360° is needed as a final requirement to design the rotor. This is done by clicking in the Polar Extrapolation module visible with the number "360". In this step, 36 polars must be extrapolated by the Montgomorie approach and re-arranged using the "Finetuning of Polar" feature to smooth the connection between the polar and the 360º extrapolation. All other values were kept standard (Figure 3.24). This module interface shows 3 graphics whose

variables can be changed to what is more convenient. Above the left side panel, the user may select “Single Graph View” to ease the polar visual re- arranging. In Figure 3.25 it is possible to visualize the 3 m/s section 1 airfoil red line re-arranged polar and in green the non-re-arranged polar.

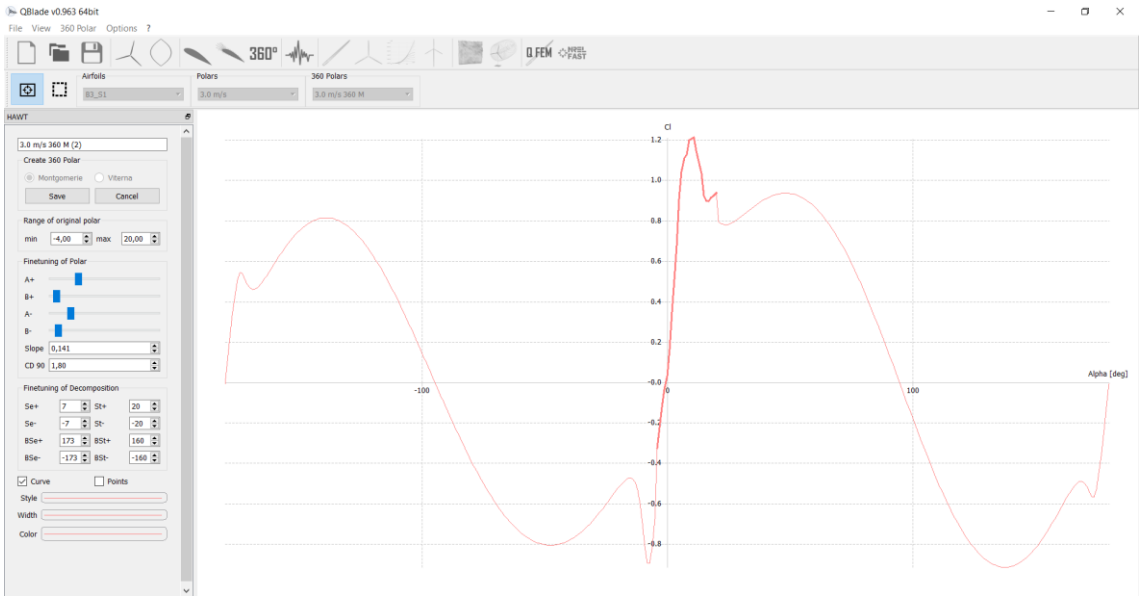

Figure 3.24: Blade 3 section 1 (r = 600 mm) 3.0 m/s polar extrapolation.

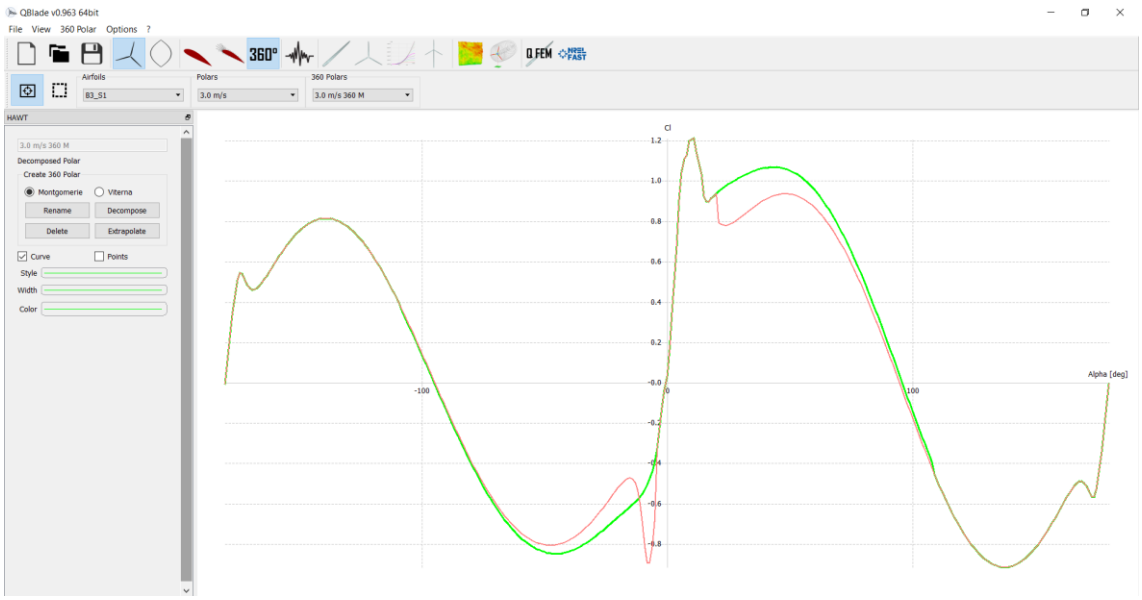

Figure 3.25: Re-arranged (green) and non-re-arranged (red) 360° polar.

4. As stated in the flowchart, in step number four the rotor is designed in the “HAWT Rotorblade design” sub-module. According to the different polars related to the wind speeds tested, 6 rotors must be designed for each blade, all with the same characteristics apart from the polars. If simulating blade 3, this means a rotor with polars concerning the 3.0 m/s windspeed, a rotor with the 3.7 m/s polars, a rotor with

the 4.4 m/s polars, a rotor with the 5.5 m/s polars, a rotor with the 7.2 m/s polars and a rotor with the 7.7 m/s polars. To start designing the rotor, the "HAWT Rotorblade design" module must be selected and then clicking "new" in the left panel. After, the blade must be designed according to its characteristics. All blades consist in 6 sections displaced on the same radial position with different chords and setting angles as seen in Figure 3.10 in the beginning of sub chapter 3.3. The airfoils are numbered from 1 to 6, meaning that 6 refers to the blade root section and 1 to the tip section. Hub radius is defined to be 0.15 m and the blade 3 rotor design is illustrated in Figure 3.26.

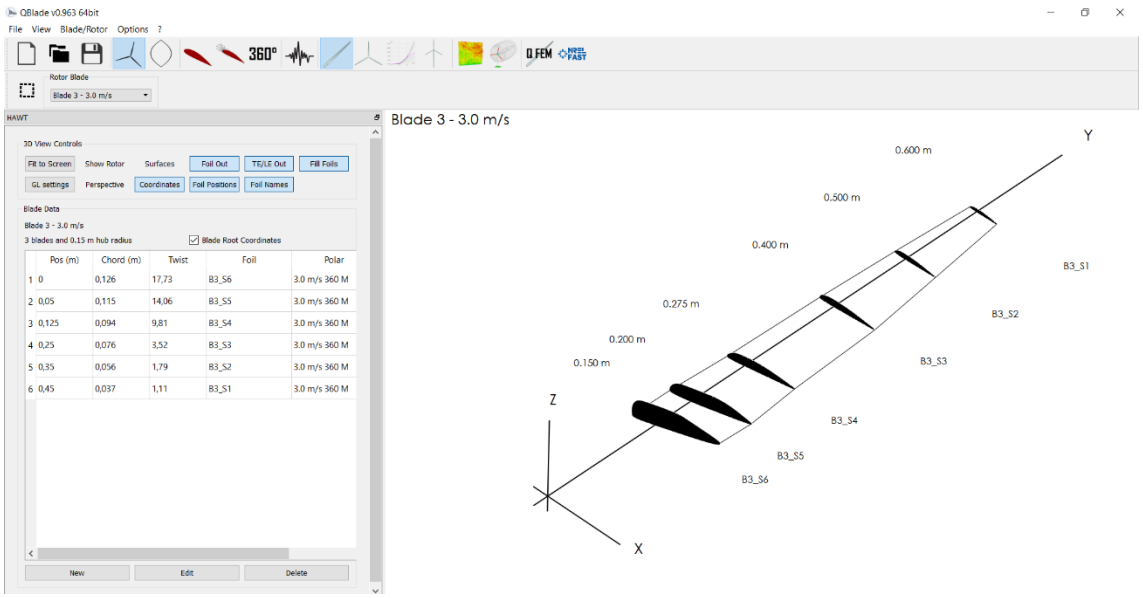

Figure 3.26: Blade 3 ideal rotor design with the Piggott airfoils for the 3.0 m/s polars.

5. The final step is the dimensionless simulation of the 6 different rotors designed in the previous stage. To do so, the "Rotor BEM Simulation" module in QBlade upper toolbar visible with a rotor must be selected. The desired rotor for simulation is chosen (Figure 3.27) and then, clicking in "Define Simulation" in the right panel entitled "HAWT Simulation Parameters" will display a window (Figure 3.28). In this window the simulation parameters are introduced. Prandtl Tip Losses, Reynolds Drag Correction and Foil Interpolation were selected in the corrections column while the variables are defined with the values visible in Figure 3.28. All these corrections selected and variables values are the same as the ones used in the simulations performed in [15].

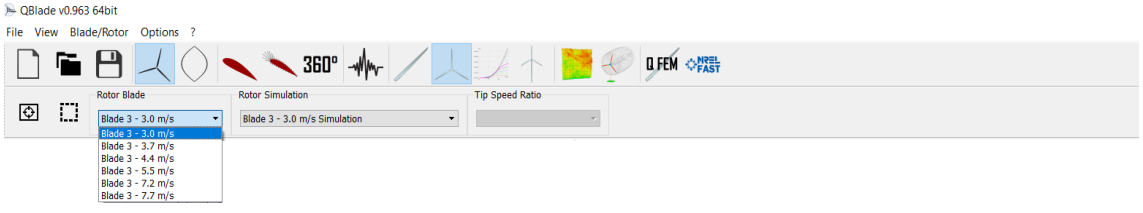

Figure 3.27: 3.0 m/s rotor selection for BEM simulation.

The Prandtl Tip Loss factor addresses the blade tip vortex to get a better agreement between wind turbines measured and computed data. Reynolds number drag correction is applied because QBlade does not include the changes in lift and drag polars due to Reynolds number effects. The polars are always computed for a fixed Reynolds number and during the turbine simulation, the Reynolds number is changing for every operational point. Foil interpolation is a simple solution to a problem that comes up during the discretization of the blade. A blade is defined in sections and every section may have a different airfoil. There is only polar data for the airfoils at every section but no data for the in between sections is present in the database. So, if the interpolation foil is switched on, the polar data of an element, is a linear interpolation between the polar data of the bounding airfoils, representing a more "true blade" geometry [31].

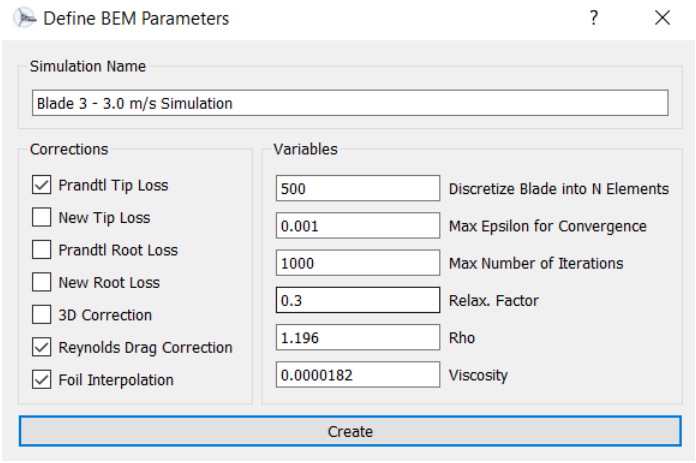

Figure 3.28: Blade 3 BEM simulation parameters for the 3.0 m/s rotor.

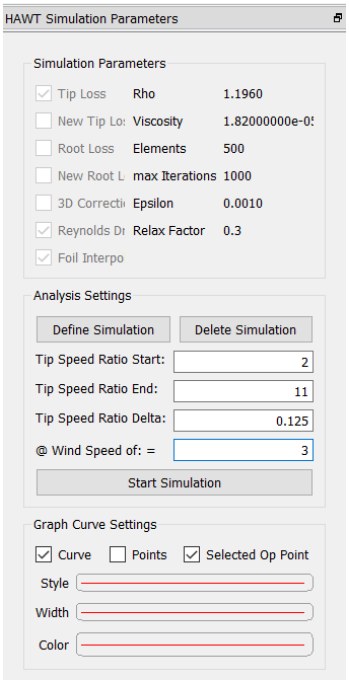

Figure 3.29: Analysis settings for the BEM Simulation.

The last step before the rotor dimensionless simulation requires to select a range of tip speed ratios and the incremental step. For every simulation done, both original and modified airfoils, the tip speed ratios range and incremental step was of [2, 11] and 0.125 respectively (Figure 3.29). After the simulation finishes, by selecting any of the graphic displayed it is possible to change x and y axis variables to what is more convenient. QBlade automatically displays a power coefficient and thrust coefficient over the λ graphics and a Reynolds number over the blade radial position. An important thing to bear is that the coefficient power curve might not converge in some cases for a λ greater than 6. To tackle this problem, changing the relaxation factor of the simulation to 0.2 or 0.1 should be enough for the simulation to converge (Figure 3.30).

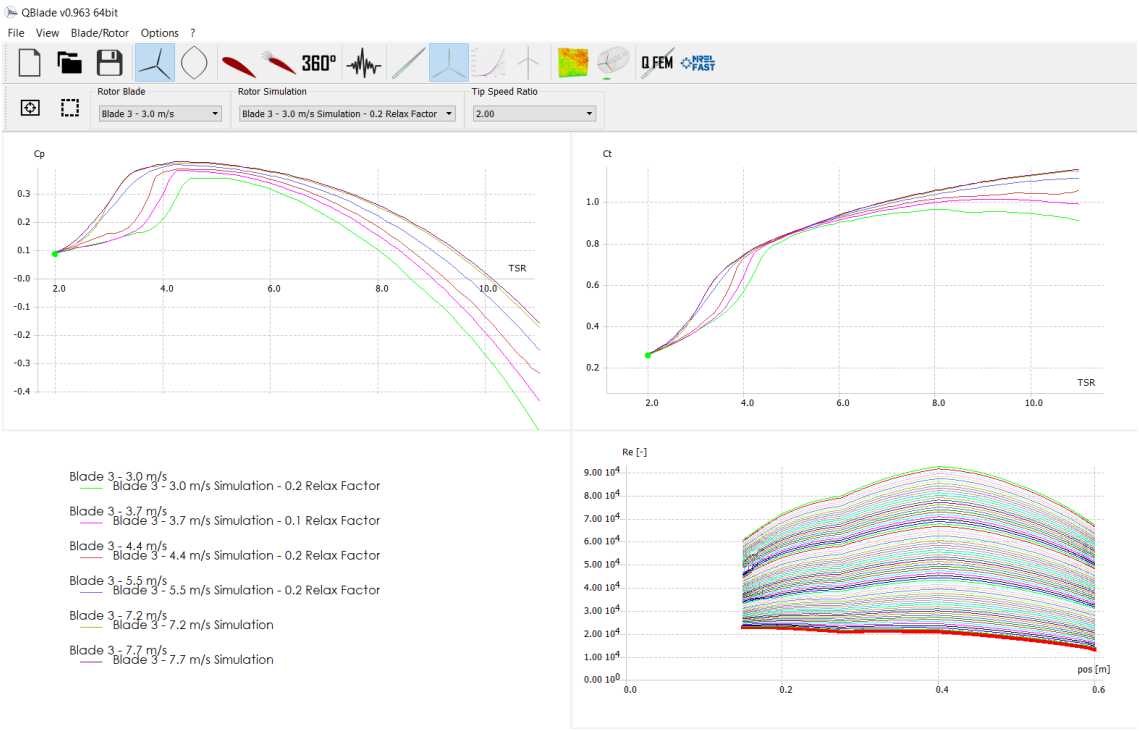

Figure 3.30: BEM simulations of the ideal rotor consisting of blade 3 Piggott airfoils.

3.5 Rotor Power Output

The graphics QBlade present are not enough to compare the data from the original and modified ideal rotors. With all simulations completed, the coefficient power data is exported in a .csv file to be handled more comfortably. Each file exported holds 6 different sets of data regarding the windspeed the ideal rotor simulation was done, being then plotted all windspeeds in a single graphic. As almost all sets of data have negative C_p values for high values of λ , the X coordinate for the Y coordinate (X,0) for every windspeed curve was calculated by linear interpolation (Equation 3.1). As this seems contradictory (plotting the same graphic that QBlade automatically shows), this is only done to later compare individually each original and modified ideal rotor windspeed curve. Figure 3.31 illustrates the 8 graphics resulting from this management, where every graphic is composed of 6 lines corresponding each to a different windspeed. Instead of plotting, as an example, the results of the ideal rotors consisting of three equal blades with the Piggott and modified airfoils of blade 1 in one graphic, as it would be difficult to visualize due to high number of curves (12), each windspeed simulation is plotted in a separated graphic. This means that, the 3.0 m/s windspeed curves of the original and modified ideal blade 1 rotor, are plotted in one graphic, repeating the step for the remaining windspeeds, therefore resulting in 6 graphics regarding blade 1. As there are 3 ideal rotors, 18 graphics in total are plotted. After averaging the 3 Piggott rotors and the 3 modified rotors, a graphic portraying the 6 windspeed curves is plotted for both, and the separation of the windspeeds curves is also done to better view the results. Figure 3.32 presents a flowchart that

resumes the number of graphics that are plotted for this windspeed curve comparison step (24 graphics).

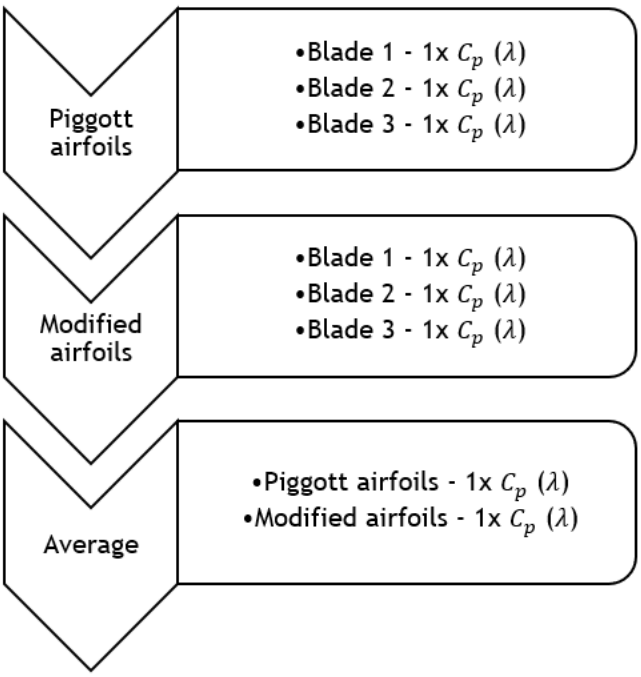

Figure 3.31: Flowchart of the Excel data management output.

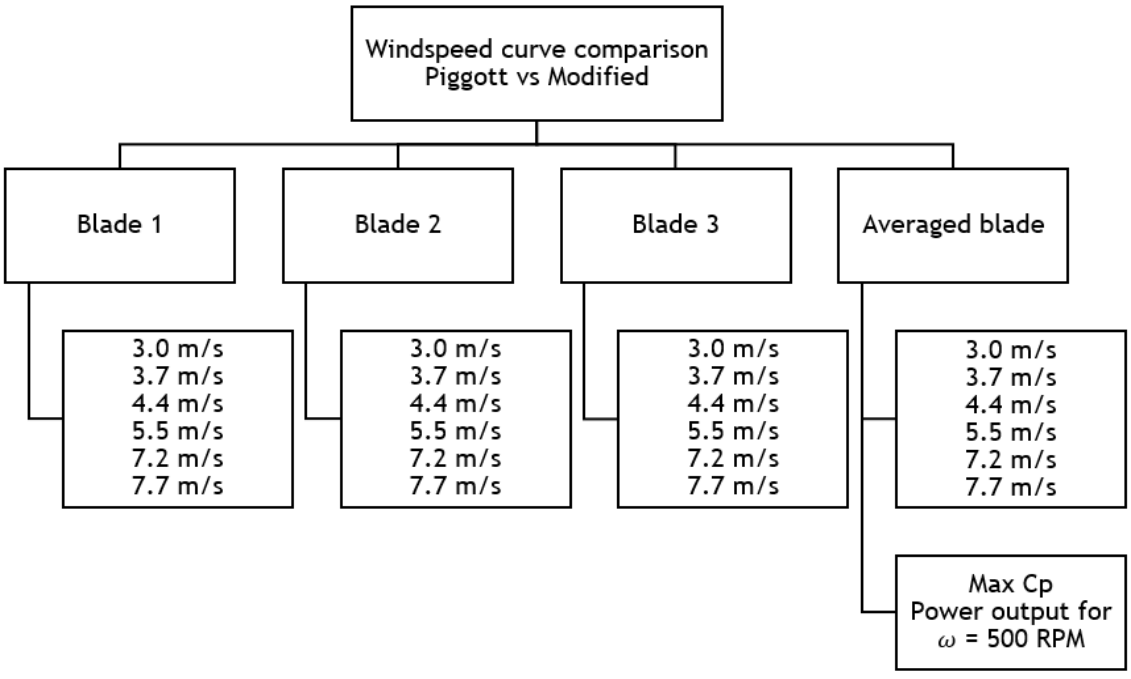

Figure 3.32: Flowchart comparison between the Piggott and modified windspeed data.

Figure 3.32 also shows that 2 more graphics were plotted regarding the averaged Piggott and modified rotors data, where one presents the maximum C_p of the Piggott and the modified rotor for the 6 windspeeds. The other graphic plots a hypothetical rotor power output if they

would operate at a ω = 500 RPM. The ideal rotors averaged data is used to calculate the turbine rotor power for a certain windspeed. Taking as an example the 3.0 m/s windspeed and using Excel to aid in this calculus, an increment of 50 RPM is set in a column ranging from 50 to 500 RPM. The rotational speed in RPM is converted to rad/s. Next step was the calculus of the λ using Equation 2.34, for each different ω, knowing the blade radius (R), the rotor area and windspeed (U) (Table 3.2). The Piggott and modified rotor C_p that corresponds to the previously λ calculated, is obtained by applying linear interpolation (Equation 3.1) from the Piggott and modified 3.0 m/s data correspondingly. Then, the power that the rotor extracts (Equation 2.21) from the available power in the wind (Equation 2.20) according to Subchapter 2.4.1 is calculated. Lastly, a column with the percentage change between the Piggott and the modified rotor power for the corresponding ω is displayed (Table 3.3). Although not mentioned in Figure 3.32, more graphics are plotted regarding another hypothetical scenario of an optimized turbine. To do so, the 3 blades modified airfoil analysis results of the same cross section are plotted in one graphic to compare which one holds the best performance. With the best airfoil of each cross section selected, the optimized rotor is simulated and the $C_p - \lambda$ results are compared to the results of the averaged rotor with the Piggott airfoils.

$$\frac{(x_1 - x_0)}{(y_1 - y_0)} = \frac{(x - x_0)}{(y - y_0)} \equiv y = y_0 + \frac{(x - x_0)(y_1 - y_0)}{(x_1 - x_0)} \quad (3.1)$$

Table 3.2: Blade radius, windspeed and air density for the 3.0 m/s rotor power.

R	0.6	m
Area	1.131	m^2
U	3	m/s
ρ	1.196	kg/m^3

Table 3.3: Averaged Piggott and modified rotor power for the 3.0 m/s windspeed.

			Piggott Rotor		Modified Rotor		
ω		λ	C_p	P	C_p	P	Δ P [%]
[rpm]	[rad/s]			[W]		[W]	
100	10.472	2.094	0.088	1.615	0.089	1.633	1.114
150	15.708	3.142	0.146	2.661	0.139	2.534	-4.805
200	20.944	4.189	0.235	4.290	0.230	4.194	-2.231
250	26.18	5.236	0.303	5.525	0.294	5.372	-2.775
300	31.416	6.283	0.240	4.376	0.238	4.342	-0.787
350	36.652	7.330	0.138	2.525	0.145	2.653	5.079
400	41.888	8.378	0.001	0.010	0.026	0.470	4580.442

3.6 General Procedure

All information presented in this section is summarized in the flowchart of Figure 3.33, where the first stage was to simulate the Piggott turbine (Subchapter 3.4) although the order in this section starts with the airfoils modification (Subchapter 3.3). This was done first, so it could be compared with the work of [15], in order to check if the results converge and thus, proceeding to the airfoils modification with a rigorous approach. Having all the Piggot airfoils smoothed (Subchapter 3.3), the simulation of the modified rotors followed (Subchapter 3.4). According to Subchapter 3.5, the Piggott and the modified turbine results are compared and, if not a better performance is accomplished, the airfoils must be handled again and the comparison process repeated. Once, and if possible, the modified turbine presents the expected results, the rotor power (Subchapter 3.5) of both turbines is compared. The last stage is the optimized turbine BEM simulation and the comparison between its performance and the averaged blade with the Piggott airfoils performance.

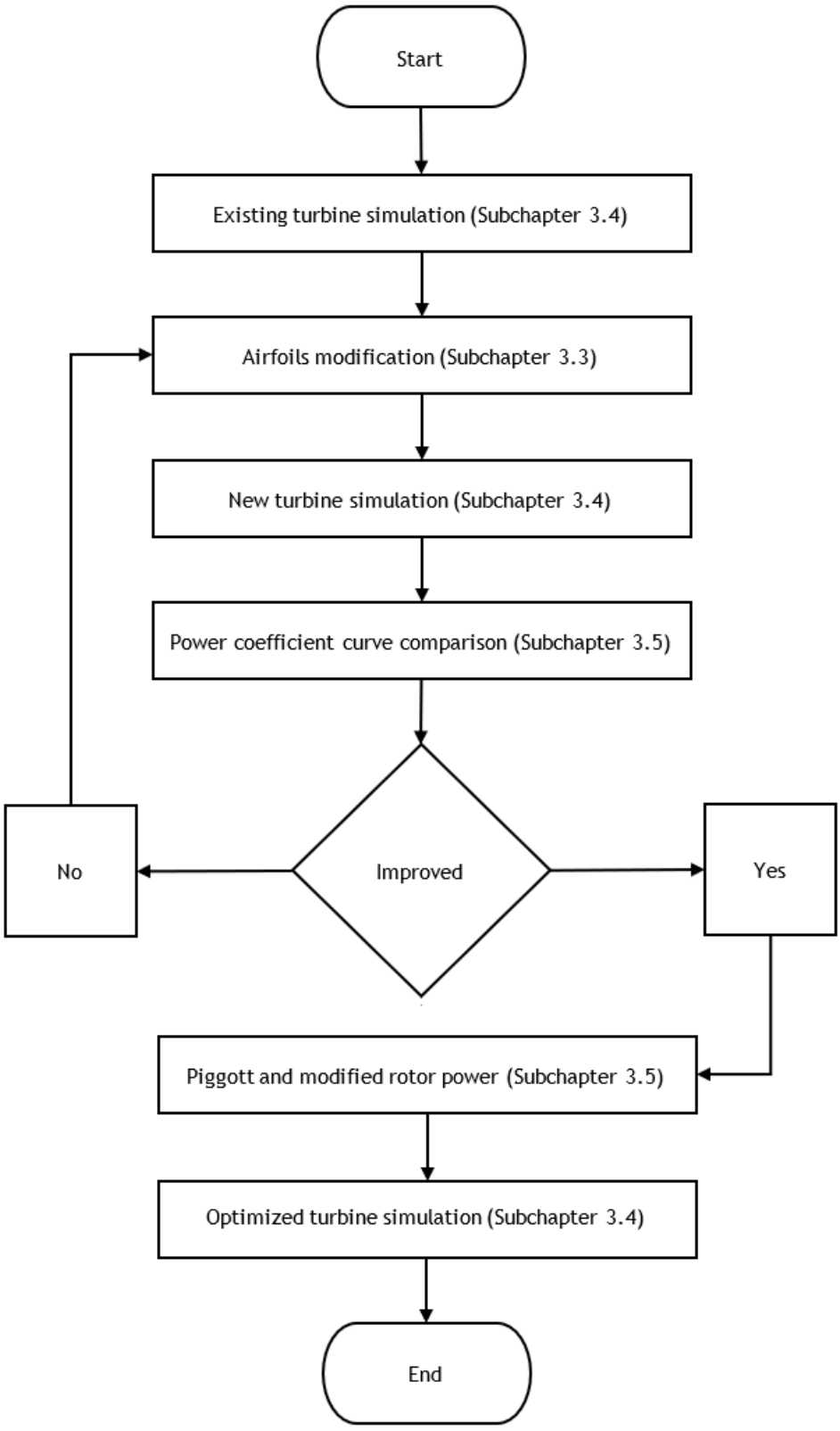

Figure 3.33: Flowchart of the wind turbine optimization general procedure.

Chapter4

Results and Discussion

This chapter addresses the results obtained from the airfoils modification on the rotor power output. The first section portraits the comparison of the $C_P - \lambda$ graphics between the averaged blade from (Monteiro et al) and the averaged blade with the Piggott airfoils from the BEM simulations performed as stated in Subchapter 3.4. As the modifications were taking place, the impact of the airfoils refinement in the XFOIL outputs became a concern as they were being done with 100 points. In the work of (Silvestre et al) it is shown that the XFoil simulations should be performed with more than 200 points for sufficient numerical accuracy. Upon knowing this, the method presented in Subchapter 3.4 was performed twice, one with 100 points and another with 200 points. This was done in order to get an accurate comparison to the simulations from (Monteiro et al) since they were performed with 100 points. Whereas the first section compares simulations with 100 points, the second section concerns the 200 points effect with the 100 points for the averaged blade with the Piggott airfoils.

The XFoil aerodynamic efficiency and lift coefficient data of every resulting new airfoil from Subchapter 3.3 is compared in Subchapter 4.3, to the respective blade and Piggott airfoil section. The airfoils leading edge difference is illustrated in Appendix B. The graphics expressed in Figure 3.32, concerning the BEM simulations of blades 1,2 and 3, are presented in Subchapter 4.4, where for each windspeed the Piggott rotor is compared to the modified rotor. The averaged blade with the Piggott airfoils and the averaged blade with the new airfoils is compared in the same way described previously and its results are presented in Subchapter 4.5. The results obtained if, for a hypothetical situation, the Piggott and the modified turbine would work with ω = 500 RPM are presented in Subchapter 4.6. This is close to the real case when the generator must provide constant voltage to charge the battery. The last section compares the results of the averaged rotor with the Piggott airfoils to the BEM results from an optimized turbine, that could be manufactured employing Computer Numerical Control technology. For each section, the modified airfoil of blade 1, 2 and 3 was compared and the best was selected to form the optimized turbine.

4.1 Methodology Validation Results

The full lines seen in Figure 4.1 represent the averaged blade performance from the work of [15] while the dashed lines are the simulations that were done following the method presented Subchapter 3.4 with the Piggott airfoils refined with 100 points. The first glimpse shows none of the lines match perfectly and overall, there is a positive offset for high values of λ. For the

lowest windspeed, 3.0 m/s, graphic A shows that the offset is almost constant throughout the curve of [15], being only closely valued in the region from λ = 4 to λ = 4.5, a behaviour also noted for the 3.7 m/s windspeed simulation (graphic B). As for the 4.4 m/s windspeed simulation (graphic C), the offset is negative from the extreme low λ values up to the maximum power coefficient, being positive from the power peak until the highest λ value. Graphics D and E, 5.5 m/s and 7.2 m/s correspondingly, share a behaviour where the dashed line is equal to the solid line in most of the low λ region but stands above the solid line little λ = 3.5 and it remains that way up to the highest λ value. The most extreme windspeed, graphic E regarding the 7.7 m/s, is characterized by a close match of both curves around a λ = 2.5 and having a significant positive offset from this point on up to the highest λ value. The maximum

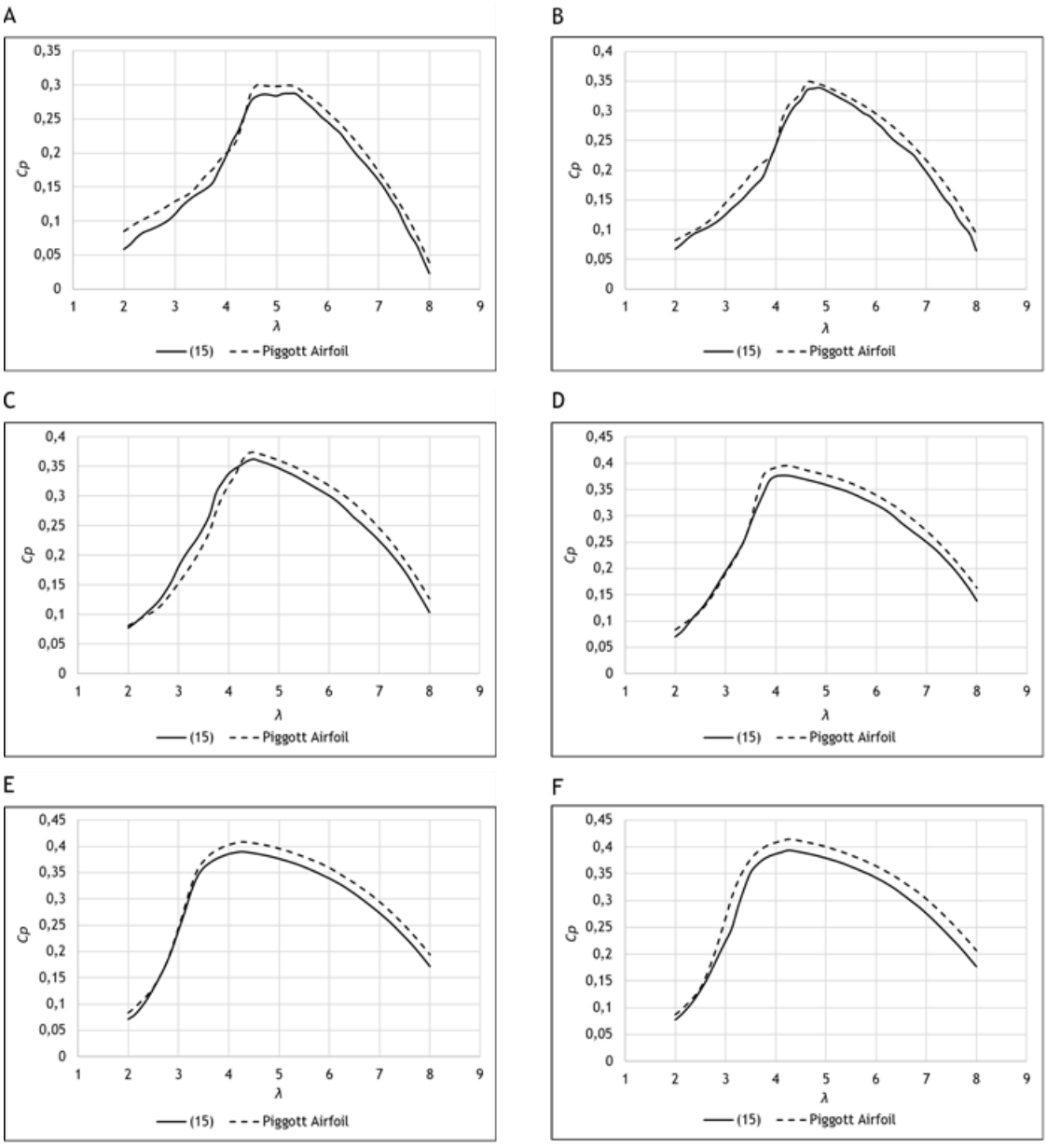

Figure 4.1: Averaged blade performance from [15] versus averaged Piggott blade performance from BEM simulations (A: 3.0 m/s; B: 3.7 m/s; C: 4.4 m/s; D: 5.5 m/s; E: 7.2 m/s; F: 7.7 m/s).

experimentally obtained peak in [15] for the 7.7 m/s windspeed was C_p = 0.40 for a λ = 4.8, a value close to that predicted by QBlade that was of C_p = 0.394 for a λ = 4.25. The simulations here portrayed by the dashed line for the 7.7 m/s windspeed found a maximum C_p = 0.415 for a λ = 4.25, meaning in a peak 3.6 % higher than the measured experimentally and 5.2 % higher than the numerical value obtained in [15]. In general, the results agree well but overpredict the performance estimated by those authors by about 5 %.

4.2 Airfoils Refinement Effect

The effect of the airfoils refinement on the simulation of the averaged blade with the Piggott airfoils is portrayed in Figure 4.2 where the solid line corresponds to the 100 points simulation

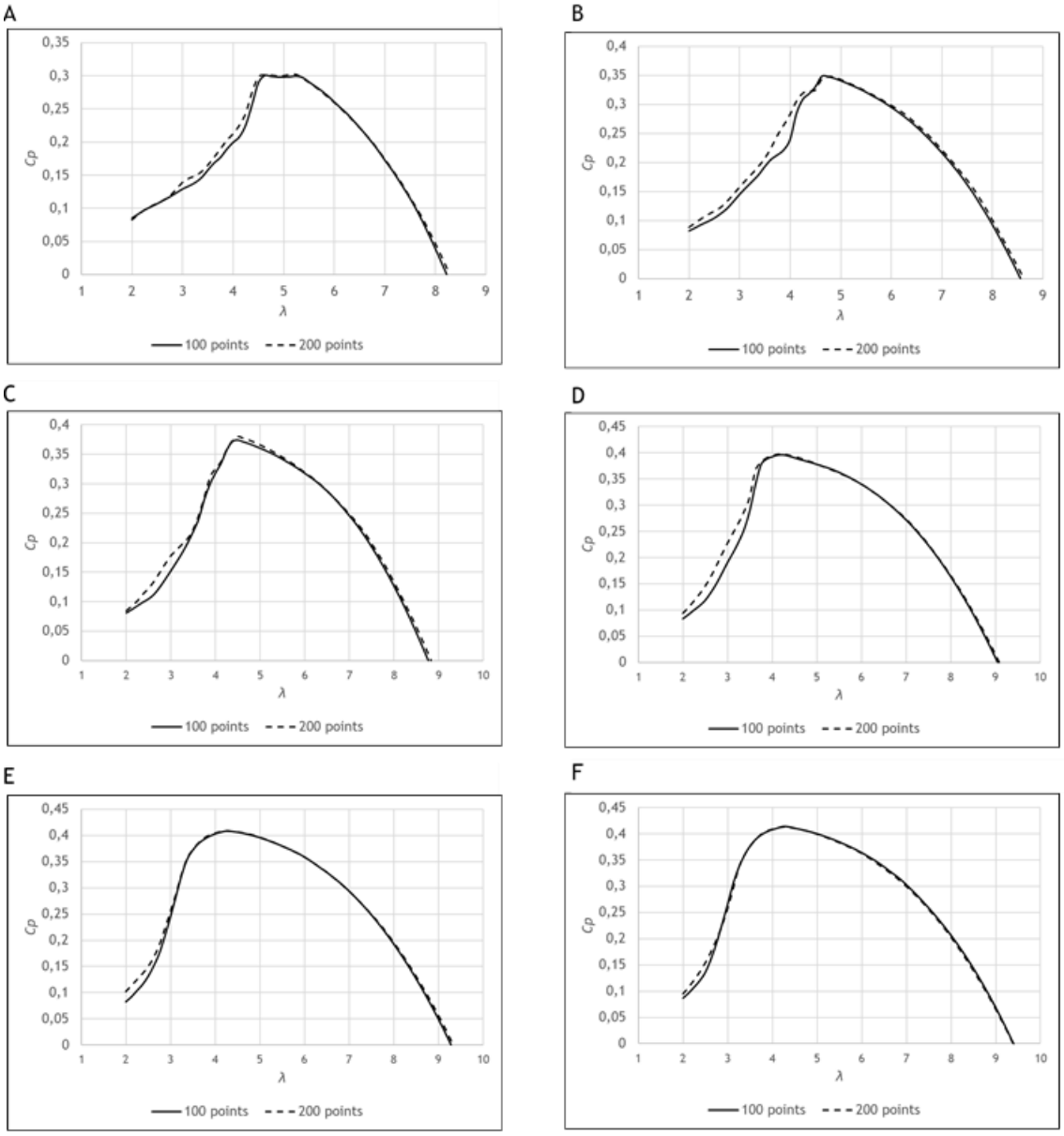

Figure 4.2: Averaged Piggott blade performance with 100 points versus 200 points (A: 3.0 m/s; B: 3.7 m/s; C: 4.4 m/s; D: 5.5 m/s; E: 7.2 m/s; F: 7.7 m/s).

and the dashed line to the 200 points simulations. The first graphic, A of the 3.0 m/s windspeed, shows that the 200 points simulation curve estimates better performance from a λ = 3 up to the power peak, around a λ = 4.5, and a marginal improvement after a λ = 8 up to the highest λ value. The 200 points curve of graphic B (3.7 m/s) presents a strong positive offset for the low λ region until the power coefficient peak and a slight improvement after a λ = 6 up to the highest λ value. Between the power peak that occurs around λ = 4.5 and λ = 6, both curves present the same behaviour. As for the 4.4 m/s windspeed simulations (graphic C), in an ascendant way, the 200 points curve presents better performance between the lowest λ and λ = 3.5, matching the 100 points curve up to the power peak although the 200 points predicts a slightly better power peak. From this point on until the highest λ value, the 200 points curve exhibits marginal better performance except between λ =6 and λ = 7. For the 5.5 m/s windspeed graphic, D, the 200 points simulation predicts better performance in the low λ region up to the power peak but with no improvements from this point on up to the highest λ value. The last two graphics E and F, of the 7.2 m/s and 7.7 m/s windspeed respectively, portrays no refinement effect except between the extreme low λ and λ = 3, where the 200 points curve shows better performance than the 100 points curve. These results are in better agreement with the work of [38] as the refinement predicts better performance, in this case, mostly for low windspeeds and at the same time for low values of λ.

4.3 Modified Airfoils Results

4.3.1 Blade 1

The smoothing results of the Piggott airfoils of blade 1 are presented and compared by analysing their aerodynamic efficiency and lift coefficient data from the XFoil simulations. Figure 4.3 presents the results of blade sections 1,2 and 3 while Figure 4.4 shows sections 4, 5 and 6. For the first section of blade 1 (tip), the new airfoil does not present any aerodynamic efficiency improvement (graphic A of Figure 4.3). While its maximum lift coefficient decreased 4.6 % compared to the Piggott airfoil, it does present a better lift coefficient for an AoA between -2 and 0 (graphic B of Figure 4.3), and a marginal improvement of the aerodynamic efficiency for this lift coefficient interval. The modified airfoil of blade section 2 (graphic C and D) also does not present any aerodynamic efficiency improvement but rather a disturbance around a lift coefficient of 1.2, and its maximum lift coefficient decreases compared to the Piggott airfoil (Δ = 0.008). The aerodynamic efficiency of the new airfoil regarding blade section 3 (graphic E) presents a significant better performance than the original Piggott airfoil between a lift coefficient of 0.2 and 0.8, having a maximum increase of 20 % at a lift coefficient of 0.6 (Δ = 5.243). This new airfoil lift coefficient (graphic F) is better than the Pigggott airfoil between an AoA of -2 and 2, although it presents worse performance from this point up to the maximum lift coefficient, that is 0.28 % worse than the Piggott maximum lift coefficient.

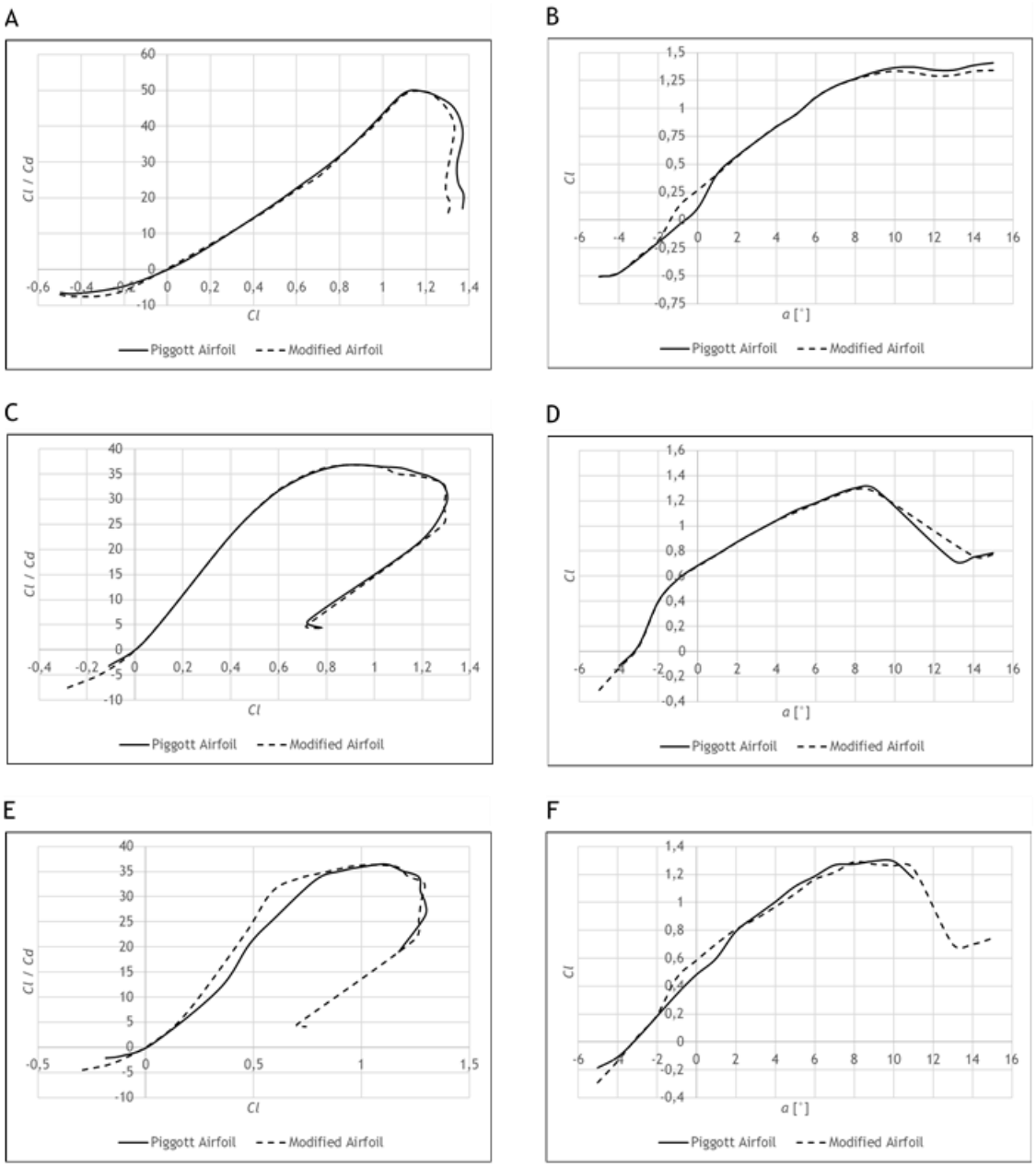

Figure 4.3: Aerodynamic efficiency and lift coefficient comparison between the Piggott and the modified airfoils of blade 1 (A,B: Section 1; C,D: Section 2; E,F: Section 3).

Analysing now Figure 4.4 which presents the XFoil simulations of the remaining 3 blade sections of blade 1, in graphic A is visible, that the aerodynamic efficiency of the modified airfoil of section 4 presents better performance between a lift coefficient of 0.1 and 0.6, with a maximum aerodynamic efficiency difference of $\Delta = 7.2$ for a lift coefficient of 0.4. The Piggott airfoil behaves better after a lift coefficient of 1.2. As for its lift coefficient (graphic B), the new airfoil shows a slight 2.3 % decrease of the lift coefficient peak. Somehow, the Piggott XFoil simulation of blade section 5 does not present linear results as the ones seen in graphic A and B. Nevertheless, the modified airfoil presents significantly improved aerodynamic efficiency for a lift coefficient between 0.2 and 1, with a maximum increase of 30.5 % for a lift coefficient of 0.7. The new rotor is only overpassed by the Piggott airfoil after a lift coefficient

of 1.4. Regarding graphic D, the modified airfoil has a slight better lift coefficient between an AoA of -1 until 9 and, presents an earlier lift coefficient peak (α = 10 °) that is 0.58 % higher than the Piggott airfoil peak that occurs for α = 12 °. As for the last section of blade 1 (root), the aerodynamic efficiency results seen in graphic E show that the modified airfoil stands expressively over the Piggott for almost all lift coefficients, with a maximum difference of 3.8 for a lift coefficient of 0.7, that represents an increase of 23.2 %.The new airfoil of section 6 presents for the same AoA (5 °) a 1.28 % better lift coefficient peak (graphic F) and is expressively better than the Piggott airfoil between an AoA of -2 and 3, achieving a maximum outstanding absolute difference of 26 at a AoA of 1.

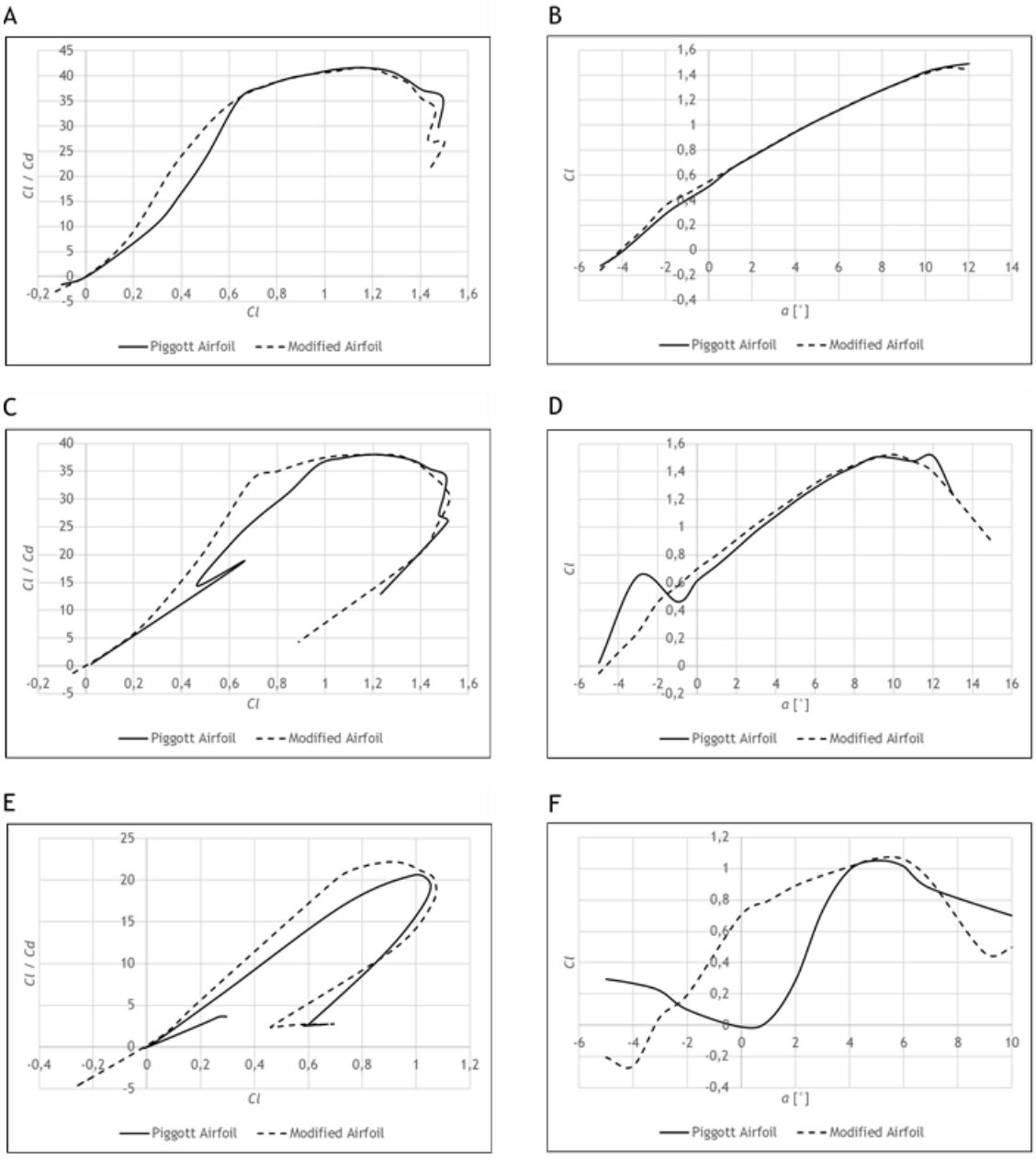

Figure 4.4: Aerodynamic efficiency and lift coefficient comparison between the Piggott and the modified airfoils of blade 1 (A,B: Section 4; C,D: Section 5; E,F: Section 6).

4.3.2 Blade 2

About the XFoils simulations of blade 2 airfoil sections, the results are illustrated in Figure 4.5 and 4.6, where the sections are divided such as in the previous section. The blade tip section is characterized by an expressive better result of the modified airfoil aerodynamic efficiency between a lift coefficient of 0.1 and 0.8 (graphic A), with an absolute difference of 2.5 for a lift coefficient of 0.33 that corresponds to an increase of 6.5 %. It also presents a higher peak than the Piggott airfoil (6.6 %) but followed by a steep fall, where from this point on, its performance is worse compared to the Piggott airfoil. From graphic B, the modified airfoil presents a worse performance than the Piggott airfoil for high AoA with a 5.8 % decrease in the

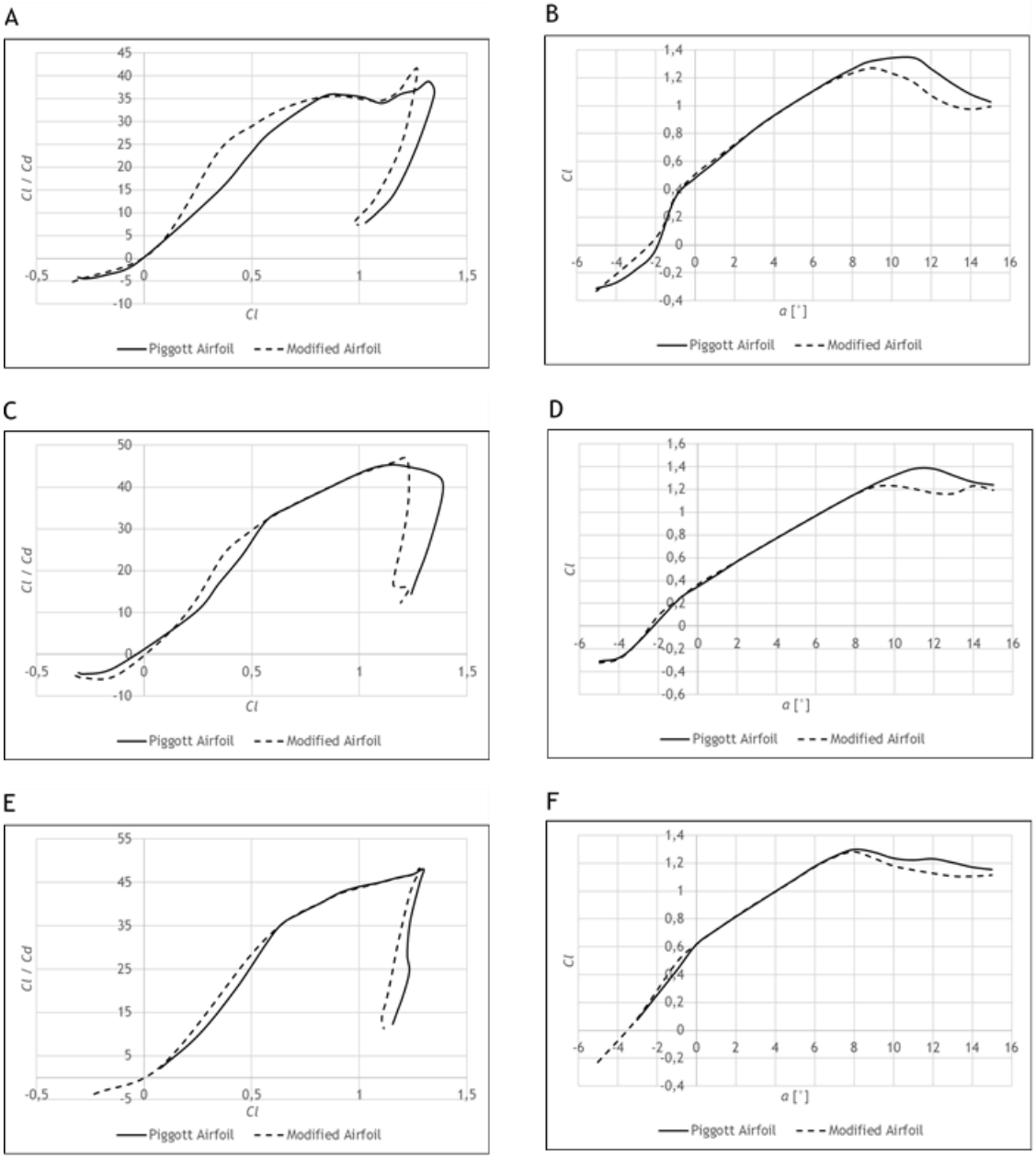

Figure 4.5: Aerodynamic efficiency and lift coefficient comparison between the Piggott and the modified airfoils of blade 2 (A,B: Section 1; C,D: Section 2; E,F: Section 3).

maximum lift coefficient, and its performance is only slightly better between an AoA of 0 and 2. The XFoil results of the second section of blade 2 behave almost identically to those of section 1. In graphic C, the modified airfoil of blade section 2 starts by having a lower aerodynamic efficiency than the Piggott airfoil until a lift coefficient of 0.1. From this value up to 0.6, the modified airfoil performs better with a maximum 25 % increase for a lift coefficient of 0.4. The two airfoils present the same performance from a lift coefficient of 0.6 up to 1.22. The modified airfoil in this point presents a higher aerodynamic efficiency peak (2.5 %) than the Piggott airfoil but followed by a vertical fall, being overcome by the Piggott airfoil for the higher end of the lift coefficient values. As for the lift coefficient performance (graphic D), the modified airfoil does not present any significant improvements over the Piggott airfoil but it does display a substantial lower peak (11.1 % drop in the maximum lift coefficient value) than the Piggott airfoil. The Piggott airfoil XFoil simulation of blade section 3 did not converged for low lift coefficient values (graphic E) but nonetheless, the modified airfoil presents better performance up to a lift coefficient of 0.6, having then the same behaviour as the Piggott airfoil until 1.3. Both airfoils present the same aerodynamic efficiency peak followed by a steep fall, where the Piggott airfoil stands better. As for the lift coefficient performance (graphic F), the modified airfoil does not present better performance for positive angles of attack and exhibits a slightly lower peak than the Piggott airfoil (1.3 %), as well as its performance after the peak is slightly poorer than that of the original airfoil.

The fourth blade section XFoil simulation is somewhat quite exquisite as it is illustrated by graphic A and B of Figure 4.6. This section was probably the one that took more work and attempts for an improved airfoil. From graphic A, it is seen that the modified airfoil performs better until a lift coefficient of 0.5. From there it reaches a higher peak than the Piggott airfoil but rapidly falls to the same aerodynamic efficiency as the original airfoil at a lift coefficient of 0.7, where it gets back to stand better than the Piggott airfoil up to 0.9, where it is noticed another peak that is followed by a vertical fall. From graphic B, the lift coefficient does not present a linear behaviour, where the new airfoil has better performance around an AoA of 8 and from 10 to 12. The new airfoil exbibits a lower lift coefficient peak (0.1 %) than the Piggott airfoil peak, both for an $\alpha = 12\ ^\circ$. If blade section 4 airfoils are characterized by such random results, blade section 5 airfoils (graphics C and D) present almost linear curves. The new blade section 5 airfoil is characterized by a small positive offset of the Piggott aerodynamic efficiency curve and by a slightly higher peak of 2.4 % (graphic C). The same description applies to graphic D where a better performance of the new airfoil lift coefficient between an AoA of -2 and 7 is observed. As for the last section, corresponding to the blade root, in graphic E, the new airfoil exhibits a substantial improvement between a lift coefficient of 0.6 and 1, having the aerodynamic efficiency peaks an absolute difference of 1.36 that results in an increase of the new airfoil peak of 14.5 %. Observing graphic F, the new airfoil converged for a greater range of AoA than the Piggott airfoil, presents better performance up to an AoA of 13, and exhibits a

higher (4.6 %) and earlier (α = 12 °) lift coefficient peak than the Piggott peak that occurs for an α = 13 °.

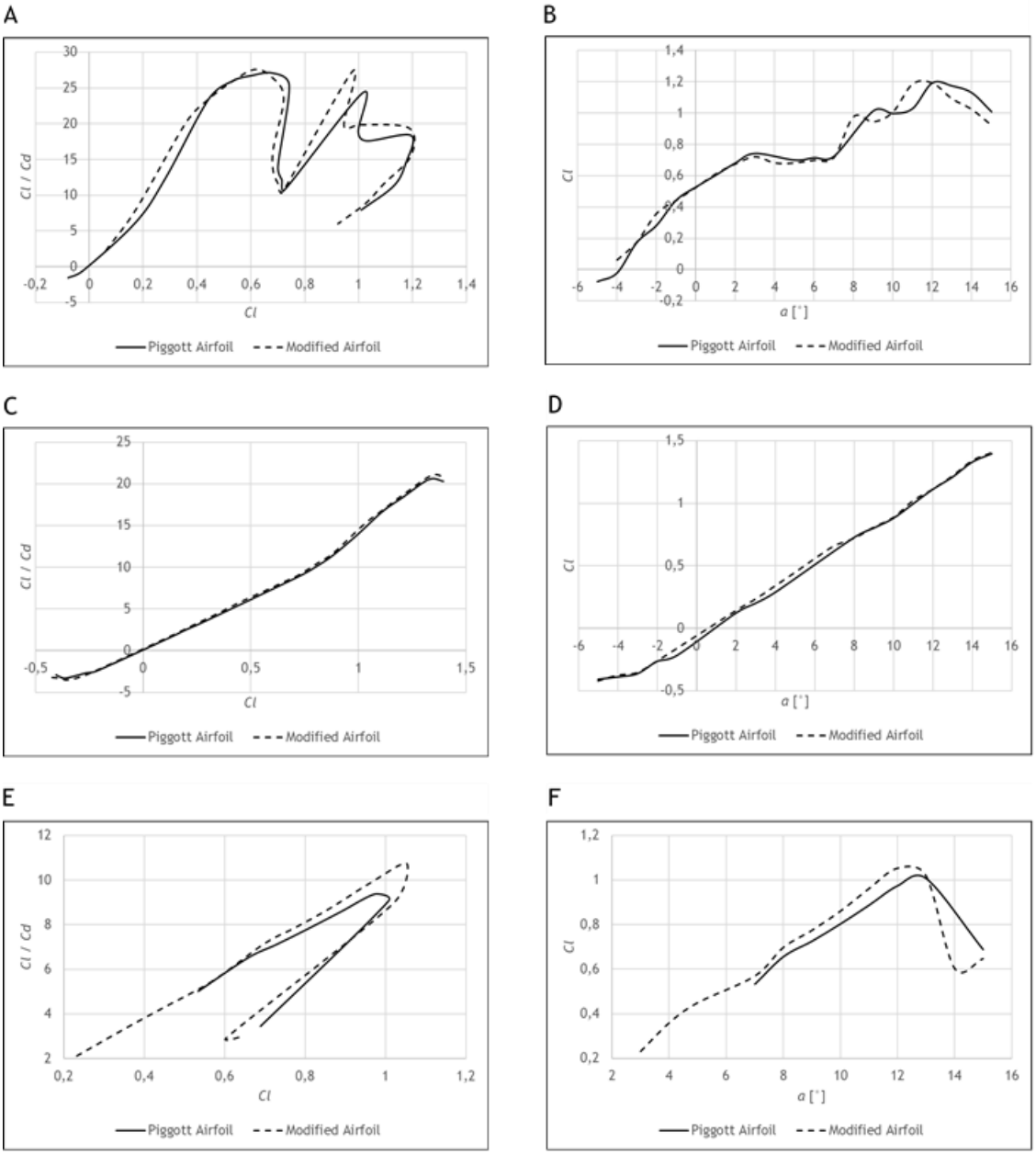

Figure 4.6: Aerodynamic efficiency and lift coefficient comparison between the Piggott and the modified airfoils of blade 2 (A,B: Section 4; C,D: Section 5; E,F: Section 6).

4.3.3 Blade 3

By observing Figures 4.7 and 4.8, it is seen that the new airfoils of blade 3 do not present significant improvements except for blade section 1 and 6. In graphic A of Figure 4.7, the new airfoil of the tip section presents better results for high lift coefficients values, while in graphic B, only exhibits a better performance after an α = 6 with a peak absolute difference of 0.09 of the Piggott airfoil (7.3 %). For the second blade section, the aerodynamic efficiency of the new airfoil does not present large improvements except for a slight offset after a lift coefficient of

0.5 (graphic C). In graphic D, the only improvement of the modified airfoil is a tiny higher lift coefficient peak. The graphics regarding blade section 3 also do not present any significant improvements. In graphic E, the new airfoil stands worse than the Piggott airfoil for high lift coefficient values. With respect to the lift coefficient performance over the AoA, in graphic F, the new airfoil curve stands most of the AoA range exactly as the Piggott one, except around an AoA of 12, where the new airfoil exhibits a slightly lower lift coefficient peak for the same AoA (1 %).

The remaining sections of blade 3 are presented in Figure 4.8. The new airfoil of section 4 stands better from a lift coefficient of 0.15 to 0.4 where after, it has a worse behaviour up to

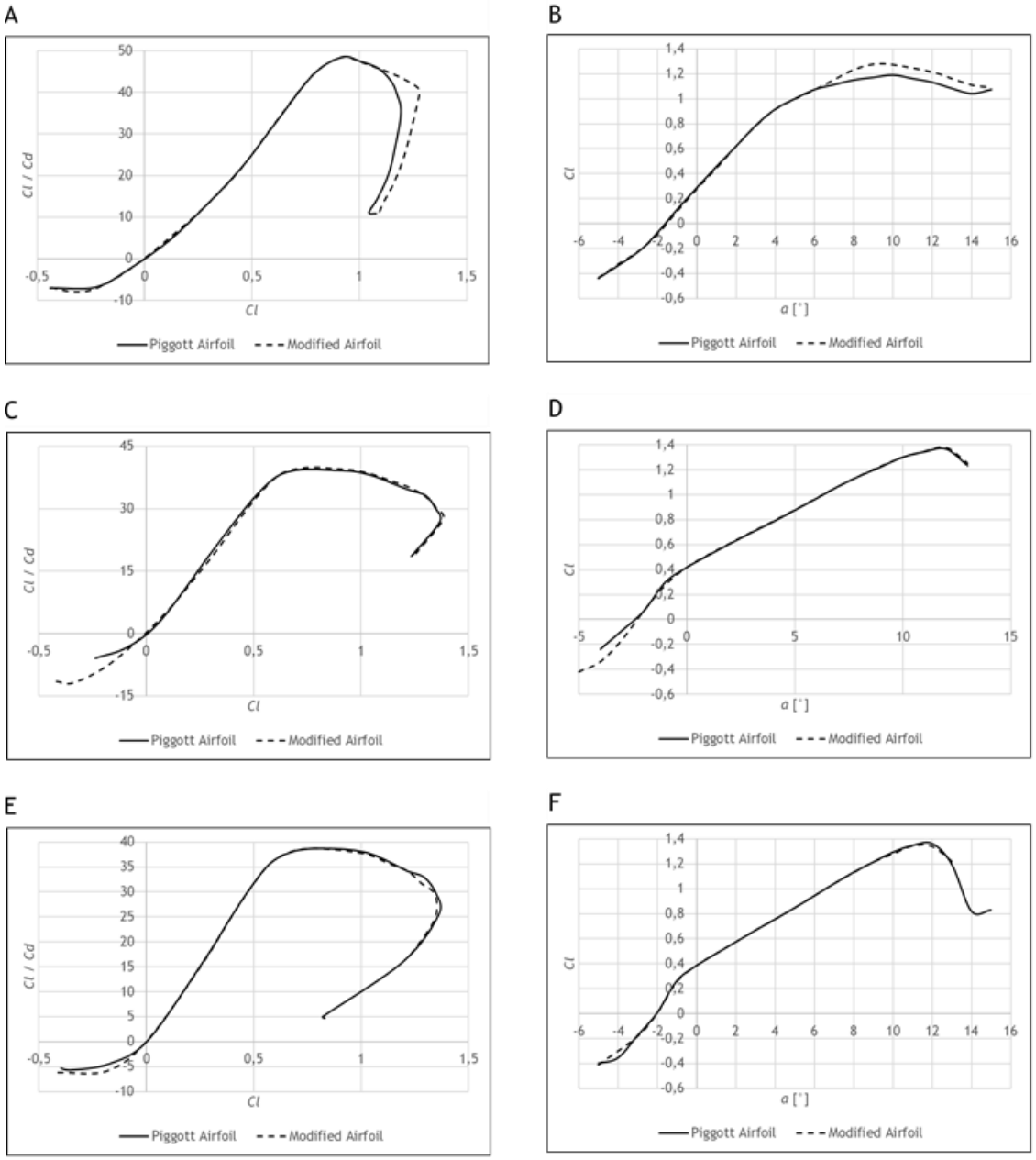

Figure 4.7: Aerodynamic efficiency and lift coefficient comparison between the Piggott and the modified airfoils of blade 3 (A,B: Section 1; C,D: Section 2; E,F: Section 3).

the peak. From the peak forward both airfoils behave similarly. As for graphic B, no improvements of the modified airfoil are observed. In graphic C, the new airfoil of section 5 has an improved aerodynamic efficiency from the origin until a lift coefficient of 0.4. From this point forward, the new airfoil presents a slight better performance as it reaches the maximum lift coefficient value, shifting to a worse performance until passing again through a lift coefficient value of 1. No significant differences are seen in graphic D, of the new airfoil compared to the Piggott one. Nevertheless, the modified airfoil presents a slightly lower, with an absolute difference of 0.02, peak than the original airfoil, as well as its performance is worse after the peak. As for the root section 6, of blade 3, the differences are noteworthy. In graphic E, the new airfoil simulation converged for more negative lift coefficient values than the Piggott

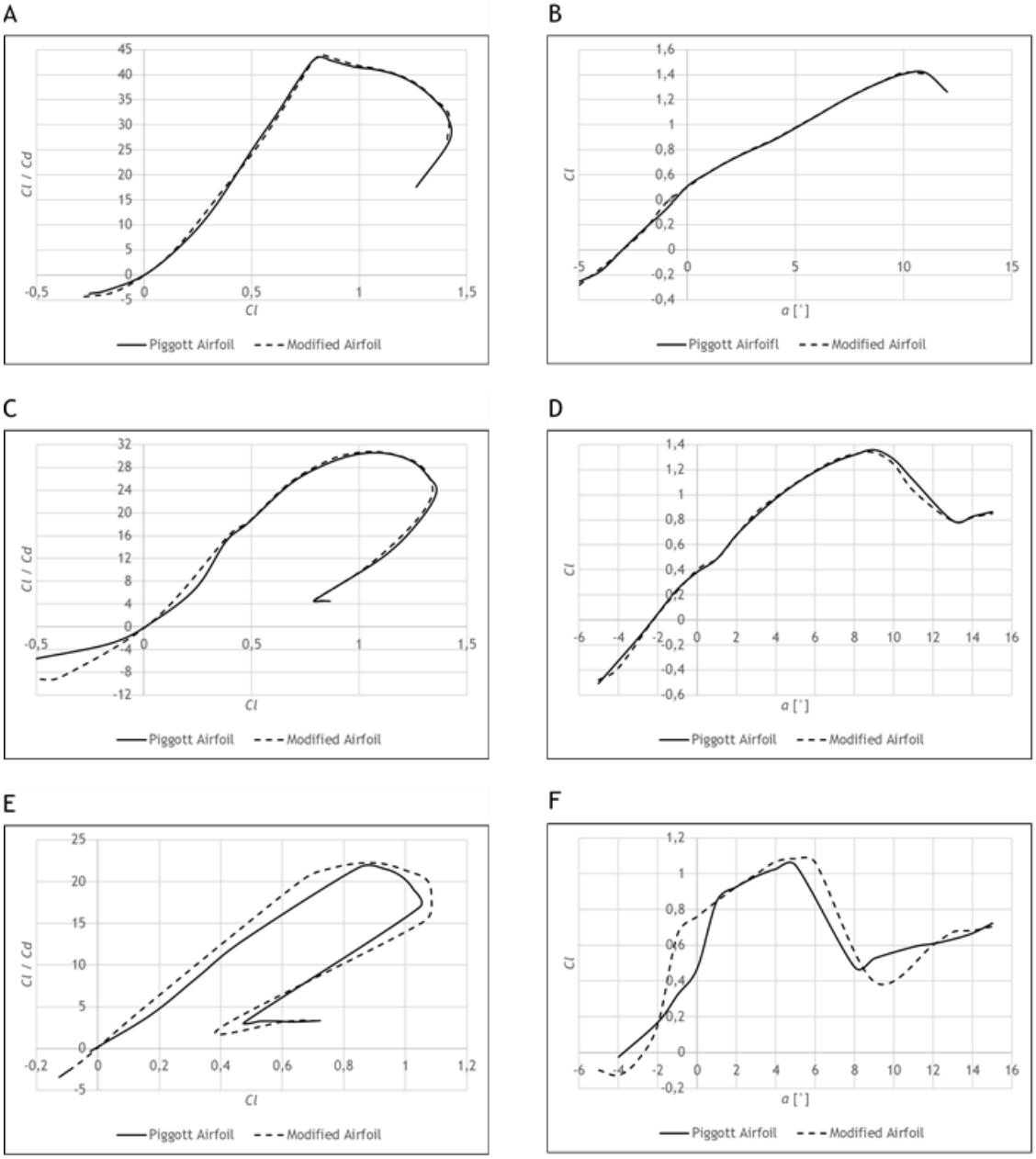

Figure 4.8: Aerodynamic efficiency and lift coefficient comparison between the Piggott and the modified airfoils of blade 3 (A,B: Section 4; C,D: Section 5; E,F: Section 6).

one. The new airfoil presents better performance from the origin of the graphic, going all the way to close of the curve peak at a lift coefficient of 0.9, where it presents an absolute difference of 2.7 for a lift coefficient of 0.65, that corresponds to an increase of 15.7 %. The region ranging from 0.7 and 1 is characterized by what could be a wide maximum aerodynamic efficiency region. On the lower part of the new airfoil curve, the Piggott airfoil has better performance after a lift coefficient of 0.7. In graphic F of Figure 4.8, the modified airfoil presents an exponential rise of the lift coefficient up to an AoA of about -1, followed by a smoother rise until an AoA of 2, where both airfoils curves closely match. For an α = 0 °, the modified airfoil presents an absolute difference of 0.29 from the Piggott airfoil, resulting in a performance increase of 61 %. From an AoA of 2, the new airfoil also stands better than the Piggott one, up to around an AoA of 8. At an α = 5 °, the modified airfoil exhibits a 3.6 % increase of its maximum lift coefficient value compared to the Piggott airfoil peak. Both airfoils show a recovery after their lift coefficient fall, where the Piggott one stands better initally, being overcome by the new airfoil after an AoA of 12.

Overall, the intent of modifying the original blade sections for a better airfoil performance at lower lift coefficients was achieved. It is expected that these improvements impact the new wind turbine performance with higher power coefficients at higher tip speed ratios.

4.4 BEM simulations

4.4.1 Blade 1

Figure 4.9 illustrates the BEM simulations performed as described in Subchapter 3.4 for the ideal rotor of blade 1 with the Piggott airfoils and with the modified airfoils for the 6 windspeeds considered. The Piggott rotor performance curve is presented as the solid line and the dashed line corresponds to the rotor with the modified airfoils. The new airfoils rotor is immediately characterized for the better power coefficient performance for high λ for all windspeeds as intended through the airfoils modifications. Graphic A, corresponding to the 3.0 m/s windspeed rotor simulation, shows a new rotor with practically the same power coefficient peak value but for a higher λ = 5.375, meaning that the power peak happens at a higher rotor rotational speed. For λ below the power peak, the fall due to the airfoil behaviour for high AoA, is more accentuated for the new rotor curve than for the Piggott rotor. At extreme lower λ values, the new rotor performs better than the Piggott rotor between the lowest λ and λ = 4. The second windspeed that was simulated, 3.7 m/s, is illustrated in graphic B. In a decreasing λ order, the new rotor shows better performance for most of the high λ region up to the power peak, except around a λ = 6 where both rotors present the same power coefficient. The new rotor presents a power peak of C_p = 0.339 for a λ = 4.75 while the Piggott peak of C_p = 0.33 occurs at a λ = 4.875, meaning a power coefficiet increase of 2 %. The new rotor shows better performance during its deep fall after the power peak, but the Piggott rotor overcomes it

between a λ = 4.5 and λ = 3, having then both rotors, about the same performance for the lowest λ. In graphic C, the 4.4 m/s windspeed simulation presents as well, the superior performance of the new rotor for high λ. With the same power peak, the new rotor has also better power coefficient performance for all the region left of the power peak than the Piggott rotor. Both rotors exhibit the same performance between the power peak and a λ = 6. The 5.5 m/s windspeed simulation, illustrated by graphic D, shows that the new rotor has a negative offset of the Piggott rotor curve for the left region of the power peak. In this case, the new rotor exhibits a lower power coefficient peak than the Piggott rotor, 1.3 % less, occurring both peaks for a λ = 4 . Between the power peak and λ = 6, both rotors have the same performance, where the new rotor has a better power coefficient curve from λ = 6 up to the highest λ value,

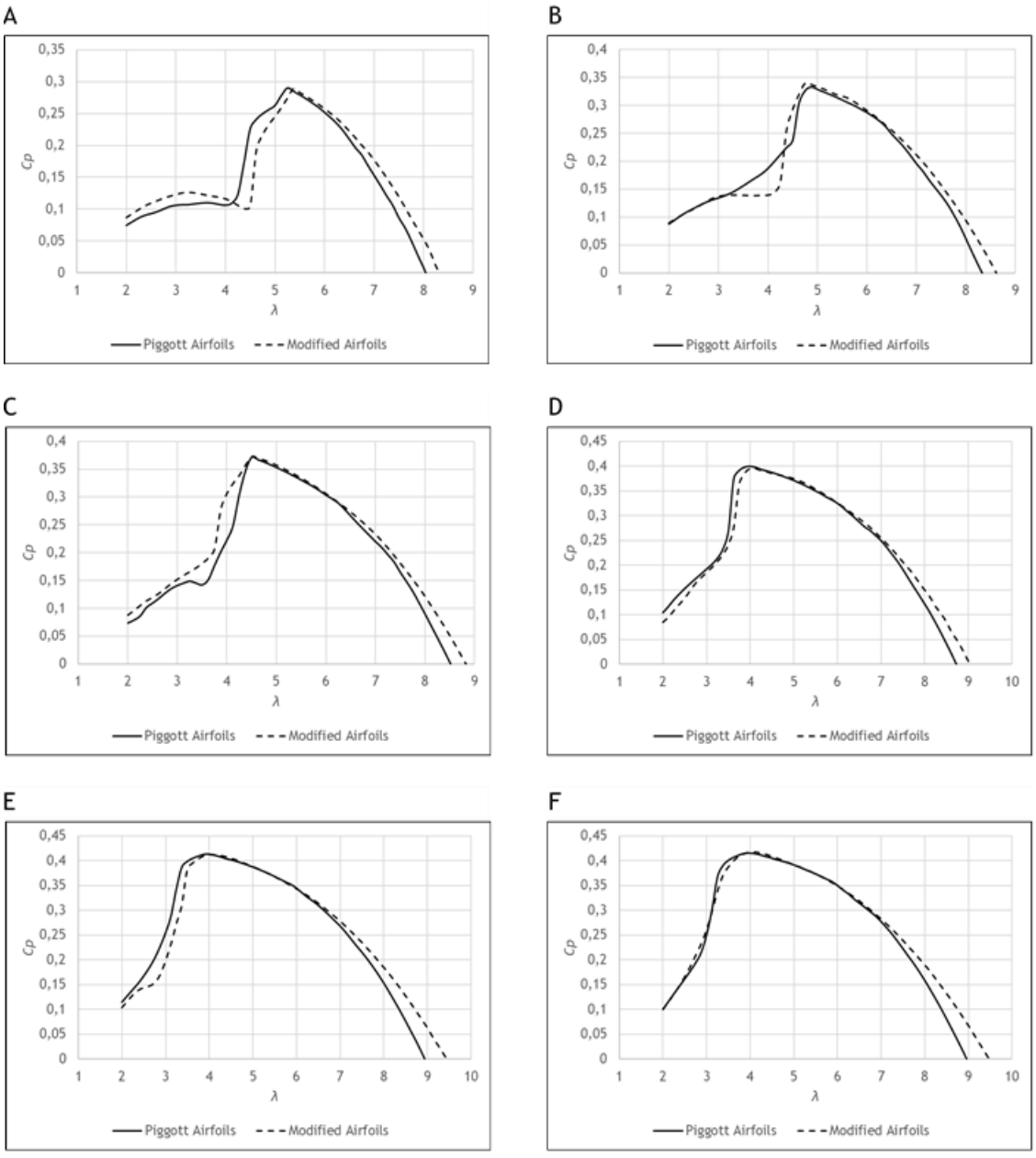

Figure 4.9: Piggott and modified rotor power coefficient comparison of blade 1 (A: 3.0 m/s; B: 3.7 m/s; C: 4.4 m/s; D: 5.5 m/s; E: 7.2 m/s; F: 7.7 m/s).

meaning that a better power coefficient for high rotor rotational speeds is achieved. With the same power coefficient peak, the new rotor regarding the 7.2 m/s windspeed simulation (graphic E), presents a drop in performance between the lowest λ and λ = 4, corresponding to the power peak λ. Both rotors exhibit close performance from the power peak to λ = 6.5. From this point forward, the new rotor has significant better performance. For the last windspeed simulation, 7.7 m/s, in graphic F, the same behaviour to the right region of the power peak as in the 7.2 m/s graphic is observed, where both rotors present equal performance between the power peak and λ = 7. The new rotor curve presents a superior power coefficient for the highest λ range. As for the left region of the power peak, the modified rotor stands worse between the power peak and λ = 3, being slightly better between the previous value and λ = 2.5, having then the same behaviour as the Piggott rotor below a λ = 2.5.

4.4.2 Blade 2

Figure 4.10 illustrates the simulations performed for the ideal rotor of blade 2 with the Piggott Airfoils and the modified airfoils. In graphic A, corresponding to the 3.0 m/s windspeed simulation, the modified rotor presents less power coefficient performance from the lowest λ up to λ = 7, where from this point onward, the modified rotor curve slightly exceeds the Piggott rotor curve. The ideal rotor with the new airfoils exhibits a lower power coefficient peak for the same λ = 4.125 (2.9 %). Observing graphic B, of the 3.7 m/s windspeed simulation, there are minimal differences between both rotor curves to the left region of the power peak. The modified rotor exhibits a higher power coefficient peak than the Piggott rotor for the same λ = 4.125 (3.1 %). Between λ = 3.5 and λ = 5, the modified rotor shows better power coefficient curve but after λ =5, it presents worse performance than the Piggott one until λ = 6. From this point up to λ = 7.5, both rotors have the same performance, but then the modified rotor presents a better power coefficient performance from λ = 7.5 up to the highest λ value. The analysis of the 4.4 m/s windspeed simulation from graphic C, is easily divided into 3 points. The modified rotor has the same power coefficient performance for the lowest λ values, being then inferior than the Piggott rotor as λ increases up to the power peak. Also, the modified rotor exhibits a marginal inferior power peak, with an absolute difference of 0.003, for the same λ of the Piggott rotor. The second point reflects the equal behaviour of both rotors from the power peak until λ = 7.5. The last point is about how the modified rotor has better performance than the Piggott rotor, from λ = 7.5 until the highest λ value. The modified rotor curve of the 5.5 m/s windspeed simulation (graphic D,) shows that it begins with a better power coefficient for the lowest λ values, having then a slight inferior curve than the Piggott one up to the power peak. The modified rotor presents an earlier 2 % increased power peak (λ =4.125) than the Piggott rotor peak for a λ = 4.25. In this windspeed simulation, the widening of the high λ region where the modified rotor curve is superior than the Piggott one, is clear from λ = 7 up to the highest λ value. Between the power peak and λ = 7, both rotors yield the same power coefficient. The logic made to the analysis of graphic C, is in some extent almost valid

to graphic E. Corresponding to the 7.2 m/s windspeed simulation, the high λ region where the modified rotor curve is superior to the Piggott one, from λ = 6.5 up to the highest λ value, spreads even more. Not only its width increases, but also the power coefficient difference is greater than the one observed in graphic D. For a λ = 9.125, the modified rotor presents a C_p = 0.071 while the Piggott has a C_p = 0.0096, meaning an increase of 641 %. As the λ decreases, both rotors present the same power coefficient up to the power peak, where for a λ = 4.375, the new rotor power peak has an increase of 0.78 %. The modified rotor presents an inferior performance from the power peak up to λ = 2. For the last simulation, concerning the 7.7 m/s windspeed, in graphic F the better performance of the modified rotor for high λ is also observed, after a λ = 6.5. Both rotors yield the same power coefficient between their power

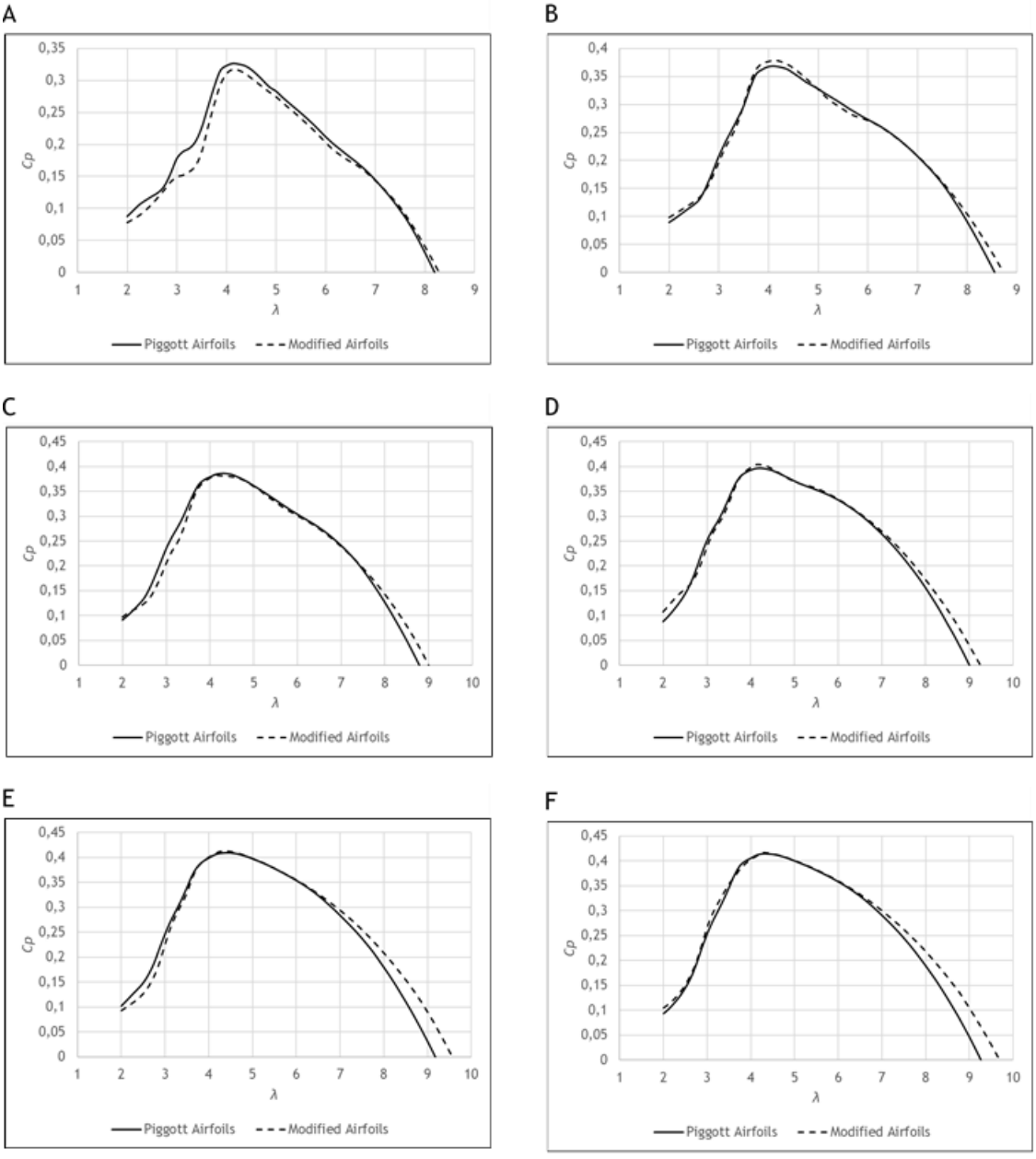

Figure 4.10: Piggott and modified rotor power coefficient comparison of blade 2(A: 3.0 m/s; B: 3.7 m/s; C: 4.4 m/s; D: 5.5 m/s; E: 7.2 m/s; F: 7.7 m/s).

peak, that is closely the same (0.28 % increase), until λ = 6.5. To the left region of the power peak, the modified rotor exhibits a marginal better performance than the Piggott rotor for most of the fall.

The simulations show again an improvement of the power coefficient at high λ as seen in Subchapter 4.4.2. Nevertheless, in this case, the improvements at high λ are marginal for the 3.0 and 3.7 m/s windspeed simulations. The behaviour observed in the lower λ region of both rotors is smoother than the behaviour regarding those of blade 1 in the same interval. Also, except for the 3.0 and 4.4 m/s windspeed simulations, the offset of the modified rotor performance on the left region of the power peak is marginal compared to the Piggott curve.

4.4.3 Blade 3

The BEM simulations of the ideal rotor of three identical blades 3 with the Piggott airfoils and with the new airfoils are portrayed in Figure 4.11. In graphic A, regarding the 3.0 m/s windspeed simulation, the modified rotor has an inferior performance than the Piggott rotor between λ = 5 and the highest λ value, although the new rotor presents a slightly higher power coefficient peak (2%) for a lower λ = 4.625 than the λ = 5 corresponding to the Piggott peak. As the λ decreases, practically both rotors yield the same power coefficient from the power peak up to the lowest λ. The second simulation concerning the 3.7 m/s windspeed, graphic B, presents a modified rotor with a maximum power coefficient of C_p = 0.372 at λ = 4.875, being inferior than the Piggott rotor maximum power coefficient of C_p = 0.387that occurs at λ = 4.375. Both rotors have the same curve from λ = 5 and λ = 6.5, but the Piggott rotor shows better performance compared to the modified rotor after λ = 6.5 up to the highest λ value. From the extreme lowest λ, both rotors present the same power coefficient performance up to λ = 3.5 but after, the modified rotor presents worse performance up to λ = 5, with a decrease of 28.4 % for a λ = 4. Graphic C, of the 4.4 m/s windspeed simulation, portraits both rotors with the same power coefficient between λ = 4 and λ = 7. From λ = 7 up to the highest λ value, the modified rotor has a marginal worse performance than the Piggott rotor. As for the lowest λ value, the modified rotor presents worse performance, but it overcomes the Piggott rotor after a λ = 2.5, having a significant difference that decreases as reaching λ = 4. At a λ = 3.375 there is a 30.4 % increase of the new rotor performance. Both rotors exhibit the same power coefficient peak, with an absolute difference of 0.001, for the same λ = 4.375. The results regarding the 5.5 m/s windspeed simulation are displayed in graphic D and, both rotors show practically the same performance from λ = 4 up to the highest λ value. From the lowest λ value until λ = 2.5, the new rotor presents a marginal better performance but then, it shows a significant worse behaviour up to λ = 4.The modified rotor exhibits its slightly inferior power peak with an absolute difference of 0.006 at λ =4.25, the same λ corresponding to the Piggott rotor maximum power coefficient. Analysing graphic E, corresponding to the 7.2 m/s windspeed

simulation, shows that both rotors yield the same power coefficient for the high λ region, between λ = 8 and the highest λ value. From λ = 3.5 until λ = 8 the new rotor presents a slightly better performance and exhibits a higher power peak than the Piggott rotor for λ = 4.25 (1.82 %). Below a λ = 3.5, the new rotor shows a marginal worse performance until λ = 2.5, where after and up to the lowest λ value, it presents the same performance as the Piggott rotor. The last windspeed simulation 7.7 m/s, displayed in graphic F, shows that the modified rotor presents a worse power coefficient behaviour than the Piggott rotor from the lowest λ value up to λ = 3. After a λ = 3, the modified rotor performs slightly better than the Piggott rotor all the way up to the highest λ value. The new rotor yields a decreased maximum power coefficient (0.28 %) for a λ = 4.25, whereas the Piggott power peak happens for λ =4.375.

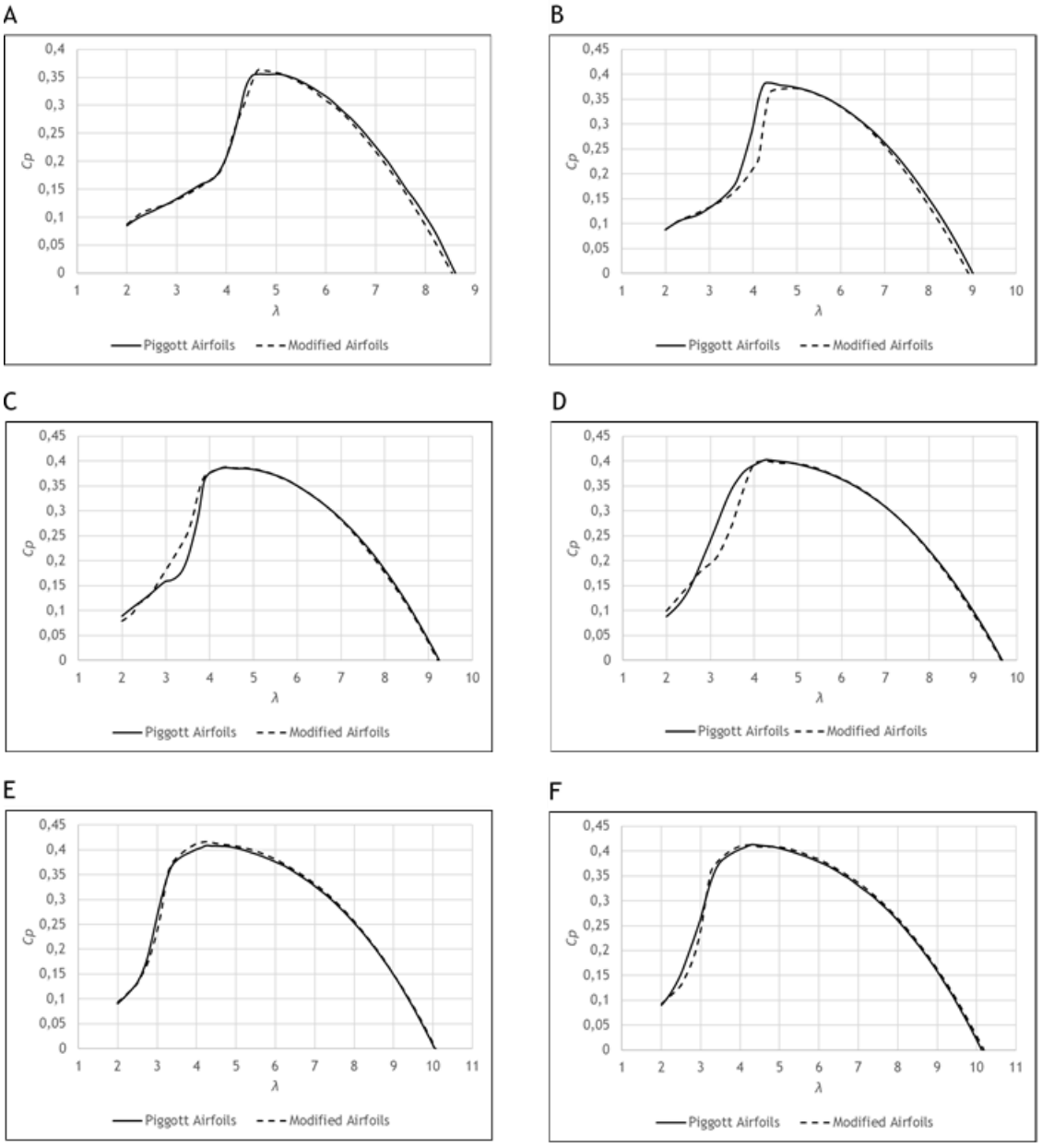

Figure 4.11: Piggott and modified rotor power coefficient comparison of blade 3 (A: 3.0 m/s; B: 3.7 m/s; C: 4.4 m/s; D: 5.5 m/s; E: 7.2 m/s; F: 7.7 m/s).

Unlike the results from Subchapter 4.4.1 and 4.4.2, the modified rotor does not present significant better performance for the highest λ when compared to the Piggott rotor performance. Instead, both rotors closely yield the same power coefficient for the highest λ values, except for the two lowest windspeeds (graphic A and B), where the modified rotor presents worse performance than the Piggott rotor. As observed in Subchapter 4.4.2, the left region of the power peak present both rotors with a smooth behaviour, where the simulations regarding the 3.0, 7.2 and 7.7 m/s present rotors that yield practically the same power coefficient but the same does not apply for the 3.7, 4.4 and 5.5 m/s simulations.

4.5 Modified Airfoils Rotor Performance

The real Piggott turbine (with an average of the 3 different blades performance) and the average of the 3 ideal modified rotors are displayed by Figure 4.12, with 6 graphics corresponding each to a windspeed. This average allows to approximate the behaviour of the real turbine. The first windspeed concerning the 3.0 m/s simulation, graphic A, shows that the modified turbine does not behave much differently from the Piggott turbine except between λ = 4 and λ = 5.5. Both turbines present closely the same power coefficient from the lowest λ value up to λ = 4 but the Piggott rotor presents slightly better performance between λ = 3 and λ = 4. There is a large difference after λ = 4, where the Piggott turbine performs significantly better that the modified turbine. In this interval, the Piggott and the modified turbine present a somehow constant curve regarding the maximum power coefficient values they achieve, whereas the modified turbine exhibits an inferior power peak (2.7 %) as well as a narrower maximum power coefficient curve. Between a λ = 5.5 and λ = 6.5, the modified turbine presents a marginal worse performance but afterwards, the opposite is observed, where the modified turbine presents better performance than the Piggott turbine up to the highest λ value. As for graphic B, of the 3.7 m/s windspeed simulation, there are two regions where both rotors yield the same power coefficient: between λ = 2 and λ = 3, and a λ = 5 and λ = 7. From the power peak and in a decreasing λ order, the modified turbine exhibits a curve where it falls below the original turbine, stalling more abruptly. The modified rotor presents a slightly better power peak than the original rotor (1.5 %) for the same λ = 4.75. Again, for the 3.7 m/s windspeed simulation, the modified rotor presents better performance than the Piggott turbine for the highest λ values. For the 4.4 m/s windspeed results, graphic C, both rotors have the same performance from the lowest λ up to λ = 3, where after and up to the power peak, the modified rotor shows better performance than the Piggott rotor. For a λ = 4, the new turbine exhibits an increased performance of 8.4 %. For a λ = 4.5, the new turbine presents a 0.1 % decrease in the maximum C_p compared to the Piggott turbine peak, and from this power peak up to λ = 7, they display the same performance, where afterwards, the modified rotor surpasses the Piggott rotor up to the highest λ value. Graphic D, corresponding to the 5.5 m/s windspeed results, shows that once again, the modified rotor performs better than the Piggott one for high λ values,

particularly after λ = 7. Between this value and the power peak, both rotors yield the same power coefficient as well as both achieve closely the same maximum power coefficient with an absolute difference of 0.002 around a λ = 4.2, meaning in a 0.5 % increase of the new rotor peak. In a decreasing λ manner, after the power peak, the Piggott rotor displays superior performance than the modified rotor curve up to λ = 3, while they have the same power coefficient from this point until the lowest λ value. The analysis done to graphic D, could be shared as the analysis to be applied for graphic E, of the 7.2 m/s windspeed simulations. These results display three different regions: one where the Piggott rotor performs better than the modified rotor from λ =2 to λ = 3.5; another region where both rotors have the same power coefficient curve , that is between λ = 3.5 and λ = 6; and the last region, where the modified

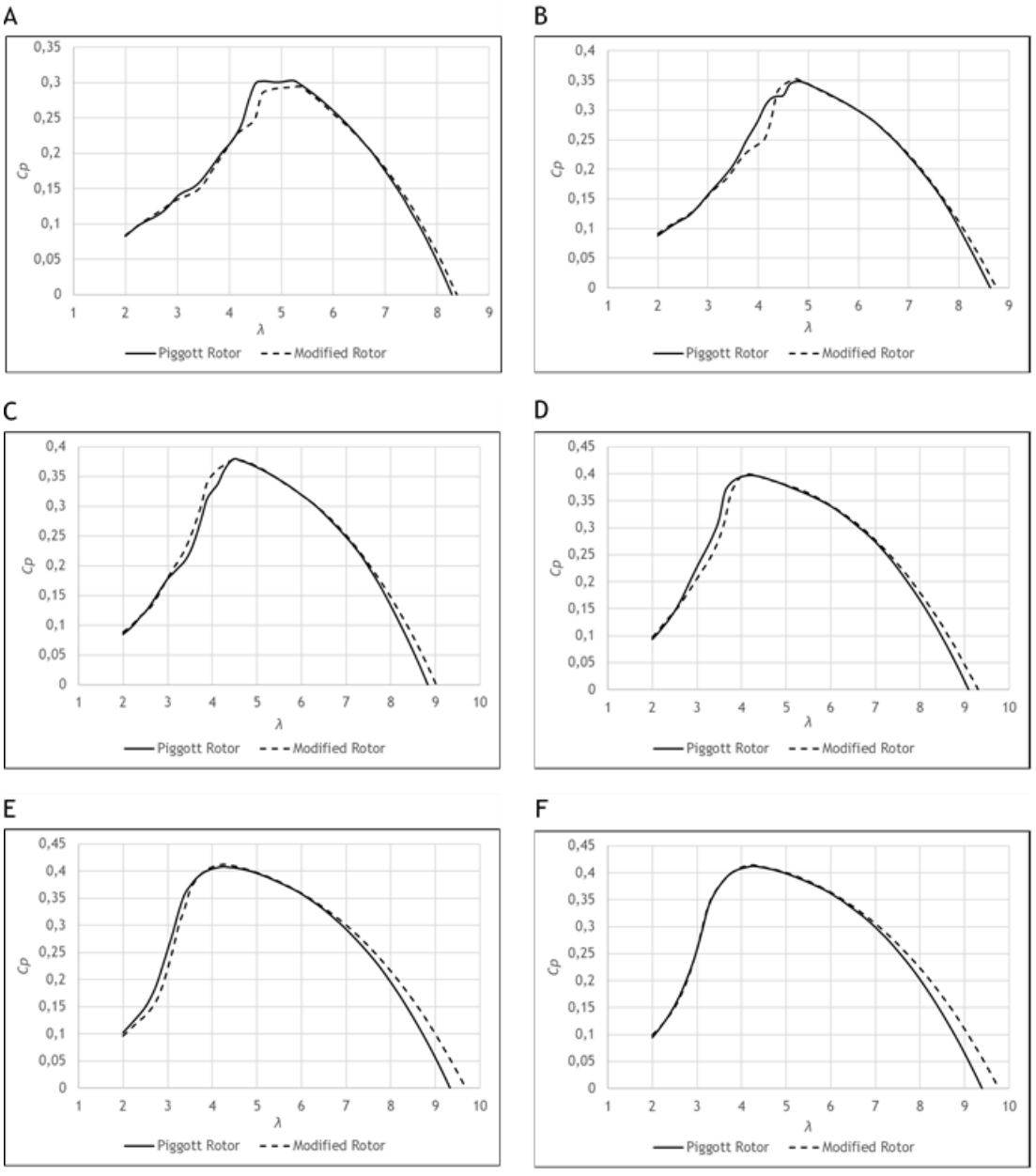

Figure 4.12: Power coefficient comparison between the average of the 3 Piggott and the 3 modified rotors (A: 3.0 m/s; B: 3.7 m/s; C: 4.4 m/s; D: 5.5 m/s; E: 7.2 m/s; F: 7.7 m/s).

rotor presents better performance than the Piggott rotor in the highest λ range, specifically after λ = 6 and up to the highest λ value. The modified rotor exhibits a slightly better maximum power coefficient (1.1 %) than the Piggott rotor, both peaks for a λ = 4.25. The results of the highest windspeed simulation, 7.7 m/s, that are illustrated by graphic F, show clearly two regions. One where both rotors yield the same power coefficient between the lowest λ and λ = 6, and another region where the modified rotor slightly starts to show an improved power coefficient after λ = 6, that is significantly better after λ = 8 up to the highest λ value. Nevertheless, the modified rotor presents a marginal better power peak (C_p = 0.415) than the Piggott rotor (0.42 % higher), for a λ = 4.25.

4.6 Rotor Power Output

Figure 4.13 illustrates the maximum power coefficient that each rotor achieves for each windspeed and the corresponding λ. These results correspond to those of Subchapter 4.5 regarding the average of the 3 ideal rotors. The λ values that stand above the curves refer to the Piggott rotor and the ones that are displayed below the curves denote the modified rotor. As said in the analysis of the previous section, the results of the 3.0 m/s windspeed presented a modified rotor with an inferior maximum power coefficient than the Piggott rotor. Nevertheless, the Piggott rotor power peak occurs at a λ = 5.25, lower than the modified rotor power peak. As for the 3.7 m/s windspeed, both power peaks occur at a λ =4.75, but the

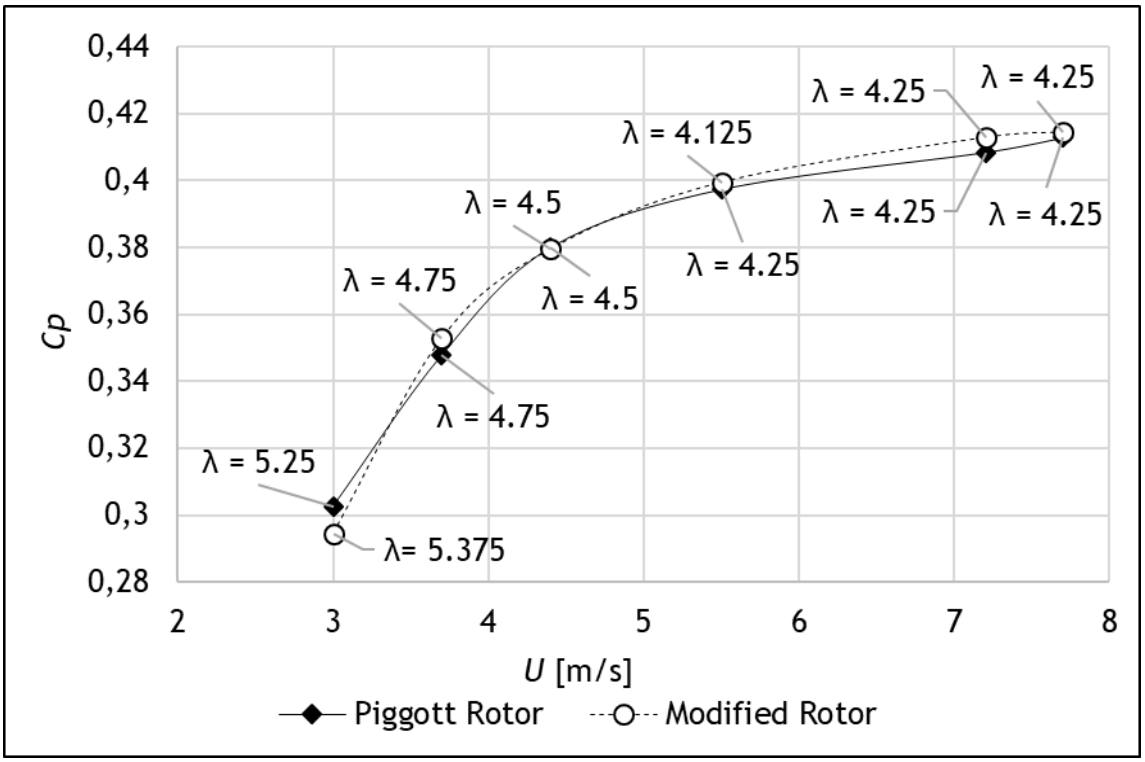

Figure 4.13: Maximum power coefficient and corresponding optimum λ of the averaged Piggott and modified rotor.

modified rotor power peak (C_p = 0.353) is higher than the Piggott rotor peak of C_p = 0.348 (1.47 % increase), meaning that for the same rotational speed in this windspeed, the modified rotor extracts more power from the available power in the considered wind. Both rotors present the same maximum power coefficient, with an absolute difference of 0.0004, for the same λ regarding the 4.4 m/s windspeed. For the 5.5 m/s windspeed, the modified rotor achieves a better maximum C_p = 0.399 for a λ =4.125, meaning at a lower rotational speed, than the Piggott rotor power peak of C_p = 0.397 (λ = 4.25). As for the 7.2 windspeed power peaks, the modified rotor presents a better peak (C_p = 0.413) than the Piggott rotor maximum C_p = 0.408 (1.1 % increase), but both occur for a λ = 4.25. The power peaks about the last windspeed, 7.7 m/s, also occur for the same λ, but the modified rotor peak is slightly better than the Piggott one (0.42 %). The design λ of the Piggott rotor was of λ = 5, and the rotor would achieve the best performance in this value. The results from Figure 4.13 do not present power peaks of the Piggott rotor exactly at a λ = 5 but very close to it, and the trend is a decrease of the λ at which the power peak occurs with the increase of the windspeed, stagnating at a λ = 4.25 for the 3 highest windspeeds. The airfoils modification turned out to present a lower power peak for the lowest windspeed, meaning that the modified rotor would have to operate at a higher rotational speed than the Piggott rotor to reach its maximum power coefficient. Taking in consideration the equal power peak for the 4.4 m/s windspeed, the modified rotor presents a better power peak for the 5.5, 7.2 and 7.7 m/s windspeed. The trend about the decrease of the λ corresponding to the power peak with the increase of the windspeed, also applies to the modified rotor but only until the 5.5 m/s windspeed which λ = 4.125, as the 7.2 and 7.7 m/s windspeed power peaks happen at a λ = 4.5.

As described in Subchapter 3.5, with the data of the averaged Piggott and the averaged modified rotor, the power the rotors would extract from the available power in the considered wind was calculated. Table 3.3 displays the results for the 3.0 m/s windspeed data, that are portrayed in Figure 4.14. The modified rotor extracts more power than the Piggott rotor for higher rotational speeds (higher λ), that is in accordance with the $C_p - \lambda$ graphic A of Figure 4.12, where the modified rotor C_p is better at higher λ than the Piggott rotor. The same procedure was done to the remaining windspeeds, whose tables and graphics are shown in Appendix B. These tables presenting the rotors power output were selected to show only the logical ω values. The data collected from the simulations, range from a λ = 2 to λ = 11 and there are ω which the respective λ is lower than 2, thus not being possible to apply Equation 3.1 for the interpolation. Also, and not taking in account the graphics of Subchapter 4.1, all the $C_p - \lambda$ graphics displayed were presented up to the λ which corresponds to a power coefficient of zero. The rotational speeds which λ are beyond this point, have a negative power coefficient. Taking as an example Figure 4.14, to the rotational speed of 450 RPM corresponds a λ within the values to perform the interpolation, but both rotors C_p is negative and yield a negative rotor power, and it would not be logical to present rotors with negative power.

Nevertheless, the cases of the 5.5 m/s and the 7.2 m/s windspeed rotor power output (see Appendix B), present a situation where the Piggott rotor yields negative power for the highest ω considered but the modified rotor yields positive power.

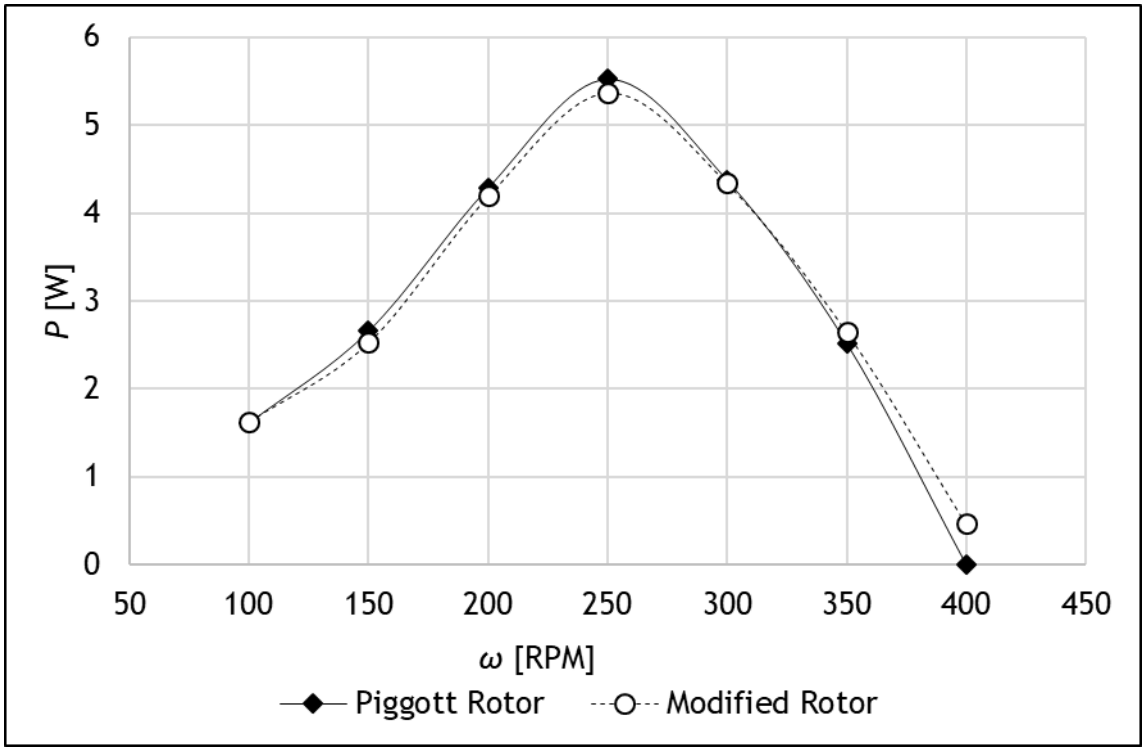

Figure 4.14: Averaged Piggott and modified rotor power for the 3.0 m/s windspeed.

In Figure 4.15, the power of the averaged modified rotor for a set of ω is displayed. This graphic shows that for each set of ω, more power is achieved with the increase of the windspeed. As predicted by the One-Dimensional Momentum Theory with Wake Rotation, the increase of ω also leads to more power as seen by the shift of the curves but, in this case, only until 500 RPM when maximum power is reached for a windspeed of 7.7 m/s. By increasing ω onward, the rotor power decreases, and the rotor would only work for high windspeeds.

With the analysis from Figure 4.15, a power comparison between both rotors was performed, by setting a hypothetical scenario where the rotors would function at a constant ω = 500 RPM. Table 4.1 presents the power values of both rotors for the considered ω, and Figure 4.16 displays graphically their performance. The Y axis is plotted with a logarithmic scale for better visualization purposes as the power values for higher windspeeds are different by one percent or less. The power of both rotors for the lowest windspeed is not presented because the considered ω yields negative power as deduced from Figure 4.14. For this hypothetical scenario of a constant ω = 500 RPM, there is a significant better performance of the modified turbine for the 3.7 m/s windspeed that reflects an increase of 87 % of the power extracted compared to the Piggott rotor, and a minimal improvement for the remaining windspeeds less than 2 %. It may be concluded that the energy production of both turbines will be essentially the same

and the main difference between the modified turbine and the original Piggott turbine is that in low wind conditions, the former may not stop where the later will stand still.

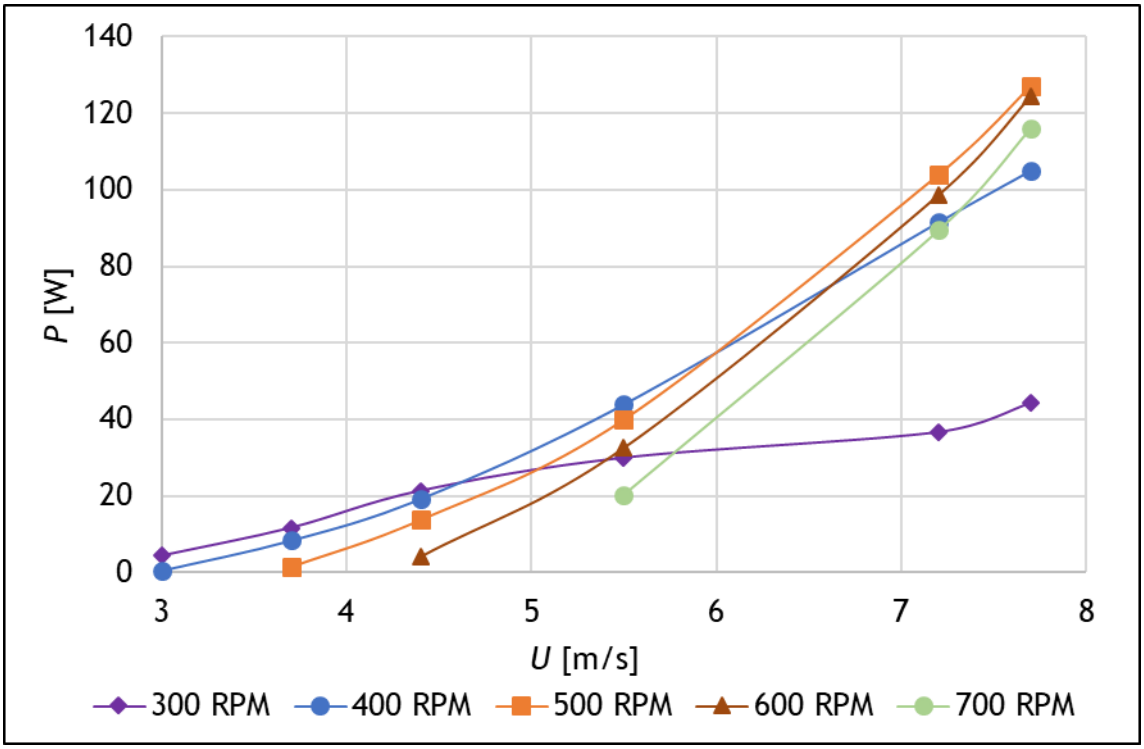

Figure 4.15: Averaged modified rotor power as function of ω.

Table 4.1: Averaged Piggott and modified rotor power for a rotational speed of 500 RPM.

	Piggott Rotor	Modified Rotor	Δ %
U [m/s]	P [W]	P [W]	
3.7	0.769	1.442	87.391
4.4	13.609	13.769	1.180
5.5	39.744	40.030	0.718
7.2	102.847	104.041	1.160
7.7	126.625	127.205	0.459

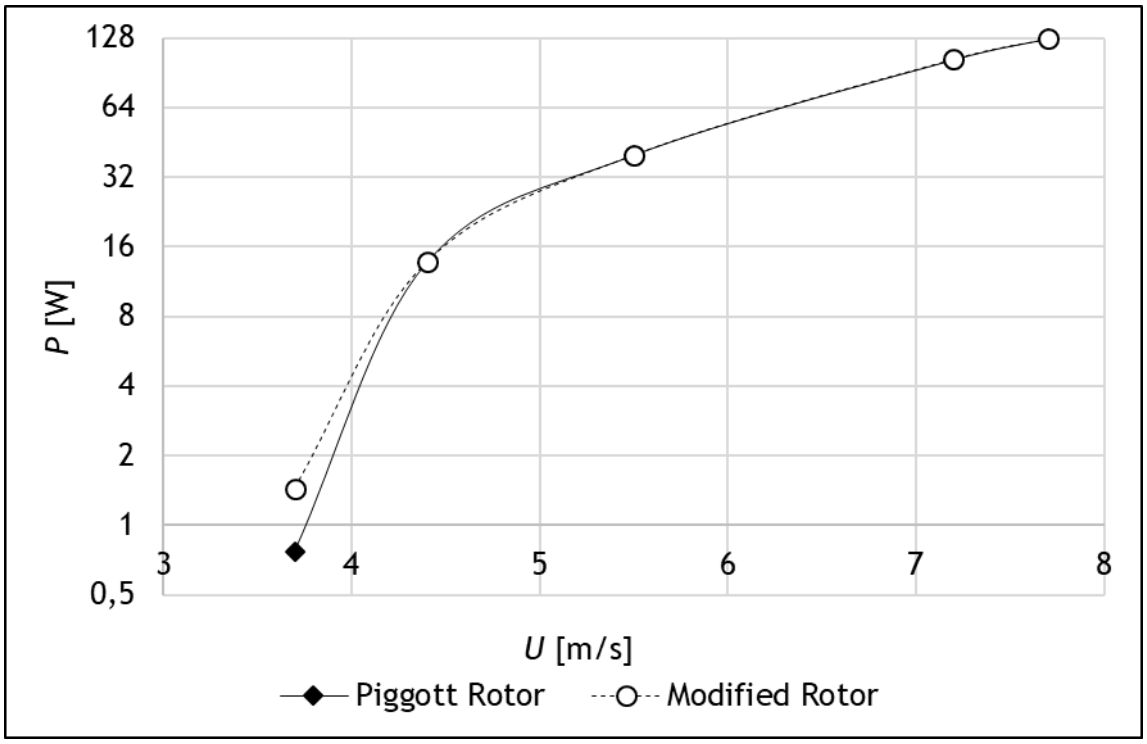

Figure 4.16: Averaged Piggott and modified rotor power for a rotational speed of 500 RPM (Y-axis shown with logarithmical scale).

4.7 Optimized Modified Airfoils Rotor Performance

As in Subchapter 4.3, where the new airfoil and the Piggott airfoil were compared, Figures 4.17 and 4.18 also display the aerodynamic efficiency and lift coefficient comparison between the three airfoils of the same blade section regarding the three different blades. For example, the section 1 airfoils of blade 1, 2 and 3 are compared in the same graphic, where the blade 1 airfoil is represented by the solid line, the blade 2 airfoil by the round dots line and the blade 3 airfoil by the squared dots line. Although there are two airfoils characteristics presented, the aerodynamic efficiency is the parameter chosen as the criteria for the best airfoil to selected among the three.

As for the airfoils of the blade tip section, graphic A and B of Figure 4.17, blade 2 and 3 present the best C_l/C_d values for low C_l values although for high C_l the best performance belongs to blade 1 and 3. The blade 1 airfoil exhibits a slightly higher and later peak than the blade 3 airfoil. Due to the overall good performance of blade 3, the best section 1 airfoil is therefore the blade 3 airfoil. For the blade airfoils of section 2, graphic C and D, the blade 1 C_l/C_d has clearly the worst performance for all the C_l range. Blade 3 presents the best performance after a C_l = 0.5, where after a C_l = 0.8, blade 2 exhibits a significant better performance with the best C_l/C_d peak, but is followed by a deep fall. Although from a C_l = 0.8 to C_l = 1.2 blade 2 has the best behaviour, blade 3 was chosen as the best airfoil of section 2 due to the achieved C_l/C_d for the highest C_l values. Graphic E, corresponding to blade section 3 C_l/C_d performance,

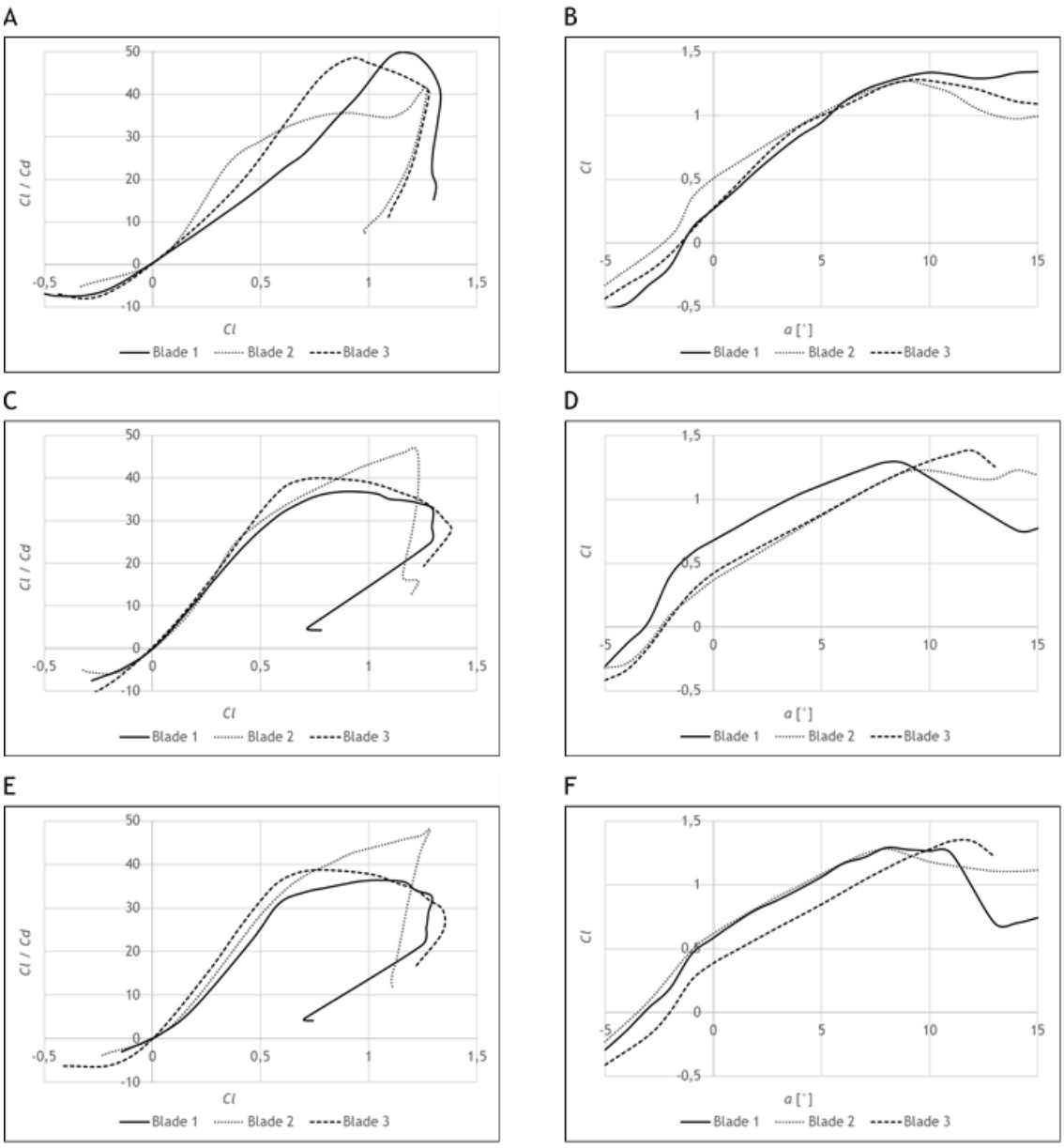

Figure 4.17: Modified airfoils aerodynamic efficiency and lift coefficient comparison between blade 1, 2 and 3 (A,B: Section 1; C,D: Section 2; E,F: Section 3).

shows that up to a C_l = 0.75, blade 3 presents the best behaviour, as well it has a total wider C_l range. The best performance after a C_l = 0.75 belongs to blade 2, where the best C_l/C_d is reached but it is followed by a deep fall, just as in graphic C. For this section 3, the blade 3 airfoil is again the selected among the three airfoils.

Regarding Figure 4.18, of the remaining blade sections, the blade 2 airfoil has the worst performance for the three considered blade sections. As so, the comparison is down between the blade 1 and blade 3 airfoil. Graphic A, corresponding to section 4, shows that the blade 3 airfoil has the highest C_l/C_d for a lower C_l than the blade 1 C_l/C_d peak. Nevertheless, only between a C_l = 0.7 and C_l = 1.1 that the blade 3 airfoil has a better performance than the blade 1 airfoil, thus being the blade 1 airfoil the pick for section 4. Observing graphic C that

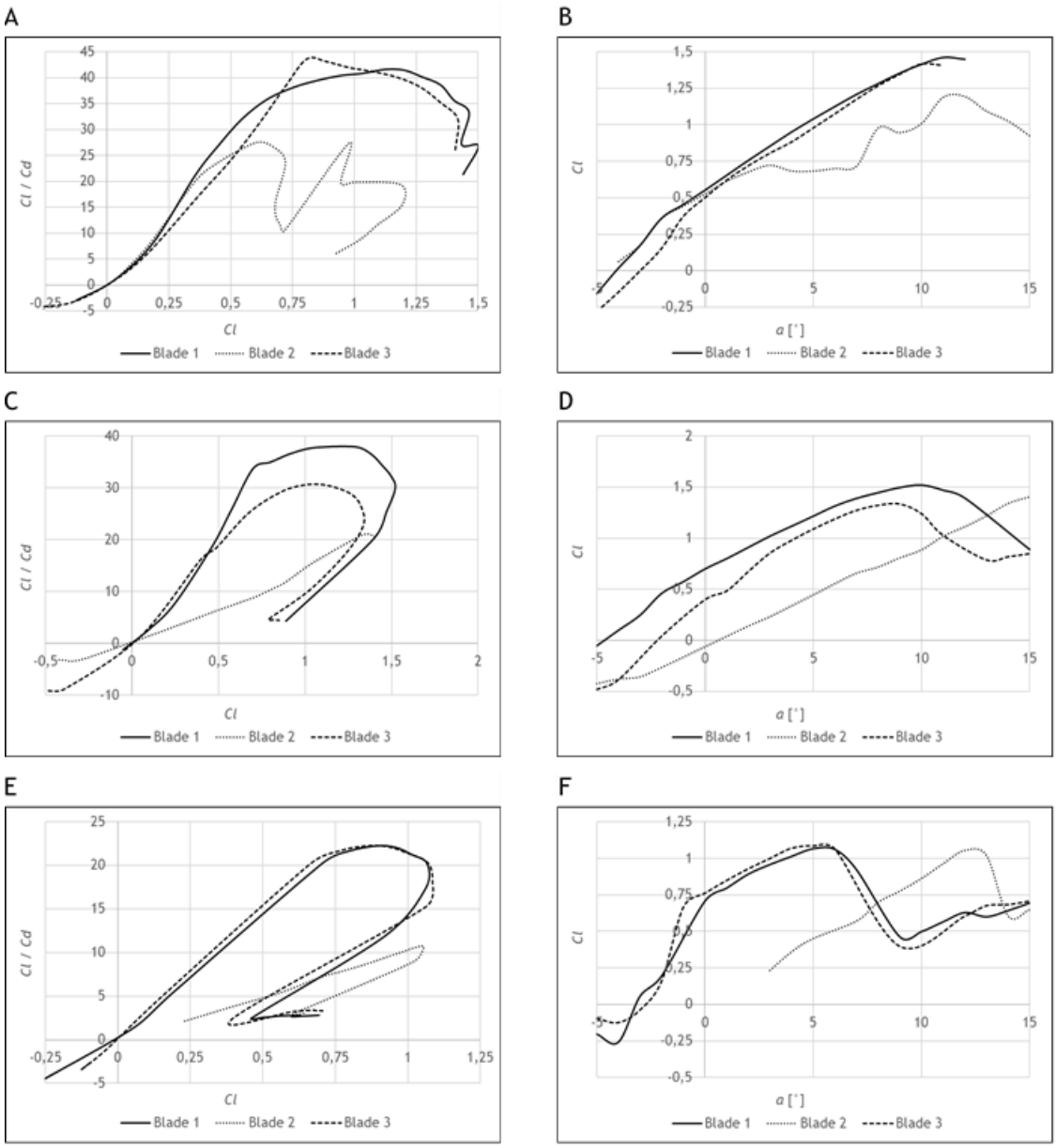

Figure 4.18: Modified airfoils aerodynamic efficiency and lift coefficient comparison between blade 1, 2 and 3 (A,B: Section 4; C,D: Section 5; E,F: Section 6).

corresponds to section 5, even though that blade 3 has a slightly better performance below C_l = 0.4, the blade 1 airfoil is undoubtedly the pick for section 5. As for the root section, in graphic E, the blade 3 airfoil has a positive C_l/C_d offset of the blade 1 airfoil between the origin and a C_l = 0.87. Both airfoils exhibit the same C_l/C_d peak and blade 3 performs better after a C_l = 1. Therefore, for this section 6, the selected airfoil is the blade 3 airfoil. Table 4.2 summarizes the selected airfoil for each blade section.

Table 4.2: Best airfoil for each blade section.

Blade section	1	2	3	4	5	6
Best airfoil	Blade 3	Blade 3	Blade 3	Blade 1	Blade 1	Blade 3

With the airfoils selected, the simulation of the optimized rotor was performed following the method from Subchapter 3.4. The BEM simulations results of the optimized rotor are illustrated in Figure 4.19 and compared to the results from Subchapter 4.5 of the averaged Piggott rotor. As for the lowest windspeed considered, 3.0 m/s, right away is observed a significant better performance of the optimized rotor from a λ = 4 up to the highest λ value. Only between a λ = 2.8 and λ = 3.8, the Piggott rotor has a better behaviour than the optimized rotor, and from the lowest λ up to λ = 2.8, the optimized rotor also exhibits better performance. The optimized rotor presents a maximum C_p = 0.352 for a λ = 4.875, that represents an increase of 16.2 % of the Piggott power peak that occurs for a higher λ = 5.25. At a λ = 8.25, there is an absolute C_p difference of 0.074 that translates in 1298 % increase of the optimized rotor. For the 3.7 m/s

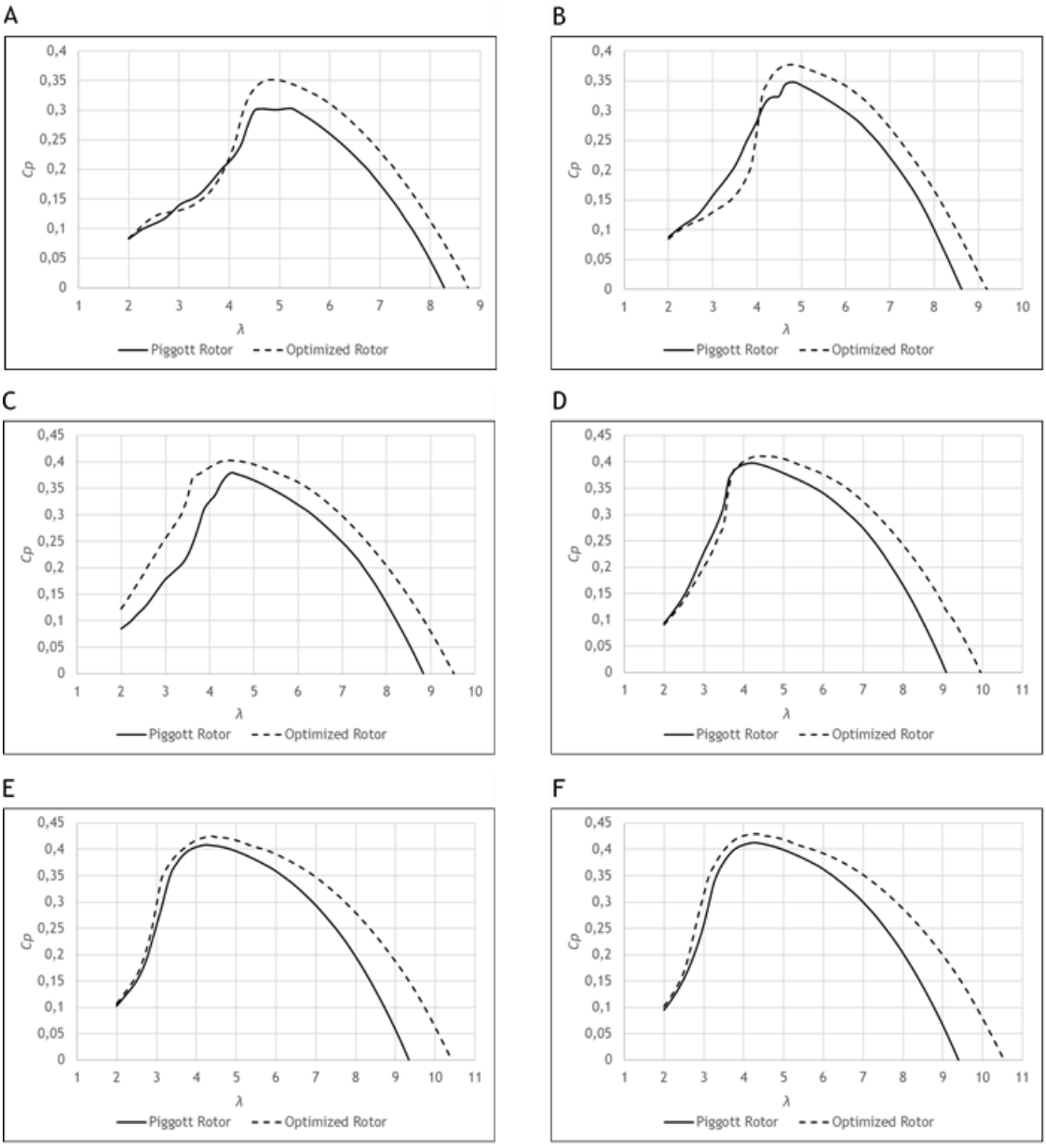

Figure 4.19: Power coefficient comparison between the averaged of the 3 Piggott rotors and the optimized rotor (A: 3.0 m/s; B: 3.7 m/s; C: 4.4 m/s; D: 5.5 m/s; E: 7.2 m/s; F: 7.7 m/s).

windspeed simulation, graphic B, the optimized rotor has a worse performance than the Piggott rotor from the lowest λ up to a λ = 4. There is a decrease of the optimized C_p at a λ = 3.75 of 24.6 %. Both rotors maximum C_p occur for a λ = 4.75, where the optimized rotor has an increase of 8.6 %. From a λ = 4 up to the highest λ value, the optimized rotor has a better behaviour than the Piggott rotor. Graphic C, of the 4.4 m/s windspeed simulation, displays an optimized rotor that is better than the Piggott rotor in all the λ range. There is a maximum increase of 50 % of the optimized C_p for a λ = 3.625. The Piggott rotor exhibits a maximum C_p = 0.38 at a λ = 4.5, whereas the optimized rotor presents a power peak of 0.403 for an earlier λ = 4.375, producing an increase of 6.1 %. The graphic concerning the 5.5 m/s windspeed simulation, D, is divided in two regions. One where the optimized rotor shows a better performance from λ = 3.75 up to the highest λ value, and another where its performance is worse than the Piggott rotor from the lowest λ value up to λ = 3.75. Even though the optimized rotor has a maximum C_p = 0.411 for a later λ = 4.375 than the Piggott power peak at λ = 4.25, it presents a 3.5 % increase compared to the Piggott maximum C_p. Graphic E, of the 7.2 m/s windspeed simulation, shows an overall better performance of the optimized rotor, with an increase of 19 % at a λ = 3.125. The rotors power peak absolute difference is 0.017, meaning a 4.2 % increase of the optimized maximum C_p at λ = 4.375, while the Piggott peak occurs for a λ = 4.25. The last windspeed simulation, 7.7 m/s, that is illustrated in graphic F, presents just as in graphic C and E, an overall better performance of the optimized rotor. At a λ = 3, the optimized rotor has a 22.3 % C_p increase. The Piggott rotor presents a C_p = 0.413 at λ = 4.25, while the optimized rotor exhibits a later (λ = 4.375) but higher power peak of 0.429, meaning a 4 % increase.

Chapter 5

Contributions

The influence of the modification of a wind turbine airfoils in its performance was investigated using the QBlade software to perform the dimensionless BEM simulations. The simulations done with the methodology described in Chapter 3 for the averaged blade with the Piggott airfoils, revealed an overprediction of the rotor performance for high λ values when compared to the averaged blade simulations of [15], as well as a slight increase of the maximum C_p. The averaged blade with the Piggott airfoils simulated in this study, was compared between a rotor with airfoils refined with 100 points and 200 points. The effect translates in an improved stall prediction of the rotor with airfoils refined to 200 points for a range of λ between the lowest value and around a λ = 4.5 that corresponds to the C_p peak.

The aim of the airfoils modification was to improve the C_l/C_d behaviour for the same C_l in order to expand the respective blade $C_p - \lambda$ curve. As for blade 1, the most notorious C_l/C_d improvements occurred for the new airfoil of the blade section 3, 4, 5 and 6. For the remaining two sections, 1 (r = 0.600 mm) and 2 (r = 0.500 mm), there was a slight decrease of their maximum C_l/C_d compared to the corresponding Piggott airfoils. Regarding the performance of blade 2 new airfoils, sections 1,2 and 3 have a better C_l/C_d performance for low C_l values and present a slight increase of their maximum C_l/C_d. The Piggott and modified airfoils of section 4 (r = 0.300 mm) and section 5 (r = 0.200 mm) of blade 2 show an irregular performance, a behaviour due to the construction process error and inaccuracy tendency. The new root section (r = 0.150 mm) presented a slightly better C_l/C_d for the highest C_l values, although with less magnitude compared to the same section of blade 1. The modified airfoils performance of blade 3 showed no significant improvements for section 2, 3, 4, and 5.The new section 1 airfoil presented a better C_l/C_d for the highest C_l, meaning in an higher C_l peak for an earlier AoA. The modified airfoil of the root section showed an improved C_l/C_d for all the C_l range.

The new airfoils were used for the simulations of the new ideal rotors made each of three equal blades. The average of the three ideal rotors allowed to approximate the real wind turbine. The new airfoils wind turbine showed a better performance for the highest λ values, and that λ range where the new averaged blade is better than the averaged rotor with the Piggott airfoils expands with the increase of the windspeed. The simulation of 4.4 windspeed revealed better C_p values for the region regarding the blade stall (left of the C_p peak). It was no expected that for the lowest windspeed, 3.0 m/s, the new rotor would present an inferior maximum C_p. Both rotors power peaks increase with the windspeed and the corresponding λ values decrease.

A study of both averaged rotors performance for a ω = 500 RPM was conducted. The results portrayed that both turbines power output is closely the same, with a slighter better power output of the new turbine for low wind conditions. This means that the simple leading edge airfoil smoothing results in a modified turbine that, once the wind would blow with less intensity, it would need less energy than the Piggott turbine to achieve again higher ω values corresponding to optimum state of functioning.

The modified airfoils comparison of all blades reinforced the fact that blade 2 airfoils do not present the same behaviour as the ones from blade 1 and 3, specially for section 4 (r = 0.300 mm), section 5 (r = 0.200 mm) and section 6 (r = 0.150 mm). With the selection of the modified airfoils from blade 1 and 3, a rotor made from exactly three identical blades was simulated and its results compared to the BEM simulations results of the average rotor with the Piggott airfoils. The results are of significant expression as the optimized turbine presents a noteworthy positive C_p offset between the maximum C_p and up to the highest λ value, as well as higher maximum C_p for all the windspeed simulations.

Bibliography

[1] IPCC, 2013: Summary for Policymakers. In: Climate Change 2013: The Physical Science Basis. Contribution of Working Group I to the Fifth Assessment Report of the Intergovernmental Panel on Climate Change [Stocker,T.F., D. Qin, G.-K. Plattner, M. Tignor, S.K. Allen, J. Boschung, A. Nauels, Y. Xia, V. Bex and P.M. Midgley (eds.)].Cambridge University Press, Cambridge, United Kingdom and New York, NY, USA.

[2] Ciais, P., C. Sabine, G. Bala, L. Bopp, V. Brovkin, J. Canadell, A. Chhabra, R. DeFries, J. Galloway, M. Heimann, C. Jones, C. Le Quéré, R.B. Myneni, S. Piao and P. Thornton, 2013: Carbon and Other Biogeochemical Cycles. In: Climate Change 2013: The Physical Science Basis. Contribution of Working Group I to the Fifth Assessment Report of the Intergovernmental Panel on Climate Change [Stocker, T.F., D. Qin, G.-K. Plattner, M. Tignor, S.K. Allen, J. Boschung, A. Nauels, Y. Xia, V. Bex and P.M. Midgley (eds.)]. Cambridge University Press, Cambridge, United Kingdom and New York, NY, USA.

[3] UNDP. 2009. Office *Resource Guide on Gender and Climate Change*. UNDP. https://www.undp.org/content/undp/en/home/librarypage/womens-empowerment/resource-guide-on-gender-and-climate-change.html.

[4] IPCC, 2014: Summary for Policymakers. In: Climate Change 2014: Mitigation of Climate Change. Contribution of Working Group III to the Fifth Assessment Report of the Intergovernmental Panel on Climate Change [Edenhofer, O., R. Pichs-Madruga, Y. Sokona, E. Farahani, S. Kadner, K. Seyboth, A. Adler, I. Baum, S. Brunner, P. Eickemeier, B. Kriemann, J. Savolainen, S. Schlömer, C. von Stechow, T. Zwickel and J.C. Minx (eds.)]. Cambridge University Press, Cambridge, United Kingdom and New York, NY, USA.

[5] Olhoff, Anne, and John (Hrsg.) Christensen. 2018. *Emissions Gap Report 2018*. https://www.unenvironment.org/resources/emissions-gap-report-2018

[6] IRENA. 2019. "Renewable Capacity Highlights." (March): 1–2. https://www.irena.org/-/media/Files/IRENA/Agency/Publication/2019/Mar/RE_capacity_highlights_2019.pdf?la=en&hash=BA9D38354390B001DC0CC9BE03EEE559C280013F.

[7] IRENA Statistics. 2019. *Renewable Energy Capacity Statistics 2019*. https://www.irena.org/publications/2019/Mar/Renewable-Capacity-Statistics-2019

[8] European Comission. EU energy in figues Union. Statistical Pocketbook 2018. https://publications.europa.eu/en/publication-detail/-/publication/99fc30eb-c06d-11e8-9893-01aa75ed71a1

[9] Wind in power 2017: Annual combined onshore and offshore wind energy statistics, February 2018, WindEurope https://windeurope.org/about-wind/statistics/european/wind-in-power-2017/

[10] Wind energy in Europe in 2018: Trends and statistics, February 2019, WindEurope https://windeurope.org/about-wind/statistics/european/wind-energy-in-europe-in-2018/

[11] APREN. (2018). 2017: Electricidade Renovável Em Revista. *APREN*. https://www.apren.pt/contents/files/2017-eletricidade-renovavel-em-revista.pdf.

[12] IRENA. (2018). Renewable Energy and Jobs - Annual Review 2018, International Renewable Energy Agency, Abu Dhabi. (December): 1–28. https://www.irena.org/publications/2018/May/Renewable-Energy-and-Jobs-Annual-Review-2018.

[13] MHI Vestas Wind Energy. (2018). Available: http://www.mhivestasoffshore.com/innovations/

[14] GE Renewable Energy. (2019). Available: https://www.ge.com/renewableenergy/wind-energy

[15] Monteiro, J. P., Silvestre, M. R., Piggott, H., & Andre, J. C. (2013). Wind tunnel testing of a horizontal axis wind turbine rotor and comparison with simulations from two Blade Element Momentum codes. *Journal of wind engineering and industrial aerodynamics*, *123*, 99-106.

[16] Shepherd, Dennis G. 1994. “Historical Development of the Windmill.” In *Wind Turbine Technology: Fundamental Concepts of Wind Turbine Engineering*, ed. David A. Spera. New York: The American Society of Mechanical Engineers, 1–46.

[17] Manwell, J. F., J. G. McGowan, and A. L. Rogers. (2009). Introduction: Modern Wind Energy and Its Origins. In *Wind Energy Explained: Theory, Design and Application*, ed. John Wiley & Sons Ltd., 1–22.

[18] Dodge, D. M. (2009). Illustrated History of Wind Power Development. [Online]. Available: http://www.telosnet.com/wind. [Consultation date: 05/01/2019]

[19] Fleming, P. D., & Probert, S. D. (1984). The evolution of wind-turbines: an historical review. *Applied energy*, *18*(3), pp. 163-177.

[20] Frost, W, Aspliden, C. (1994). Characteristics of the Wind In *Wind Turbine Technology: Fundamental Concepts of Wind Turbine Engineering*, D. Spera, Ed., pp. 371-445.

[21] Ackermann, T., & Söder, L. (2000). Wind energy technology and current status: a review. *Renewable and sustainable energy reviews*, *4*(4), pp. 315-374.

[22] Jain, P. (2011). Properties of Wind In *Wind Energy Engineering*, ed. McGraw-Hill Companies., pp. 25–40.

[23] Manwell, J. F., J. G. McGowan & A. L. Rogers. (2009). Wind Characteristics and Resources. In *Wind Energy Explained: Theory, Design and Application*, ed. John Wiley & Sons Ltd., pp. 23–89.

[24] Manwell, J. F., J. G. McGowan & A. L. Rogers. (2009). Wind Turbine Siting, System Design, and Integration In Wind Energy Explained: Theory, Design and Application, ed. John Wiley & Sons Ltd., pp. 407–448.

[25] Brederode, V. D. (2014). Conceitos e equações fundamentais da mecânica dos fluidos in *Aerodinâmica Incompressível: Fundamentos*, IST Press, pp. 94-148.

[26] Lynette, R., Gipe, P. (1994). Commercial Wind Turbine Systems and Applications In *Wind Turbine Technology: Fundamental Concepts of Wind Turbine Engineering*, ed. David A. Spera. Washington: The American Society of Mechanical Engineers, pp. 139–214.

[27] Divone, L. V., (1994). Evolution of Modern Wind Turbines In *Wind Turbine Technology: Fundamental Concepts of Wind Turbine Engineering*, ed. David A. Spera. Washington, DC, pp. 73–138.

[28] Wilson, R. E., Lissaman, P. B., & Walker, S. N. (1976). *Aerodynamic performance of wind turbines*, Corvallis, Oregon: Oregon State University, pp. 1-164.

[29] Wilson, R. E. (1994). Aerodynamic Behaviour of Wind Turbines In *Wind Turbine Technology: Fundamental Concepts of Wind Turbine Engineering*, ed. David A. Spera. Oregon: The American Society of Mechanical Engineers, pp. 215–282.

[30] Manwell, J. F., J. G. McGowan & A. L. Rogers. (2009). Aerodynamics of Wind Turbines In *Wind Energy Explained: Theory, Design and Application*, ed. John Wiley & Sons Ltd. , pp. 91–155.

[31] Marten, D., Wendler, J. (2013). *QBlade Guidelines - v0.6*. Available: http://q-blade.org/project_images/files/guidelines_v06.pdf, Consultation date: 03/02/2019.

[32] Hansen, M. O. L. (2008). *Aerodynamic of Wind Turbines*, 2nd ed, Earthscan.

[33] Hosman, N. (2012). Performance analysis and improvement of a small locally produced wind turbine for developing countries. *Master of Science, TU Delft*.

[34] Krogstad, P. Å., & Lund, J. A. (2012). An experimental and numerical study of the performance of a model turbine. *Wind Energy*, *15*(3), pp. 443-457.

[35] Piggott, H. (2003). How to build a WIND TURBINE: Axial flux alternator windmill plans 8 foot and 4 foot diameter machines. Available: http://www.scoraigwind.com/download/index.htm. Consultation date: 10/04/2019.

[36] Marten, D., Wendler, J., Pechlivanoglou, G., Nayeri, C. N., & Paschereit, C. O. (2013). QBLADE: an open source tool for design and simulation of horizontal and vertical axis wind turbines. *Int. J. Emerging Technol. Adv. Eng*, *3*(3), pp. 264-269.

[37] Deperrois, A. (2009). XFLR5: Analysis of Foils and Wings Operating at Low Reynolds Numbers Guidelines for XFLR5.

[38] Silvestre, M. A., Morgado, J. P., & Pascoa, J. (2013). JBLADE: a propeller design and analysis code. In *2013 International Powered Lift Conference* (p. 4220).

Appendix A

Chapter 1 Annexes

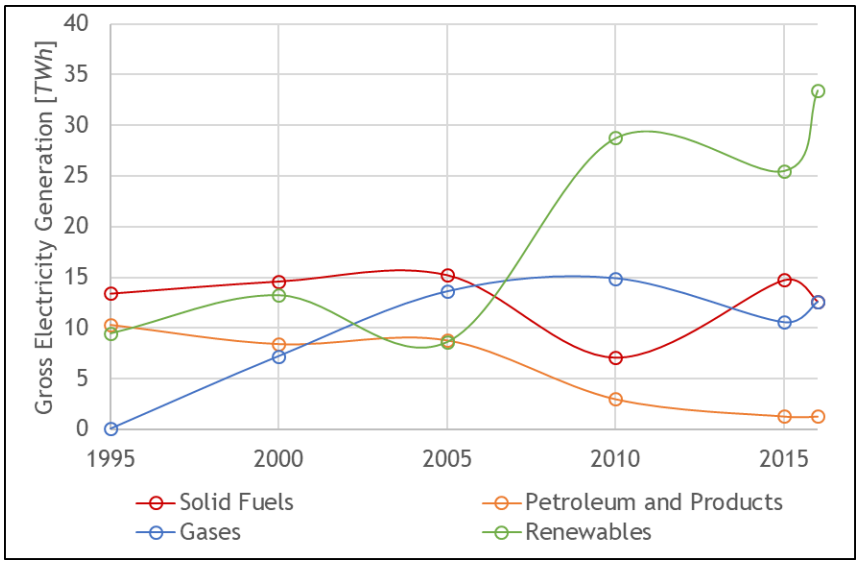

Figure A.1: Portugal gross electricity generation by fuel (adapted from [8)].

a - Bioenergy includes liquid biofuels, solid biomass and biogas.

b - Other technologies include geothermal energy, small hydropower, concentrated solar power (CSP), heat pumps, municipal and industrial waste, and ocean energy.

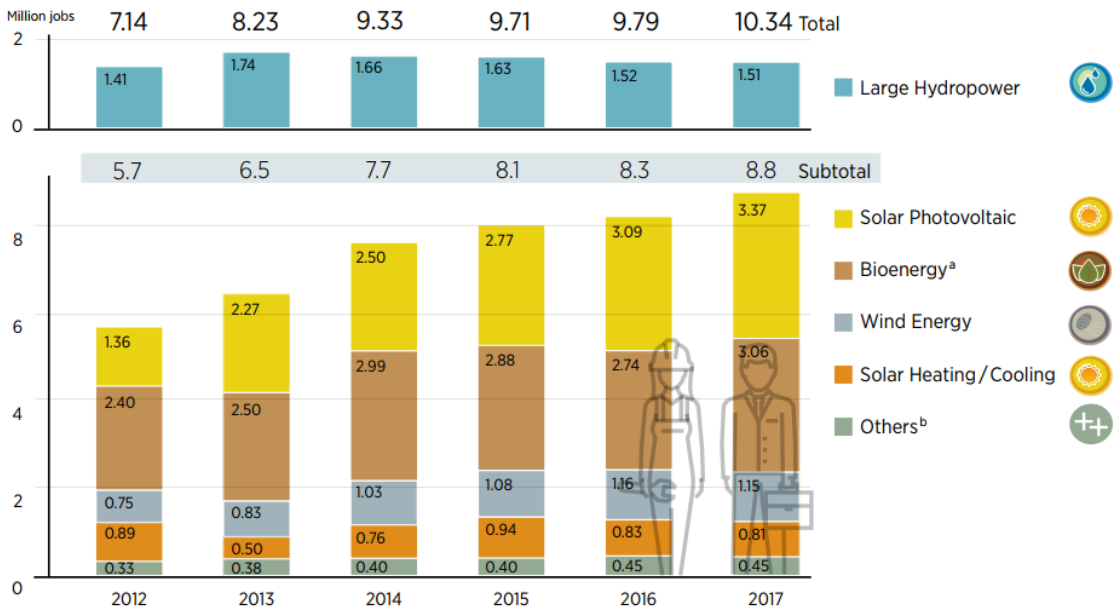

Figure A.2: Global employment by RE technology (adapted from [12]).

Appendix A

Chapter 2 Annexes

A.1: Format of the airfoil file.

Foil Name

X (1) Y (1)

X (2) Y (2)

. .

. .

X (N) Y (N)

Appendix B

Chapter 4 annexes

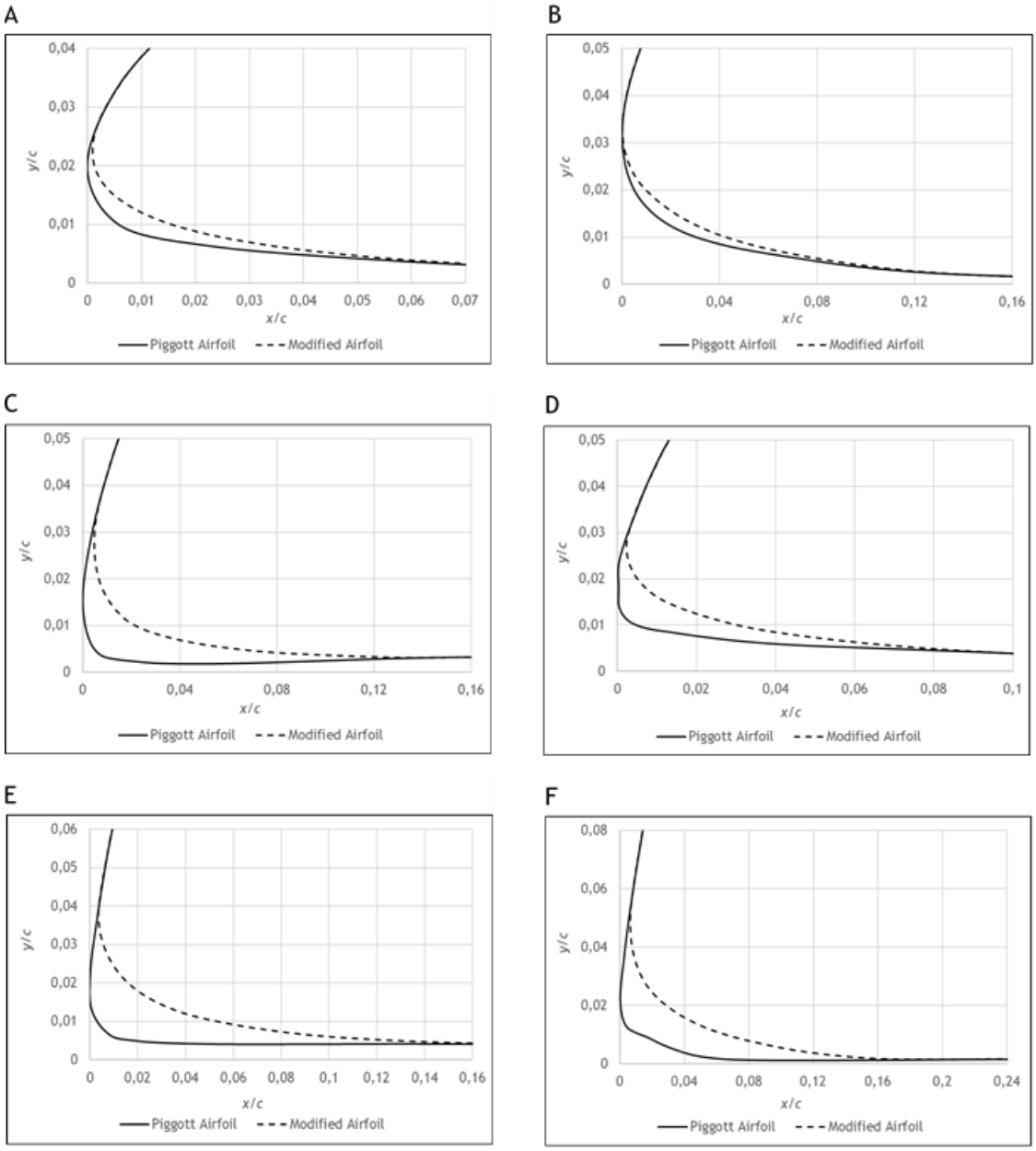

Figure B.1: Blade 1 leading edge zoom of the Piggott and the modified airfoil (A: Section 1; B: Section 2; C: Section 3; D: Section 4; E: Section 5; F: Section 6).

Appendix B

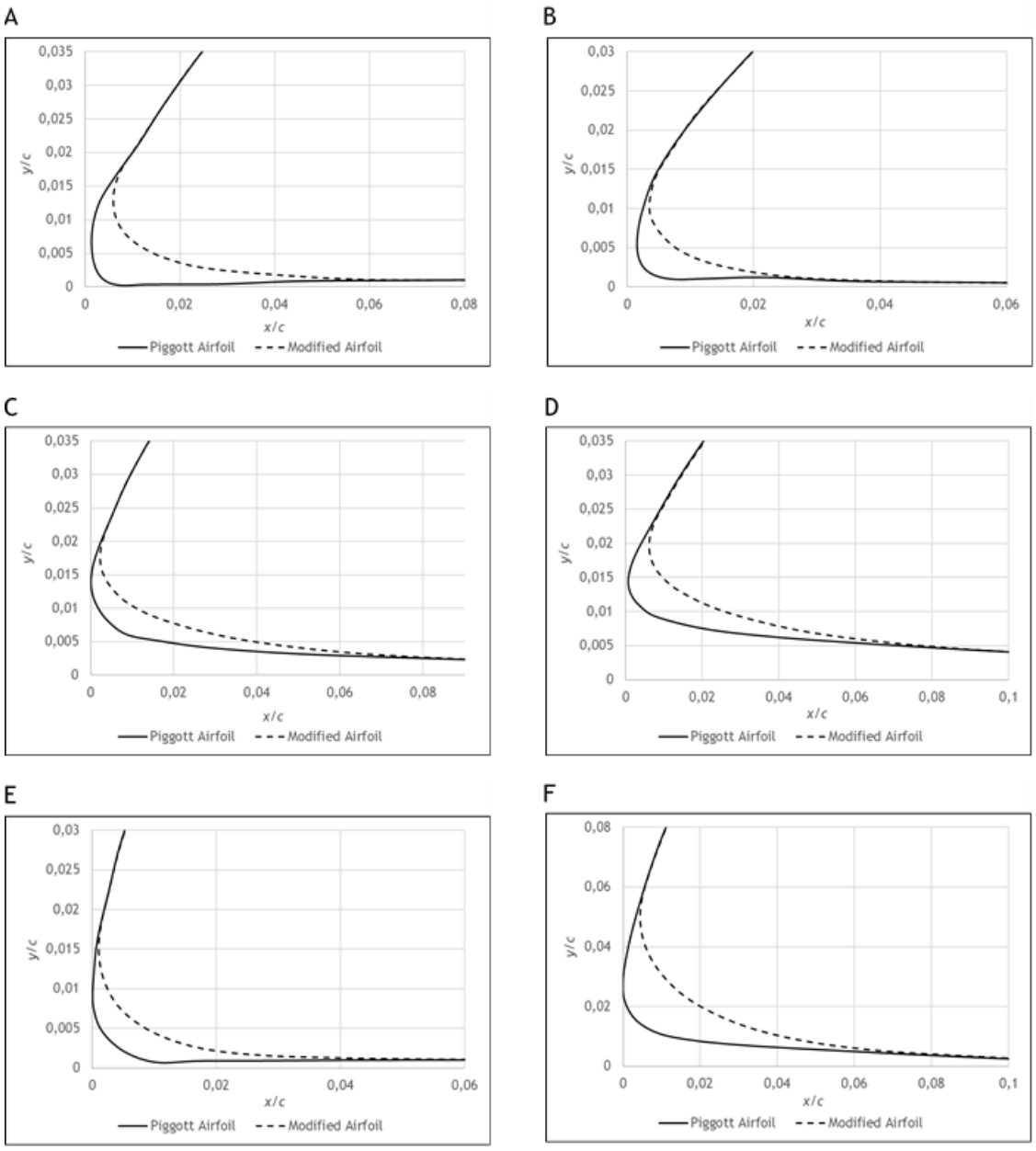

Figure B.2: Blade 2 leading edge zoom of the Piggott and the modified airfoil (A: Section 1; B: Section 2; C: Section 3; D: Section 4; E: Section 5; F: Section 6).

Appendix B

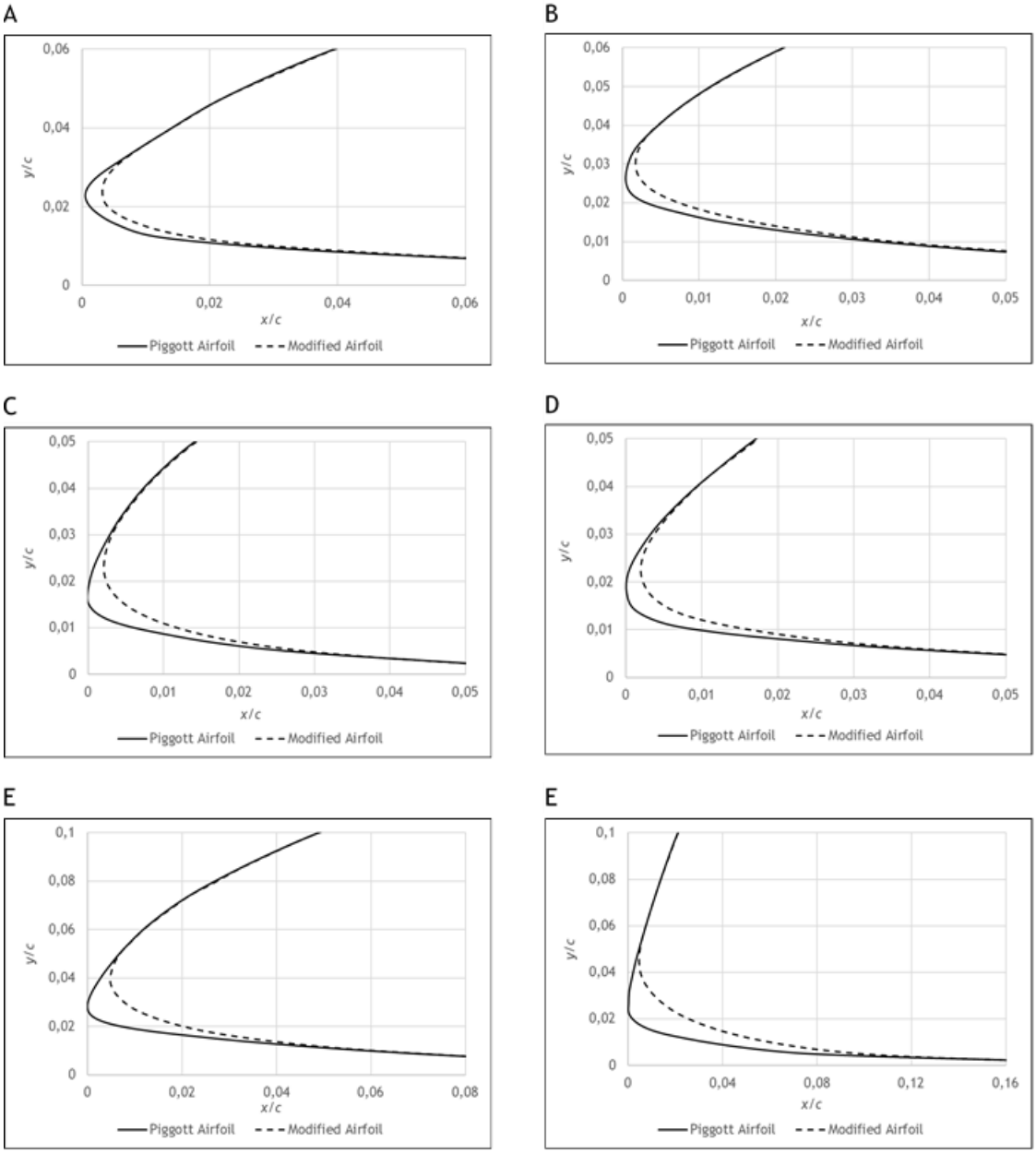

Figure B.3: Blade 3 leading edge zoom of the Piggott and the modified airfoil (A: Section 1; B: Section 2; C: Section 3; D: Section 4; E: Section 5; F: Section 6).

Table B.1: Averaged Piggott and modified rotor power for the 3.7 m/s windspeed.

			Piggott Rotor		Modified Rotor		
ω		λ	C_p	P	C_p	P	Δ P [%]
[rpm]	[rad/s]			[W]		[W]	
150	15.708	2.547	0.118	4.059	0.121	4.133	1.837
200	20.944	3.396	0.196	6.704	0.188	6.430	-4.095
250	26.180	4.245	0.319	10.920	0.280	9.607	-12.024
300	31.416	5.094	0.340	11.631	0.340	11.655	0.205
350	36.652	5.944	0.302	10.333	0.302	10.355	0.220
400	41.888	6.793	0.242	8.294	0.244	8.361	0.811
450	47.124	7.642	0.153	5.242	0.157	5.379	2.614
500	52.360	8.491	0.022	0.769	0.042	1.442	87.391

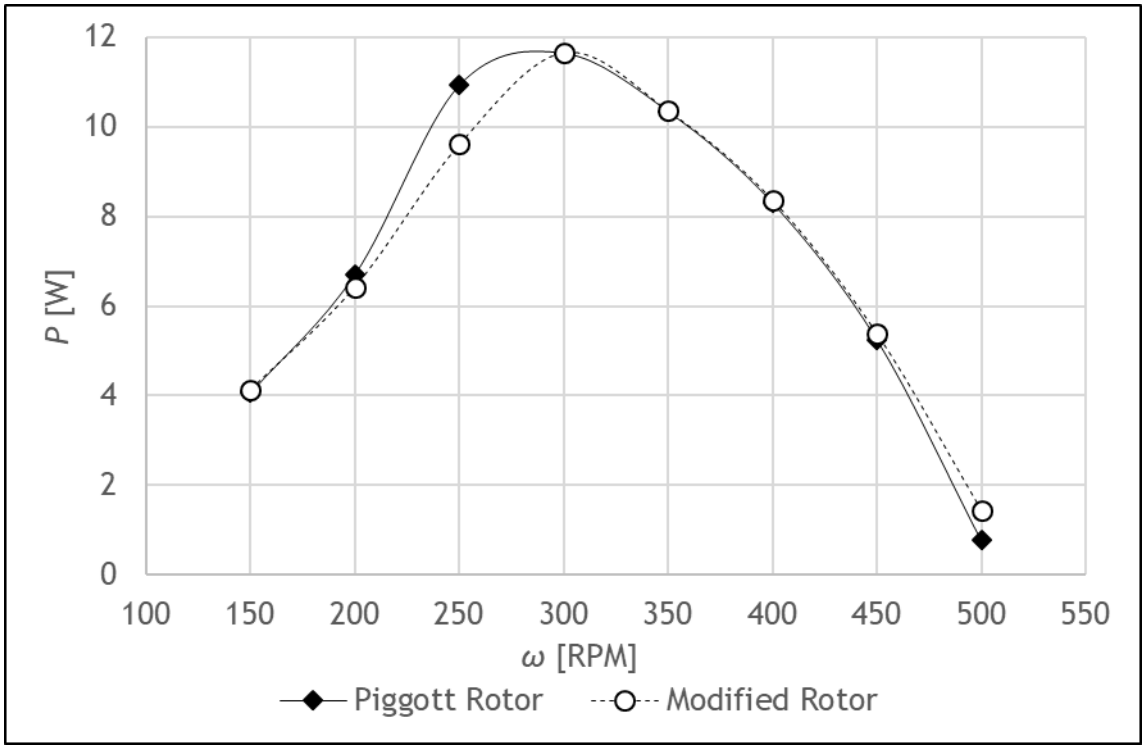

Figure B.4: Averaged Piggott and modified rotor power for the 3.7 m/s windspeed.

Table B.2: Averaged Piggott and modified rotor power for the 4.4 m/s windspeed.

			Piggott Rotor		Modified Rotor		
ω		λ	C_p	P	C_p	P	Δ P [%]
[rpm]	[rad/s]			[W]		[W]	
150	15.708	2.142	0.094	5.396	0.097	5.592	3.627
200	20.944	2.856	0.162	9.343	0.159	9.189	-1.646
250	26.180	3.570	0.236	13.616	0.261	15.058	10.591
300	31.416	4.284	0.362	20.858	0.371	21.350	2.361
350	36.652	4.998	0.366	21.070	0.367	21.160	0.424
400	41.888	5.712	0.335	19.285	0.334	19.245	-0.207
450	47.124	6.426	0.293	16.892	0.294	16.965	0.429
500	52.360	7.140	0.236	13.609	0.239	13.769	1.180
550	57.596	7.854	0.154	8.855	0.164	9.458	6.814
600	62.832	8.568	0.046	2.626	0.071	4.074	55.172

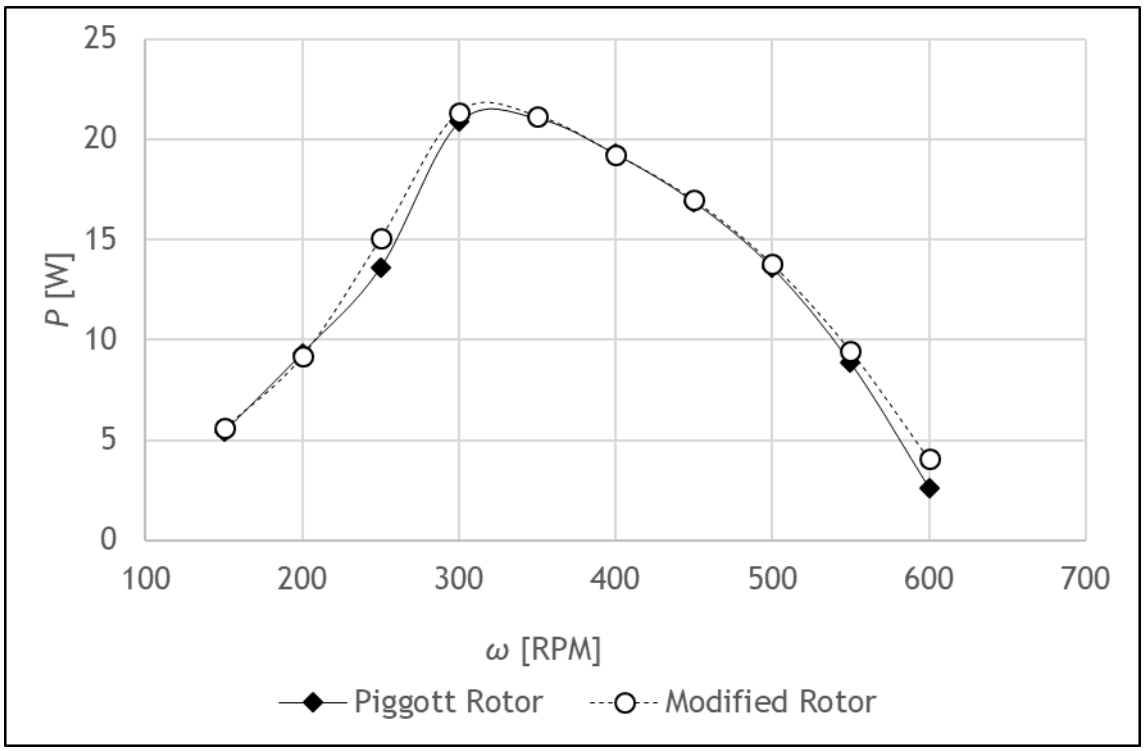

Figure B.5: Averaged Piggott and modified rotor power for the 4.4 m/s windspeed.

Table B.3 Averaged Piggott and modified rotor power for the 5.5 m/s windspeed.

			Piggott Rotor		Modified Rotor		
ω		λ	C_p	P	C_p	P	Δ P [%]
[rpm]	[rad/s]			[W]		[W]	
200	20.944	2.285	0.121	13.610	0.125	14.117	3.725
250	26.180	2.856	0.203	22.844	0.187	21.058	-7.816
300	31.416	3.427	0.300	33.772	0.266	29.981	-11.227
350	36.652	3.998	0.395	44.406	0.396	44.532	0.284
400	41.888	4.570	0.391	44.025	0.391	43.974	-0.114
450	47.124	5.141	0.374	42.057	0.376	42.324	0.635
500	52.360	5.712	0.353	39.744	0.356	40.030	0.718
550	57.596	6.283	0.324	36.468	0.327	36.760	0.800
600	62.832	6.854	0.285	32.111	0.289	32.564	1.414
650	68.068	7.426	0.233	26.248	0.241	27.108	3.277
700	73.304	7.997	0.167	18.745	0.181	20.368	8.661
750	78.540	8.568	0.086	9.718	0.110	12.366	27.256
800	83.776	9.139	-0.009	-0.972	0.026	2.971	-405.795

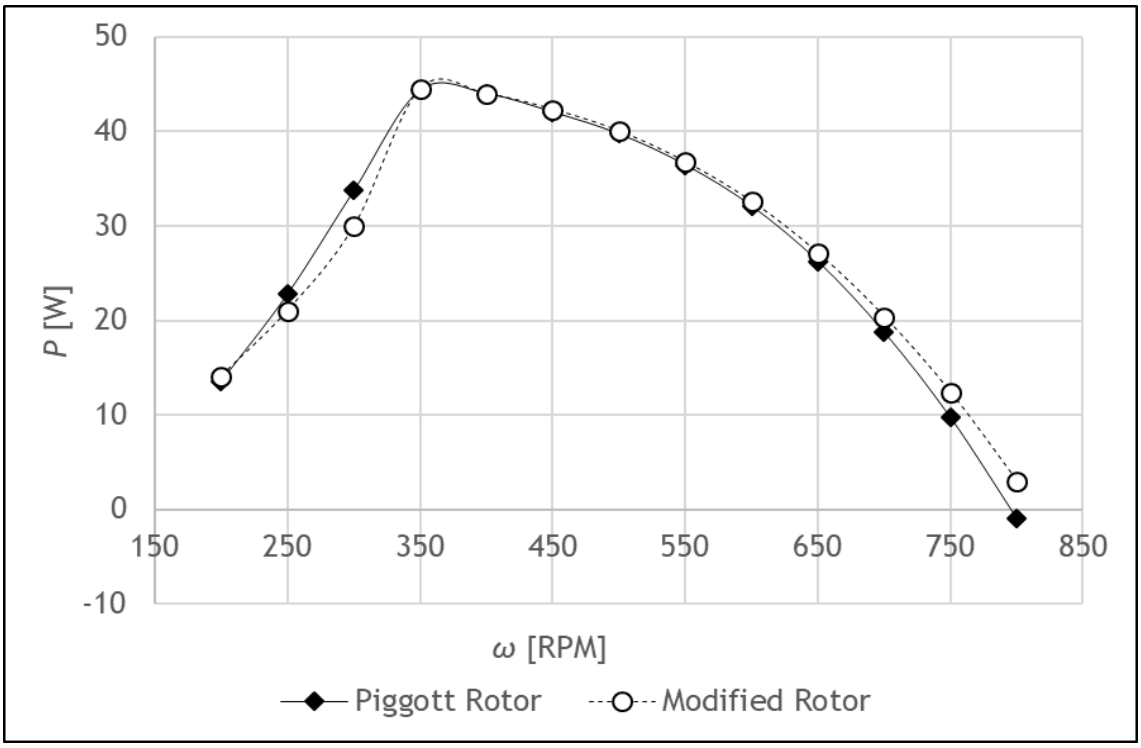

Figure B.6: Averaged Piggott and modified rotor power for the 5.5 m/s windspeed.

Table B.4: Averaged Piggott and modified rotor power for the 7.2 m/s windspeed.

ω		λ	Piggott Rotor		Modified Rotor		Δ P [%]
[rpm]	[rad/s]		C_p	P [W]	C_p	P [W]	
250	26.180	2.182	0.119	29.983	0.111	27.943	-6.804
300	31.416	2.618	0.167	42.063	0.145	36.690	-12.773
350	36.652	3.054	0.270	68.135	0.237	59.737	-12.325
400	41.888	3.491	0.371	93.712	0.362	91.493	-2.368
450	47.124	3.927	0.402	101.523	0.405	102.282	0.748
500	52.360	4.363	0.407	102.847	0.412	104.041	1.160
550	57.596	4.800	0.401	101.338	0.403	101.786	0.442
600	62.832	5.236	0.389	98.201	0.391	98.619	0.425
650	68.068	5.672	0.373	94.078	0.374	94.464	0.410
700	73.304	6.109	0.353	88.998	0.354	89.487	0.549
750	78.540	6.545	0.327	82.458	0.330	83.415	1.160
800	83.776	6.981	0.295	74.456	0.303	76.366	2.566
850	89.012	7.418	0.257	64.902	0.270	68.033	4.824
900	94.248	7.854	0.213	53.722	0.231	58.221	8.374
950	99.484	8.290	0.160	40.331	0.186	47.046	16.650
1000	104.720	8.727	0.099	25.031	0.136	34.430	37.551
1050	109.956	9.163	0.030	7.588	0.078	19.739	160.150
1100	115.192	9.599	-0.049	-12.244	0.014	3.572	-129.170

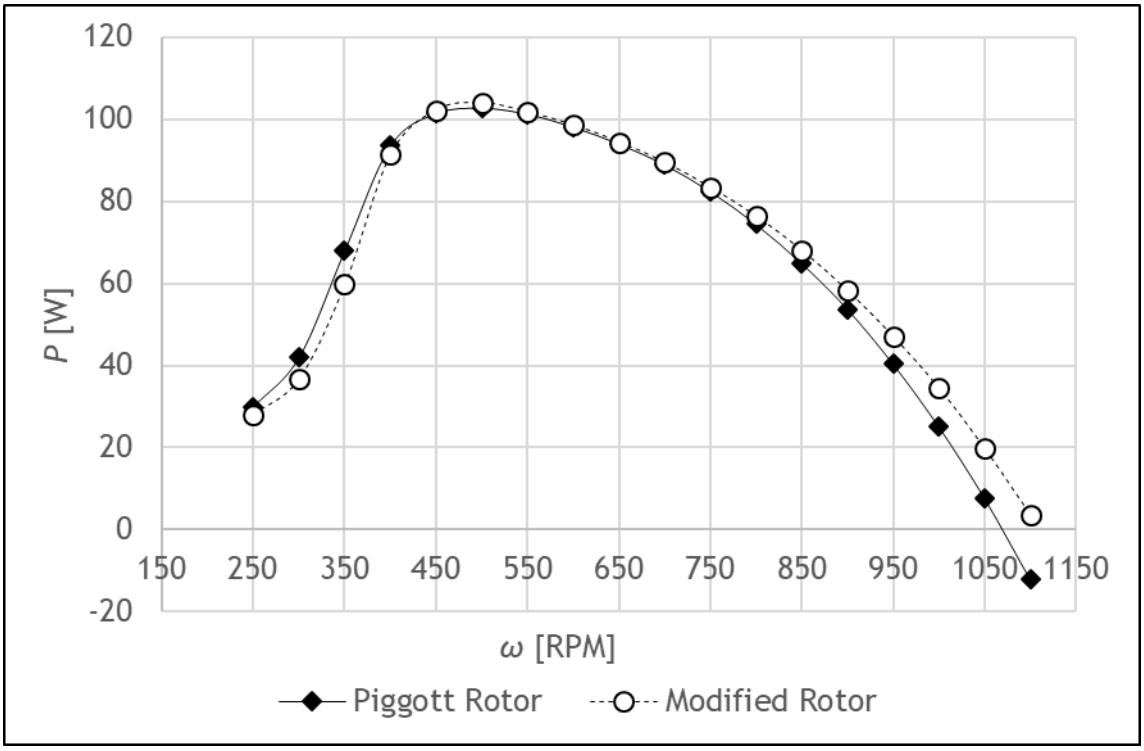

Figure B.7: Averaged Piggott and modified rotor power for the 7.2 m/s windspeed.

Table B.5: Averaged Piggott and modified rotor power for the 7.7 m/s windspeed.

ω		λ	Piggott Rotor		Modified Rotor		Δ P [%]
[rpm]	[rad/s]		C_p	P [W]	C_p	P [W]	
250	26.180	2.040	0.099	30.511	0.103	31.750	4.061
300	31.416	2.448	0.147	45.295	0.143	44.304	-2.188
350	36.652	2.856	0.221	68.311	0.218	67.205	-1.619
400	41.888	3.264	0.338	104.334	0.340	104.988	0.626
450	47.124	3.672	0.393	121.201	0.391	120.848	-0.291
500	52.360	4.080	0.410	126.625	0.412	127.205	0.459
550	57.596	4.488	0.410	126.650	0.411	126.808	0.125
600	62.832	4.896	0.402	124.133	0.403	124.401	0.215
650	68.068	5.304	0.390	120.277	0.391	120.851	0.477
700	73.304	5.712	0.375	115.699	0.376	116.181	0.417
750	78.540	6.120	0.357	110.074	0.359	110.892	0.743
800	83.776	6.528	0.332	102.544	0.336	103.773	1.199
850	89.012	6.936	0.304	94.016	0.310	95.849	1.950
900	94.248	7.344	0.271	83.576	0.281	86.711	3.750
950	99.484	7.752	0.231	71.181	0.247	76.169	7.008
1000	104.720	8.160	0.184	56.673	0.208	64.279	13.420
1050	109.956	8.568	0.130	40.098	0.164	50.657	26.333
1100	115.192	8.976	0.070	21.556	0.114	35.290	63.716
1150	120.428	9.384	0.002	0.513	0.059	18.149	3437.776

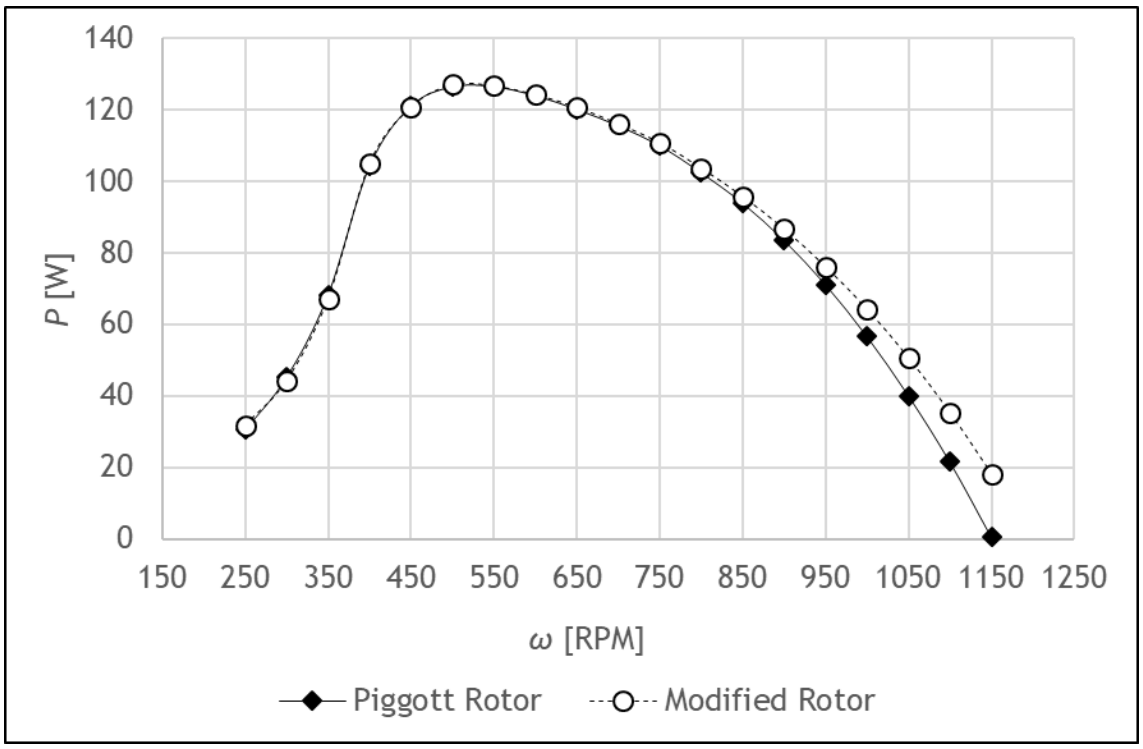

Figure B.8: Averaged Piggott and modified rotor power for the 7.7 m/s windspeed.

Appendix B